Title
Screen Printed MRI Receive Coils

Author
Corea, Joseph Russell

Publication Date
2016

Peer reviewed|Thesis/dissertation

Screen Printed MRI Receive Coils

by

Joseph Russell Corea

A dissertation submitted in partial satisfaction of the
requirements for the degree of
Doctor of Philosophy

in

Engineering – Electrical Engineering and Computer Sciences

in the

Graduate Division

of the

University of California, Berkeley

Committee in charge:

Professor Ana Claudia Arias, Chair
Professor Michael Lustig
Professor Ali Niknejad
Professor Jack Gallant

Fall 2016

Screen Printed MRI Receive Coils

Abstract

Screen Printed MRI Receive Coils

by

Joseph Russell Corea

Doctor of Philosophy in Engineering - Electrical Engineering and Computer Sciences

University of California, Berkeley

Professors Ana Claudia Arias and Michael Lustig

The widespread use of MRI has created a demand for high quality images for current and emerging applications. High quality images are currently acquired by using application specific receive coils that fit close to the patient's body to produce high signal to noise ratio. These coils are manufactured using traditional printed circuit board fabrication technologies that produce large heavy coils that do not suit some applications very well. In particular, two areas that have not been able to take advantage of the current receive coils are pediatric imaging and MR guided high intensity focused ultrasound therapy due to size, weight, and thickness constraints. These two areas would benefit greatly from the high quality imaging provided by purpose-built lightweight and thin receive coil arrays. One way to achieve a very lightweight and thin coil is to fabricate it from solution using printed electronics. Here for the first time, advances in solution-processed fabrication techniques have allowed lightweight, thin, and flexible receive coil arrays to be made for these applications.

In this thesis the development of printed MRI receive coils is discussed, covering fabrication, characterization, and implementation. An entirely printed approach is used to create single element receive coils that are characterized and tested on 1.5 T and 3 T clinical systems. The materials used to fabricate the coil components are identified as a main avenue for improvement. A fully printed proof-of-concept array is made to demonstrate feasibility and is used to image a volunteer on a 3 T clinical system. Coils are optimized with components made from high quality flexible substrates to make better performing printed coils and arrays. These printed arrays are compared to commercially available arrays on several phantoms as well as on a volunteer on a 3 T scanner.

In addition to creating coils for standard clinical imaging, several coils and arrays are optimized for use in an high intensity focused ultrasound interventional MRI. Coil materials are evaluated for acoustic transparency, stability in water, safety, and electrical quality. The optimized coils are used to evaluate image quality as well as to characterize the system level of acoustic transparency. An 8-channel coil array is used to characterize image quality on a volunteer. To show a system level proof-of-concept on an interventional MR system, optimized arrays are used to track ultrasonic heating inside phantoms and ex-vivo tissue.

Overall, the characteristics of the printed coils described in this thesis enable a new generation of coils design for both traditional and emerging applications.

Contents

Acknowledgements

First of all, I would like to recognize that this thesis would not be possible if it were not for the friendship and collaboration between my advisors Prof. Ana Arias and Prof. Michael Lustig. Together, they continue to provide me with an excellent source of advice, ideas, and mentorship. Thanks to them both for providing me with the resources, connections, patience, and environment to be successful.

I would like to acknowledge the funding sources that I have had during my time at UC Berkeley. The work in this thesis was made possible by funding from the National Institutes of Health under R21 EB015628 and R01 EB019241 grants, the Hellman Family Fund, Sloan Research Fellowship, Okawa Research Grant, the Bakar Fellowship and GE Healthcare. I have also been supported by stipends from the Hellman Graduate Research Fellowship and the Andrew Yang Entrepreneurship fellowship. Additionally, I was also fortunate enough to receive funding from the International Society of Magnetic Resonance in Medicine and Focused Ultrasound Foundation to attend several conferences that helped in advancing my work.

I am also thankful for the generous amount of scan time given by UC Berkeley, Stanford, and UCSF. I have the great gratitude toward Ben Ingles, Prof. Dan Vigneron, Prof. John Pauly, Prof. Kim Butts-Pauly for arranging this time. I would also like to thank the Berkeley Brain Imaging Center and Stanford Lucas Imaging center for making sure the scanners always worked and were available.

I wanted to express thanks for the support I received from people at UC Berkeley. I wanted to thank the members of the Arias research group for helping to put together a great lab and work environment. I wanted to specifically recognize the contributions from Balthazar Lechene, who has helped mature my research and career goals. Thanks to Aminy Ostfeld, Adrien Pierre, and Claire Lochner for being with me since the beginning of the lab, together they made an excellent place to do research. Thanks to Alla, Abhinav, Han, Igal, Maggie, Mahsa, Yasser, Ting, and Karthik for continuing to make the group and lab a great place to work.

My research would be nowhere near as mature as it is today without the help of the Lustig research group, particularly Dr. Anita Flynn. She made sure the lab space had at least two of everything and that anything we didn't have was in her basement. Thanks to Dr. Martin Uecker, Frank Ong, and John Tamir for expertly answering my questions about MRI.

I want to thank Samuel Smith, Filip Maksimovic and Donjin Seo, for their advice on engineering inside and out of research. I also wanted to thank Ben Lake, Bill King, Joe Gavazza, Lou Ahtty, Bob Armal and Eric Chu of the Cory Hall machine shop for the advice, support, and tool time I have received from them over the years. I also would like to thank professors Profs. Jack Gallant and Ali Niknejad for serving on both my qualification and dissertation committee.

When I first started this project, my knowledge of MRI was extremely limited, however I was fortunate to have guidance from some of the best minds in the MRI field. I want to thank Dr. Greig Scott, Dr. Galen Reed, Dr. Joseph Cheng, and Dr. Peter Shin for helping me get started with MRI. I would also like to thank the support I received from GE Healthcare's coil division in maturing the printed coil technology. Specifically I wanted to recognize the contributions of Thomas Grafendorfer, Dr. James Tropp, Dr.

Fraser Robb, and Dr. Victor Taracila along with GE Healthcare, for guidance with electrical testing of coils.

I owe a huge amount of thanks to my parents and family for the support they have given me during my pursuit of a graduate degree, even if I did run off to the west coast. They never needed to understand what I was doing to be proud of me.

Finally, I wanted to thank my wonderful lab mate and partner Natasha Yamamoto. She has been the best part of graduate school and the source of my happiest memories.

Chapter 1

1. Introduction and Background

1.1 Introduction

Magnetic resonance imaging (MRI) is a widely used non-invasive imaging technique that provides high resolution images of soft tissue without ionizing radiation [1]. The utility of MRI has made it a powerful tool for doctors to see the physiology and the function of biological processes, such as tissue structure, brain activity, blood flow, and cancer metabolism [2-4]. However, the poor signal-to-noise ratio (SNR) in clinical MRI makes it inherently slow. Scans can trade speed for image resolution, but this would limit the diagnostic quality or use long acquisition times that are impractical and prone to motion artifacts. While there have been many recent advances in MRI such as parallel imaging [5, 6] and compressed sensing [7] to reduce the scan time, these gains are ultimately limited by the SNR of the scan. SNR can be increased by the use of contrast agents [8, 9], higher field scanners [10], and better receive coils [11, 12], with coils providing the most significant gains.

There has been remarkable development in the hardware used to perform MRI, the most notable are the surface coil arrays enabled by Roemer, et al [11]. Since Roemer's landmark article, various surface coils have been designed, each with a particular anatomy and patient in mind. However, to have a truly ubiquitous and useful coil, it must fit a wide variety of patients and sizes. To meet this need without creating custom coils for each patient, flexible coils that conform to a wide range of patients are used for scanning.

Currently, commercial flexible coils are made using traditional printed circuit board (PCB) techniques that produce mechanically robust arrays that are relatively heavy and not very flexible. While all areas of MRI would benefit from having a lighter and more flexible device there are several particular applications that can benefit tremendously from improvements in the coil form factor. For example, even with modern design and fabrication techniques, the existing high SNR surface coil arrays are poorly suited for pediatric imaging and MRI guided surgeries.

Multi-channel coil arrays with high SNR are typically designed for adults and can weigh a few kilograms. Pediatric patients, who often can weigh as little as the array itself, poorly tolerate the size and weight of an adult array. For example, when an adult cardiac array is used to image an infant, a noticeable change in breathing can be detected as the array presses on their chest. Technologists and nurses can lift the array off the patient with an inflexible support former (or even rolled up hospital blankets), but this introduces a performance-reducing gap between the patient and coil. To bring the benefits of high SNR coils to pediatric imaging a new lightweight approach to designing and fabricating coils is needed.

Likewise in MR guided high intensity focused ultrasound (MRgHIFU) therapy - a technique that uses sound waves to locally heat tissue deep inside the body - it is challenging to design coils that can provide high SNR without significantly interfering

with the ultrasound waves. To address this, a coil that is nearly transparent to ultrasound is necessary to provide high-resolution images for guiding the therapy.

In both pediatric MRI and MRgHIFU, a novel solution is needed to tailor high SNR surface coils in order to achieve lightweight, thin, and flexible devices. To provide high quality images, while offering unique design benefits, we create, characterize, and implement several lightweight and thin receive arrays fabricated using screen-printing.

1.2 Thesis Outline

This thesis will outline and explore the benefits, limitations, and suitability of using solution-processed materials for MRI receive coils for clinical applications.

In chapter 1, a brief introduction on MRI is covered, followed by an in depth look at the design of receive coils. Current coil design and manufacturing is covered along with a review of other flexible coils in the literature. A discussion on the coil-sample system is also included to highlight the ultimate limitations for coil design. Chapter 2 focuses on the measurement techniques needed to correctly characterize a coil. Bench top measurements, MRI scan results, and their interpretations are also covered. Chapter 3 discusses the fabrication of flexible MRI coils using screen printing, focusing on manufacturing a coil for pediatric patients. Chapter 4 details the techniques used to optimize printed coils, including an in-depth analysis of a printed coil array. Chapter 5 includes a discussion on how a printed MRI coil could be adapted to high intensity focused ultrasound surgery. Acoustic transparency, water stability, image quality, and safety are characterized. Furthermore, a system level demonstration of a printed array tracking ex-vivo tissue heating is shown. Finally, chapter 6 summarizes the findings of this thesis and suggests avenues for future research and development.

1.3 Basics of MRI

1.3.1 Signal Generation and Detection

An MRI scanner is able to produce images of internal anatomy by taking advantage of the spin angular momentum of atomic species with an odd number of protons, neutrons, or both. These atoms with spin angular momentum are commonly referred to as spins. A simplified way to represent a nuclear spin is to view it as a spinning charged sphere with a specific magnetic moment orientation – shown as a sphere with an arrow in Fig. 1.1 A. The direction of the arrow indicates the positive poll of the tiny magnetic moment. Spins are the basis for MR imaging and are manipulated by applying magnetic fields and radiofrequency (RF) pulses to produce images. [2].

Most biological tissues possess large amounts of hydrogen, an element with a single proton, making it well suited as the source of signal in clinical imaging [13]. Other nuclei can be used, for example, carbon-13 [14], fluorine-19 [15], sodium-23 [16], phosphorous-31 [17], and even certain isotopes of argon [18], but these nuclei are less common. Normally the orientations of the hydrogen spins are randomly distributed in the tissue at any given time and do not have any net magnetization. However, if these spins are placed in an external magnetic field, a small portion will align their magnetic field parallel and anti-parrallel to the external field. A net magnetic moment is only possible because the

parallel state requires slightly less energy than the anti-parallel one and gives rise to a net magnetization aligned to the main field – illustrated in Fig. 1.1 B. The ratio of spins parallel to the field to those anti-parallel is small, about 0.999993%, but it is enough to create a net magnetization that can be used for reception [2]. In a scanner, the source of this static magnetic field is usually a large superconducting solenoid that fully encompasses the sample. Permanent magnets [19], or pulsed currents [20, 21] are also used to generate the main field, but are not as common.

In the presence of a large constant field, the net magnetization aligned with the field is static and undetectable. To detect it, a transverse magnetic pulse is applied to excite the spins, flipping them over by some angle away from the axis of the main magnetic field as illustrated in Fig. 1.1 C [2]. As the spins are flipped away from the main magnetic field axis they will start to precess. The frequency of the spins' precession will be at a unique frequency proportional to the external magnetic field (B_0), called the Larmor frequency (f_{Larmor}), and is described by equation 1.1. In equation 1.1, the gyromagnetic ratio (γ) is equal to 42.58 MHz/Telsa for hydrogen protons [2].

$$f_{Larmor} = \frac{\gamma}{2\pi} B_0 \quad (1.1)$$

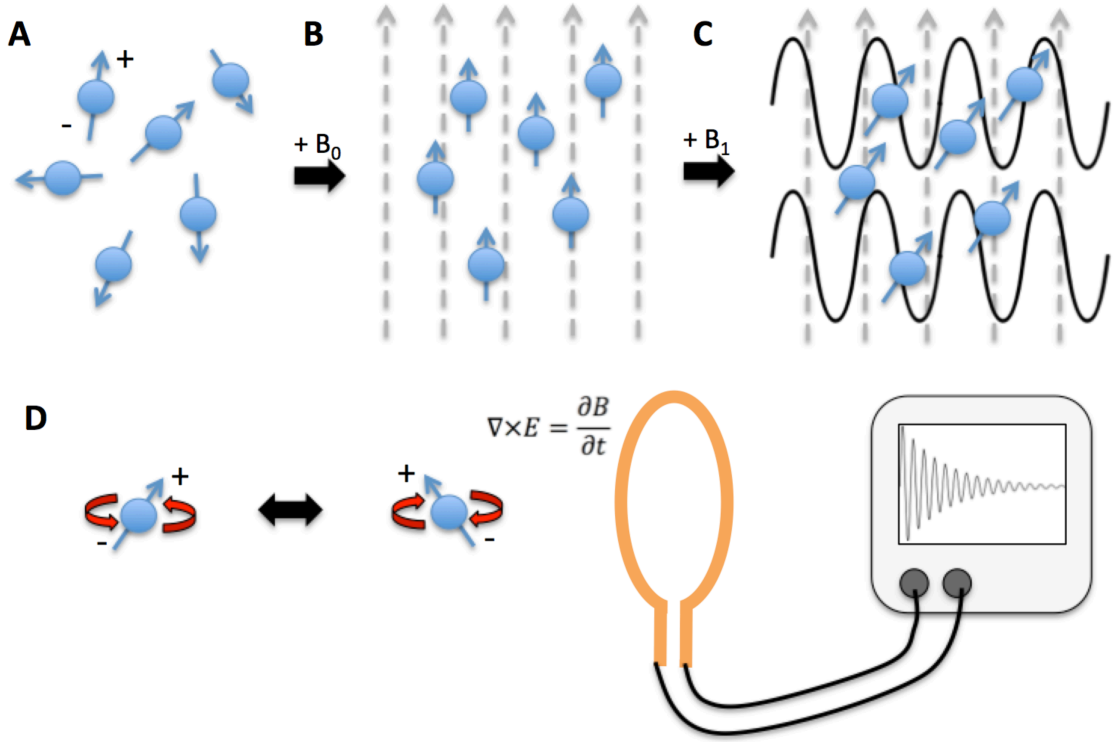

Figure 1.1: **A.** Nuclear spins with magnetic moments randomly oriented with out an external field **B.** Spins aligning with the external magnetic field. **C**. Radio frequency energy is applied to impart some flip angle to spins, creating a transverse magnetic field component. **D.** The precession of spins creates a changing magnetic field that can be detected using a loop of wire through faraday induction.

After excitation, the flipped spins cause the net magnetization to have a transverse component. Figure 1.1 D illustrates how one spin varies with time during its precession and can induce an electromotive force - along with the many other spins - in a nearby loop of wire (i.e., a receive coil) through Faraday's law of induction [3]. This voltage creates a small current that can be detected, amplified, and decoded by the MRI scanner. [2]

1.3.2 Spatial Encoding

Linear magnetic field gradients are the most common method to determine the location of spins inside a scanner. During a scan, linear gradients are applied in the x, y, and z directions across the sample to ensure a unique magnetic field strength at any point in space. This in turn causes all spins at that location to have a unique resonance frequency. For example, the Larmor frequency of a spin at any given point (x) is determined by the main magnetic field and the linearly varying x gradient (G_x) and is described by equation 1.2.

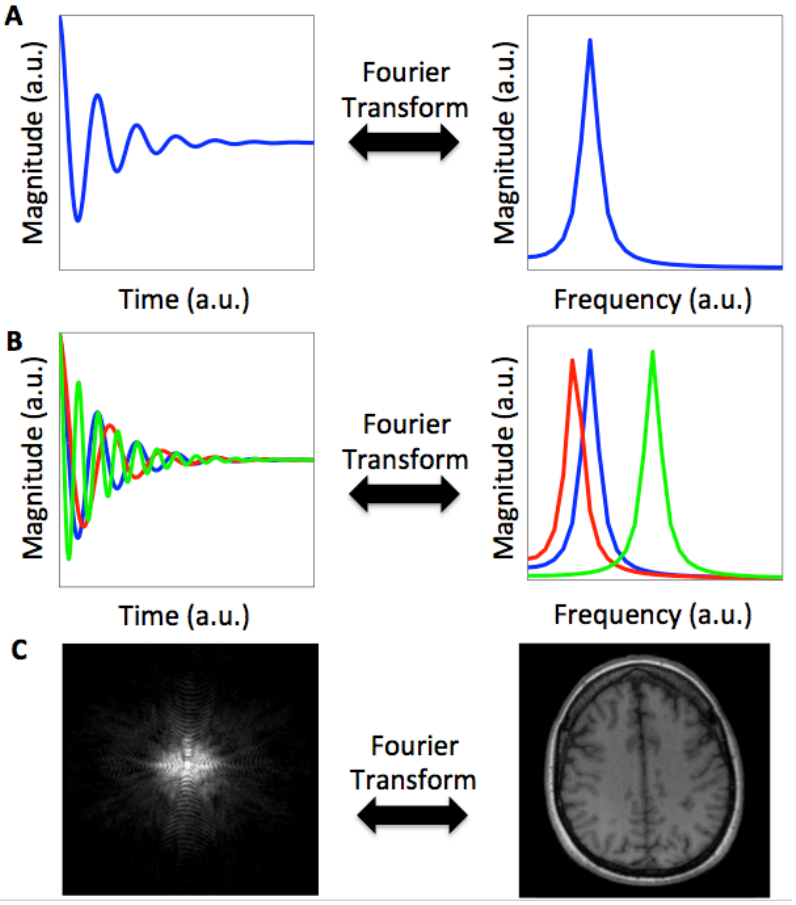

Figure 1.2: **A.** Free-induction decay (FID) from spin at one frequency. Fourier transform reveals frequency. **B.** FID of several spins all at different frequencies received at the same time. Fourier transform reveals separate frequencies. **C.** K-space from scanner and image produced after Fourier transform is taken.

$$f_{Larmor} = \frac{\gamma}{2\pi}(B_0 + G_x x) \qquad (1.2)$$

Figure 1.2 A shows a free induction decay (FID) induced in a receive coil from a single spin with an x gradient applied. A Fourier transform is used to obtain the frequency of the spin that can then be located inside the scanner. Figure 1.2 B illustrates how this technique can be used even if there are multiple FID signals at once because the information is encoded in the frequency and the detected signal is just a linear superposition of all the contributing spins [2]. One way of visualizing this relationship is to think of the frequency response like notes from a piano, with each sound corresponding to a unique location on the keyboard [7].

This technique can be extended to collect multiple lines of data to form an image. A representation of data collected in two dimensions, called k-space, is shown in Fig. 1.2 C. This 2D representation of frequency space can be converted into an image by taking an inverse Fourier transform of the frequency information similar to the 1D case described previously [2, 7] Figure. 1.2 C shows an axial cross section of a volunteer's brain reconstructed using a Fourier transform of the k-space image.

1.3.3 Coils in an MRI scanner

This thesis focuses on the receive coils in an MRI scanner, however receive coils are just one of the many coils in the system that are used to manipulate the behavior of spins. Figure 1.3 A illustrates the approximate locations of all the other coils inside a scanner bore. All of these loops are different types of coils, each interacting with the spins in a unique way.

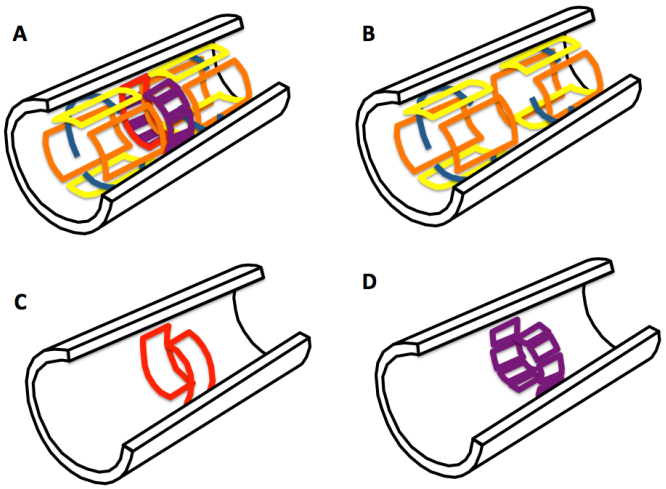

Figure 1.3: **A.** Simplified illustration of different types of coils in an MRI scanner. White coil is the superconducting solenoid that provides a large static magnetic field (B_0). **B.** Gradient coils that provide unique magnetic field strength in X, Y and Z. **C.** Transmit coils that excite nuclear magnetic moments in sample with RF pulses. **D.** Shim coils which help maintain field homogeneity when different samples are placed inside scanner.

The largest loop, a superconducting solenoid (sometimes referred to as a coil) provides the static magnetic field to create a net magnetization in a sample. Gradient coils, illustrated in figure 1.3 B, provide spatial encoding by producing a time-varying linear magnetic field gradient across the bore of a scanner, giving each position in space a unique field strength. A high power transmit coil, which in some designs is also a receive coil, provides a powerful RF pulse to excite the spins in order to obtain a transverse magnetic component – highlighted in figure 1.3 C. Finally, there are low powered shim coils, shown in Fig. 1.3 D, that help maintain a uniform magnetic field despite the distortions created by the sample inside the scanner. [2].

1.4 Receive Coils

1.4.1 Coil Circuit

A receive coil is a resonant circuit tuned to the Larmor frequency of the scanner [3, 22]. The angular frequency (ω) an electrical resonator operates at is determined by the inductance (L) and capacitance (C) of the circuit, as shown in equation 1.13.

$$\omega = \frac{1}{\sqrt{LC}} \quad (1.3)$$

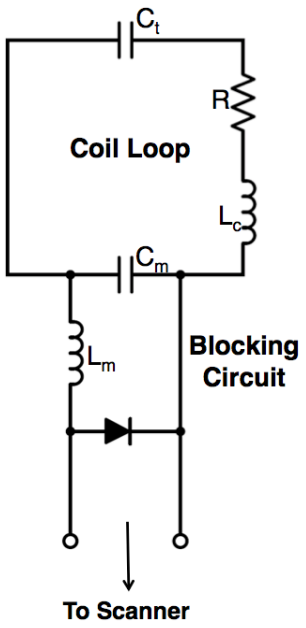

Figure 1.4: Circuit for simple receive coil with a blocking circuit. Coil loop is a resonant circuit comprised of tuning capacitors and loop of wire with some inductance. Blocking circuit consists of a matching capacitor and inductor controlled with a diode.

Typically, the size and shape of the loop are fixed, setting a constant inductance. To tune a coil, in-series capacitors are added to change the resonant frequency of the coil. Figure 1.4 shows a simple receive coil circuit detailing the circuit components used to

tune a coil. The main coil loop is formed form a loop of wire with some inductance (L_c), resistance (R), and tuning capacitor (C_t). The value of the tuning capacitor is the primary means to tune the coil resonant frequency. The input impedance of the coil is tuned using a matching capacitor (C_m) while C_m, the diode, and the matching inductor (L_m) form the blocking circuit. Matching and blocking are described in the following sections.

1.4.2 Coil Matching

All clinical scanners have a 50 Ω impedance receive chain, therefore to reduce the reflection loss of the signal from an impedance mismatch the coil must also be matched to 50 Ω impedance. Specifically, when measuring the input port of the coil, the impedance must be 50 Ω without any inductive or capacitive reactance component. This match is accomplished by introducing an L-network made of inductors, capacitors, or both. In practice this can be implemented by placing a capacitor across the terminals of the probe, shown as C_m in Fig. 1.4. For the common series tuned, parallel matched circuit used in this thesis, the value of capacitances can be determined by equations 1.14-1.15 from Mispelter et al. [22].

$$\frac{1}{C_m\omega} = Z_0\sqrt{\frac{r}{Z_0 - r}} \qquad (1.4)$$

$$\frac{1}{C_t\omega} = L\omega - \sqrt{r(Z_0 - r)} \qquad (1.5)$$

While it is possible to calculate the value of the matching capacitor needed, an iterative tuning approach is usually required because precise characterization of the coil resistance (r) is not straightforward since it relies on the positioning and conductivity of any sample near the coil.

1.4.3 Blocking Circuit

During excitation, the coil circuit must appear like an open circuit in order to not impact the uniformity of the excitation or absorb damaging amounts of RF energy. To accomplish this, a resonant RC tank circuit – otherwise known as a blocking circuit - is put in series with the loop to open the loop during excitation. To switch the blocking circuit on and off, a high quality switching p-type-intrinsic-n-type (PIN) diode is put in series with the blocking circuit. A PIN diode is well suited for this application since it only passes RF energy when it is biased and it can switch quickly [3]. When there is no bias across the diode, no trap circuit exists and the diode is essentially removed from the circuit as illustrated in Fig. 1.5 A. When the diode is biased, a high impedance resonant trap circuit between C_m and L_m is formed, blocking current in the loop, as it is illustrated in Fig. 1.5 B.

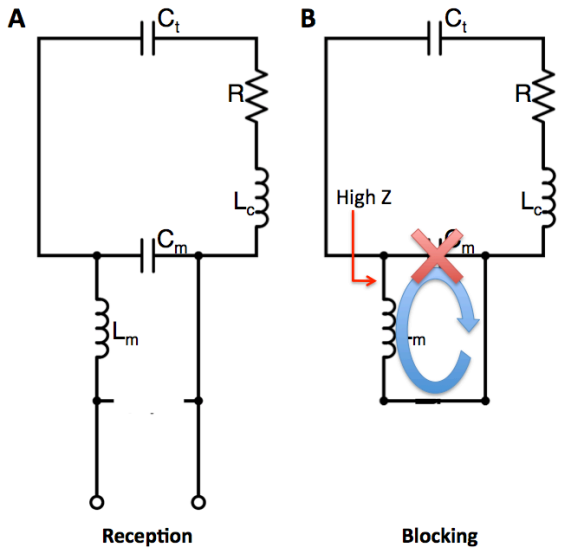

Figure 1.5 **A.** Effective coil circuit during reception. No bias to diode makes it appear removed from the circuit. **B.** When PIN diode is biased it passes RF energy, creating a trap circuit that prevents current from circulating on the main loop.

This blocking circuit switches on and off during every transmit and receive cycle with a period ranging from a few milliseconds to as long as a few seconds. The signal transmitted through the diode is at the Larmor frequency of the scanner.

1.4.4 Coil Decoupling

A surface coil has high SNR because it is not sensitive to noise far away from it. However, if two tuned surface coils are placed near each other, as is the case in arrays of coils, they will inductively couple together effectively increasing the area a coil is sensitive to noise. This will lower the overall SNR and cause high correlation between the two coils, limiting the use of array based acceleration techniques [5]. Furthermore, the presence of another coil will change the tuning of both coils so that they are no longer resonant at the frequency of interest, further lowering the image quality [11].

To prevent coil coupling from occurring, several techniques can be implemented. The first and most straightforward technique is to simply place the coils far away from each other. This technique is effective in reducing coupling, but it is rarely used because it cannot provide sufficient coverage of an entire area of interest. Another method to reduce coupling is to position two coils in planes that are perpendicular to each other. Again, while this method reduces coupling, it rarely provides the coverage needed to be clinically practical [11].

Another way to decouple up to three coils is to overlap them so that the mutual inductance between the each coil is zero, forming a critically overlapped pair. To illustrate this, Fig. 1.6 A shows the scattering parameter response of a single surface coil (a detailed description of scattering parameters is covered in 2.3.1). As this single coil is brought near another tuned coil, as shown in Fig. 1.6 B, the resonant frequency shifts and splits. There is a point where the mutual inductance between the two coils is zero, forming a critically overlapped pair – illustrated in Fig. 6 C.

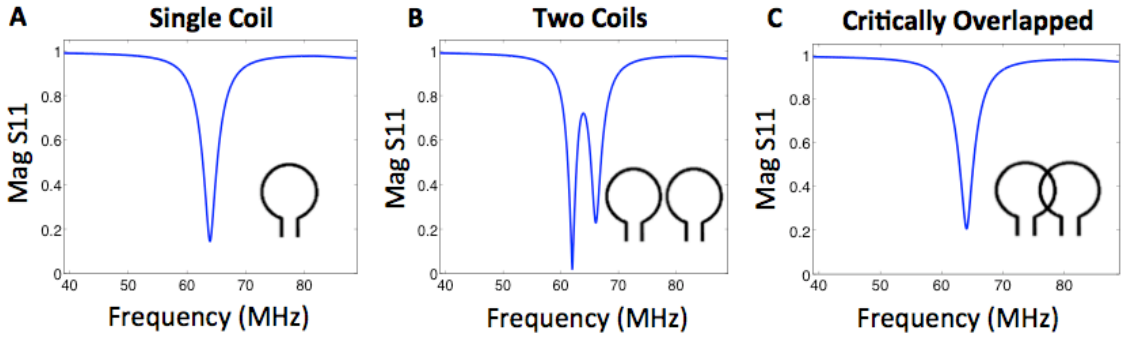

Figure 1.6: S11 response from a surface coil **A** alone, **B** near another surface coil tuned to the same frequency, **C** critically overlapped with another tuned coil.

Even when the coils are critically overlapped, there is some coupling due to the parasitic capacitor formed by the overlapped portions of the coil traces. In order to minimize this interaction, the area of this parasitic overlapping capacitor is reduced. One way to accomplish this is to use octagonal coils instead of circular or square coils because of the reduced overlapped area. Some designs also decrease the width of the conductor in this region to decrease this effect.

Critically overlapping coils is common in surface array coils, however it is only sufficient to decouple the nearest neighboring coils. To decouple the coils from other elements another technique must be used [11].

The most common technique to decouple coils is to use low input impedance preamplifiers in the coil design. This technique uses the low input impedance of the preamplifier to form high impedance trap circuit [11]. Figure 1.7 illustrates how the low input impedance preamplifier acts like a short and forms a high impedance trap circuit with the matching capacitor and inductor in the blocking circuit. This high impedance resonant trap limits the amount of current in the loop and prevents it from significantly coupling to any other nearby coils. However, the current in the blocking circuit is relatively high and causes a significant voltage across the preamplifier allowing it to still receive the MR signal [11].

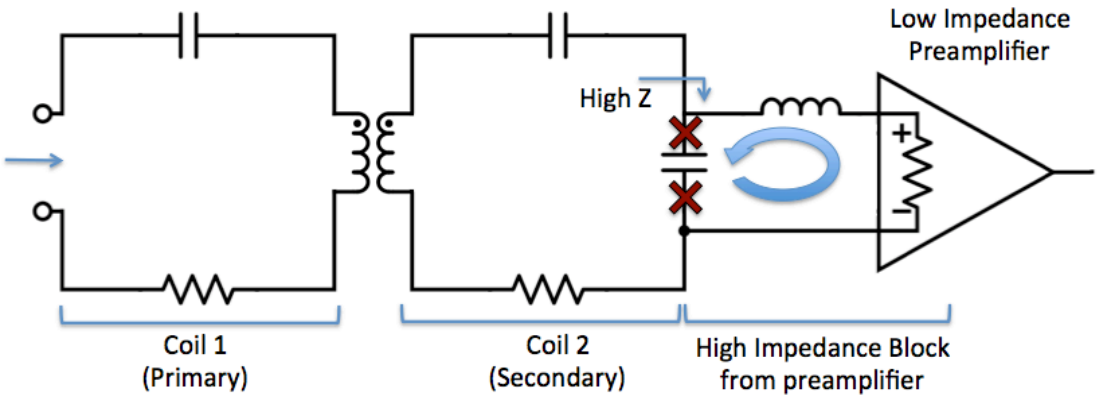

Figure 1.7: Low impedance preamplifier forms blocking circuit at Larmor frequency limiting current in secondary coil reducing inductive coupling between coils.

1.4.5 Coil Cabling and Baluns

Another important component of the receive coil chain are the transmission lines connecting the coil to the scanner. Coaxial cables are typically used to create this link. However, when used inside the scanner, certain lengths of cable can show some sensitivity to the sample and contribute unwanted signal and noise to an image. If these cables are not managed properly the overall SNR of the array can be reduced. In an extreme case, the cables can create dangerous coupling to the transmit coil and create local RF hot spots which can heat up and burn the patient. Figure 1.8 A shows an example of a parasitic current loop that can be formed if baluns are not used. Dangerous hotspots could be formed anywhere along that path.

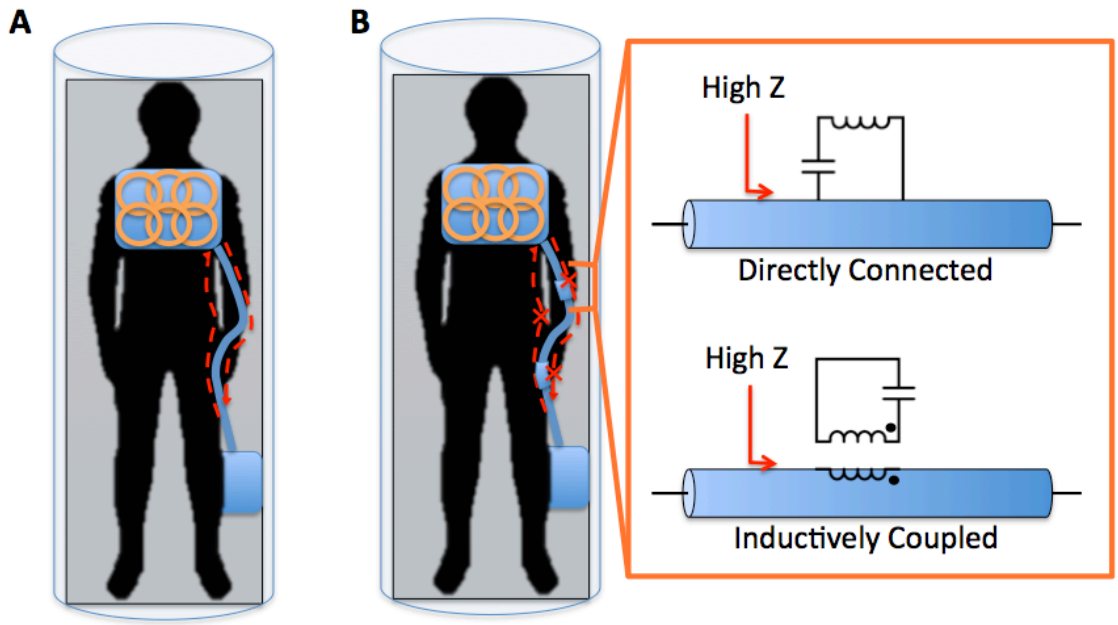

Figure 1.8: **A.** Patient in scanner with coil array placed on chest inside scanner without baluns. Red dotted lines show potential current loop. **B.** Patient in scanner with balun equipped coil array. Baluns break up current loop with high impedance and prevent coupling to the transmit coil. Inset shows (top) directly soldered balun circuit and (bottom) inductively coupled balun circuit used to create high impedance on the outside of the cable.

To prevent currents from existing on the outside of the cables, trap circuits are placed at several intervals along the length of the wire. In other areas, such as antenna design, this would be accomplished by the addition of a ferrite bead on the outside of the cable which offers broadband blocking, however this approach is not compatible in an MRI system due to the high static magnetic field present. Instead of this, a band stop filter – called a balun or cable trap - can be created on the outside of the cable.

The two main ways of constructing a high impedance balun are by soldering a trap to the cable or inductively coupling it to the outside of the cable as shown in the inset of Figure 1.8 B. The most straightforward method to create a balun is to solder a capacitor across a wound section of transmission cable. This uses the inductance of the wound

section of cable in conjunction with the soldered capacitor to form a high impedance trap at the frequency of operation. While directly soldering a capacitor across a wound section of cable is a very robust way to implement a trap, during initial coil design it is more useful in to have the ability to add and remove traps without having to remake the entire cable. A removable, or floating balun, shown in Fig. 1.8 B, creates the high impedance trap circuit by surrounding the cable with a tuned trap. The trap inductively couples to the cable and creates a high impedance block. This block provides lower impedance than a directly connected version due to an imperfect coupling between trap and cable, but it is suitable for initial coil testing. For both types of baluns, the typical blocking attenuations we measured for clinical systems are -12dB or lower.

1.4.6 Body Noise Dominance

The dominant source of loss in a coil/sample system is a key parameter in the design of a coil array. As a coil couples to a sample, the total resistance of the coil is not only dependent on the coil materials, but the sample as well. The loss from the sample can be significant, particularly in clinical scenarios where the coils and sample are relatively large. One particularly important outcome of a sample-dominated system is that no additional improvements to the coil could significantly increase the SNR, setting an upper limit on the coil performance.

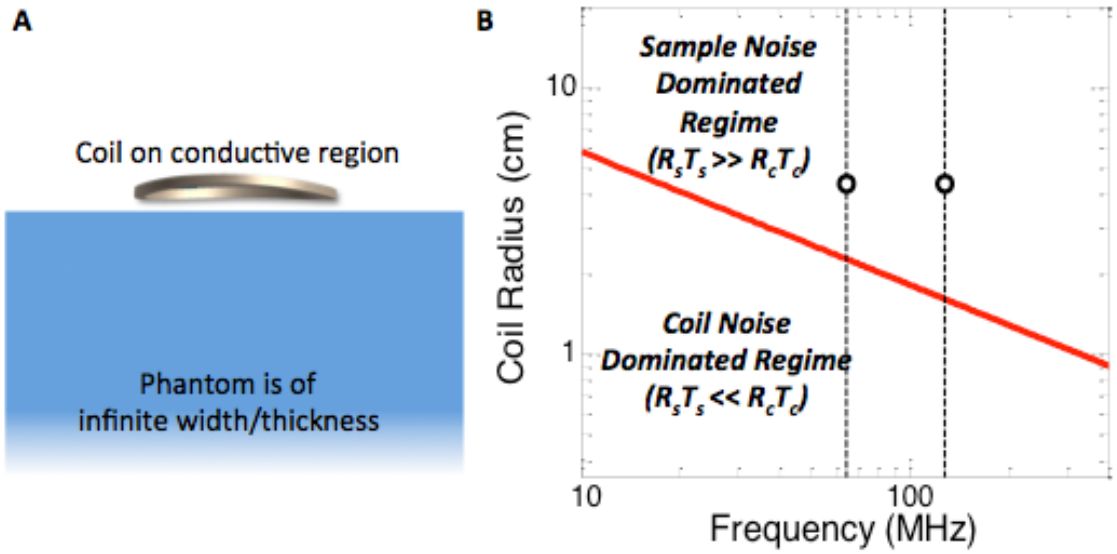

Figure 1.9: **A.** Coil on semi-infinite phantom with conductivity similar to tissue (0.67 S/m). **B.** Frequency dependence of sample noise and coil nose dominated regimes. Black circles highlight coil used in example at 1.5 and 3 T.

To illustrate this point, consider a 3.75 cm radius coil used to image a human abdomen. To estimate the point where the coil and sample noise are equal, the simplified model of a coil and a semi-infinite phantom system can be used as described in Darrasse et al.[23]. Figure 1.9 A illustrates the setup considered with the coil placed on top of a

semi-infinite phantom of a constant conductivity. Using equations 1.6 and 1.7 with the coil placed directly on the surface of a conductive phantom (d = 0), coil conductivity (ρ_c) of 8.02 × 10^5 S/m, coil fill factor ($\xi a/r$) of 45, sample conductivity (σ) of 0.66 S/m, sample temperature (T_s) of 37°C, and coil temperature (T_c) of 20°C the graph shown in Fig. 1.9 B is produced. Figure 1.9 B shows where the sample and coil noise are equal vs. frequency, anything above the red line has loss primarily dominated by sample noise, where as anything under the line is predominantly coil noise limited.

$$R_c = \sqrt{0.5\rho_c\mu_0\omega}\left(\xi\frac{a}{r}\right) \qquad (1.6)$$

$$R_S \approx \frac{2}{3\pi}\sigma\mu_0^2\omega^2a^3\tan^{-1}\left(\frac{\pi a}{8d}\right) \qquad (1.7)$$

In the frequency range of 10 to 400 MHz shown in Figure 1.9 B, we can see a large gap between a coil with a radius of 3.75 cm and the red line where coil and sample noise are equal. This suggests that a coil of this size would be mostly impacted by the noise contribution from the sample, not the coil materials at both 1.5 and 3 T. This would then allow the designer to choose different material systems for coil fabrication. As coil materials contribute more loss, the red line in Fig. 1.9 would move up, decreasing the sample noise dominated regime. This analysis provides a first reference to analyze whether the main source of noise is the coil materials or from the phantom. To quantify the impact of this effect another analysis method, such as calculating coil efficiency, must be used.

1.4.7 Coil Efficiency

The efficiency of a coil can be calculated to quantify how much signal lost due to coil losses. During excitation, a finite amount of magnetization is produced in the sample – giving rise to an intrinsic SNR (SNR_0). As the signal from the spins moves along the receive chain, a portion of it is lost at each step. For a coil designer, the goal is to extract the most signal as possible from a coil, however as previously mentioned, a large portion of the loss can come from the sample, not from the coil materials. Even if a completely lossless coil is used a fundamental limit exists on how much SNR can be extracted out of a given coil/sample system.

To predict how close a real coil is to an ideal lossless coil, the loss of a coil is characterized by measuring its quality factor in and out of the presence of a representative phantom - Q_{Loaded} and $Q_{Unloaded}$ respectively (further described in section 2.3.2). If the $Q_{Unloaded}$ and Q_{Loaded} on a particular phantom are known, the efficiency of a coil can be predicted using equation 1.8 from Link in Rudin et al. [24] where SNR_0 is the total available, (i.e. intrinsic) SNR [25, 26].

$$SNR = SNR_0\sqrt{1-\frac{Q_{Loaded}}{Q_{Unloaded}}} \qquad (1.8)$$

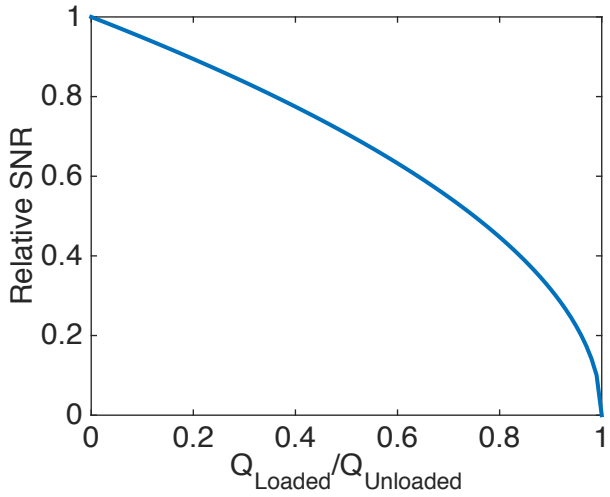

Figure 1.10: Coil efficiency and maximum SNR for a given $Q_{loaded}/Q_{unloaded}$ ratio.

Figure 1.10 shows the trend of the relative SNR vs. the $Q_{Unloaded}$ and Q_{Loaded} ratio. Any $Q_{Unloaded}$ and Q_{Loaded} ratio lower than 0.2 would not experience a large increase in SNR from improving the coil. For example, if a designer measures a coil to have an efficiency of 97%, then even a super-conducting lossless coil would only gain a 3% increase in SNR. This provides a good context to evaluate any design decisions, like the value of adding the complexity of a super-conductive coil system to increase SNR by a marginal percentage.

This characterization technique requires careful measurement of coil quality factor to accurately predict SNR. The details of performing this and other measurements are the focus of chapter 2.

1.4.8 Coil Sensitivity and Positioning

While there are a multitude of designs for a receive coil, the two main types common to clinical imaging are those that image an entire volume and those that are placed on the surface of the sample, commonly referred to as volume or surface coils respectively [3].

Volume coils typically have excellent uniformity with a large field of view (FOV). This large sensitivity to the entire enclosed volume lowers the SNR of the coil because while there is signal from the encompassed sample, the large amount of noise from the entire enclosed area is contributing to the image as well [3]. The wide field of view has made these coils well suited for applications that image large sections of the body at low resolution, such as the initial images taken to localize the patient in the scanner. To illustrate this, Fig. 1.11 A shows an image of a large cylindrical phantom produced by the low SNR volume coil of a 3T scanner. In this image the entire phantom is visible with a uniform sensitivity, but the overall image is grainy. To increase the SNR in a particular area to get high-resolution images without changing scan parameters, surface coils are used.

Surface coils have a narrower field of view, allowing them to reject noise from other areas of the sample while providing stronger signal from the area of interest. This method

gives a much higher SNR than a volume coil. However, as a result, the surface coil does not have a uniform coverage, being most sensitive to tissue close to the coil. Figure 1.11 B shows an image illustrating the limited coverage of a surface coil with the same scan parameters as those in Fig. 1.11 A. While the coverage is limited, the signal near the coil is much higher than the volume coil image in Fig. 1.11. Likewise the image has low noise near the coil and gradually becomes grainy farther away from the coil. To increase the FOV, a larger coil could be used, however this would increase the volume the coil is sensitive to and lower the SNR. A practical way of increasing the FOV without lowering the SNR is to use an array of multiple single coil elements [3, 11]. Figure 1.11 C illustrates how additional elements of a receive coil array can increase the FOV while maintaining a high SNR.

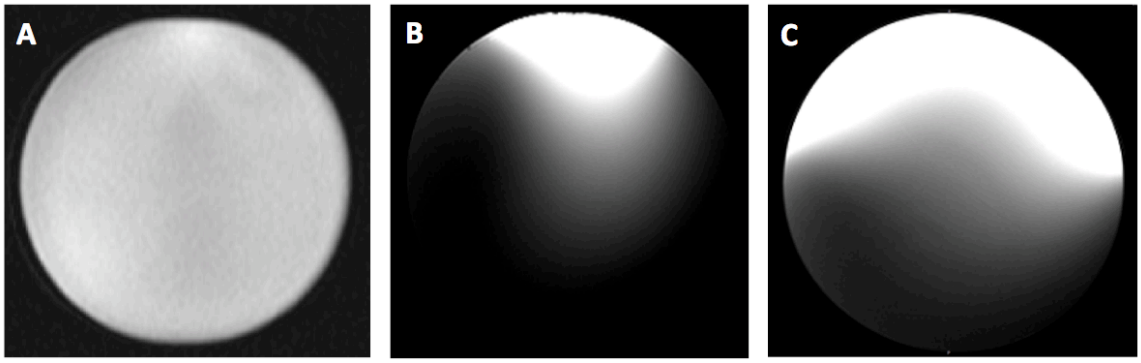

Figure 1.11: **A.** Image of cylindrical phantom with large volume coil showing large field of view but high noise. **B.** Single surface coil image of phantom providing high signal locally on top of phantom, but poor field of view. **C.** Image from array of surface coils providing high signal and an increased field of view. All images were acquired using the same scan parameters and are displayed with similar windowing.

To illustrate the region of space a surface coil is sensitive to, an example focusing on a 10 cm diameter surface coil is described. While there are many ways to calculate the sensitivity pattern of a surface coil, a convenient closed form way to calculate the magnitude of the magnetic field is by using the quasi-static solutions (equations 1.9-1.14) outlined in Landau and Lifshits [27] for a loop of wire in free space. More rigorous solutions exist for conductive media inside a scanner [28, 29], but a quasi-static solution is sufficient to illustrate the general trend of coil sensitivity.

$$k^2 = \frac{4ar}{(a+r)^2+z^2} \tag{1.9}$$

$$K = \int_0^{\pi/2} \frac{d\theta}{\sqrt{1-k^2\sin^2\theta}} \tag{1.10}$$

$$E = \int_0^{\pi/2} \sqrt{1-k^2\sin^2\theta}\, d\theta \tag{1.11}$$

$$B_r = \frac{\mu_0}{4\pi} \frac{2z}{r\sqrt{(a+r)^2+z^2}} \left[-K + \frac{a^2+r^2+z^2}{(a-r)^2+z^2} E\right] \tag{1.12}$$

$$B_z = \frac{\mu_0}{4\pi}\frac{2}{r\sqrt{(a+r)^2+z^2}}\left[K + \frac{a^2-r^2-z^2}{(a-r)^2+z^2}E\right] \quad (1.13)$$

$$B = \sqrt{{B_r}^2 + {B_z}^2} \quad (1.14)$$

$$B_{Transverse} = B \cdot P \qquad where: P = [0, 1, -i] \quad (1.15)$$

In these equations, the radius of the coil (a) and the permittivity of free space (μ_0) are used to calculate the magnitude of the coil sensitivity field (B) in free space (r,z). E and K shown in equations 1.3 and 1.4 are the complete elliptic integrals of the first and second kind with elliptic modulus k. Note that only the right handed transverse component is actually detected by a receive coil so the polarization vector (P) is needed to get the sensitivity pattern seen on a scanner described by equation 1.15. These equations produce the sensitivity pattern shown in 1.12 A with a cutline shown in 1.12 B. In Fig. 1.12 A the regions closest to the coil have the highest sensitivity, with the largest being near the conductive loop. This trend is further highlighted by Fig 1.12 B, which shows the sensitivity of the coil decreasing as the distance from the coil increases, quickly falling near zero for a distance approximately equal to the diameter of the coil.

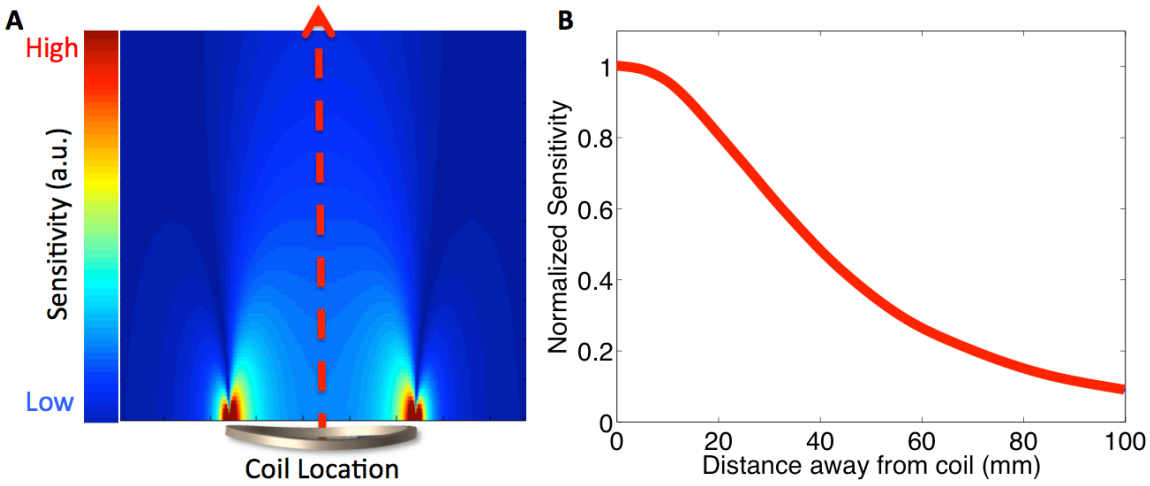

Figure 1.12: **A.** Sensitivity profile for 10 cm diameter receive coil in free-space calculated with equations 1.2-1.7. Red dotted cutline shows location of coil centerline. **B.** Sensitivity along central axis of coil in free-space.

Since there is a spatial dependence of SNR for a surface coil, it is desirable to have the coil elements close to the sample to maintain high SNR. However, it is possible to have the coil elements too close if the sample is conductive [30]. When a conductive sample is too close, the coil can create small parasitic currents in the surface of the phantom. Usually, the sample presents low electrical conductivity, so the loss from these eddy currents is reflected in the overall SNR seen from the coil. The ideal offset distance

(h) can be calculated using equations 1.16-1.19 from Suits et al. which predicts the relative SNR along the z-axis of a coil at depth (d) [30].

$$SNR \propto a^3 |B_1(h+d)| \sqrt{\frac{\omega L}{(r_0 + r_L(h))}} \tag{1.16}$$

$$B_1(z) = \frac{\mu_0}{4\pi} \frac{2\pi a^2 I}{(a^2+z^2)^{3/2}} \tag{1.17}$$

$$r_L(h) = \frac{\pi \mu_0{}^2 \sigma \omega^2 a^3 f\left(2\frac{h}{a}\right)}{4} \tag{1.18}$$

$$f(\beta) \approx \frac{8}{3\pi^2} \tan^{-1}\left(\frac{\pi}{4\beta}\right) \tag{1.19}$$

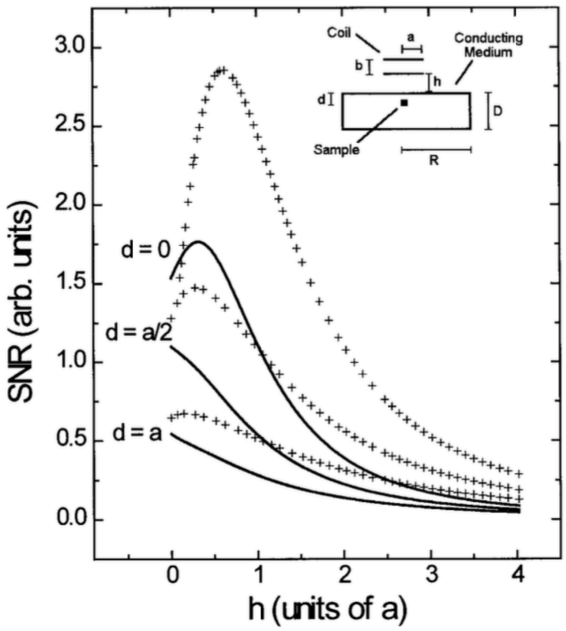

Figure 1.13: Dependence of SNR on coil height for signals from a depth d for an ideal simple surface coil (solid line) and a two coil NMR gradiomter probe (dotted line) system with the coil spacing equal to one-half the coil radius (b = a/ 2) as computed using Eq. 1.8. The inset shows the geometry used here. (Reproduced from Suits et. Al [30] with permission)

In equations 1.16-1.19, (a) is the radius of the coil, (r_0) is the series resistance of a coil in free space, (r_L) is the series resistance of a coil in the presence of a conductive body, (σ) is the conductivity of the sample, (I) is a test current –typically equal to 1, and (μ_0) is the permittivity of free space. Figure 1.13 (reproduced from Suits et. Al [30]), shows that for some points inside a phantom, there is an optimal distance for a surface coil to be offset from the sample. For example, for points near at the surface of the phantom (d ≈ 0)

the peak SNR is obtained when there is a gap of approximately half the radius of the surface coil. For points in the phantom deeper than half the radius of the coil (d = a/2) this loss effect is no longer relevant.

Once the sensitivity pattern has been estimated it can then be used to calculate the SNR of a coil sample system using equation 1.12 [3, 5, 24, 31]. Then, other equations can be used to calculate the loss from the coil (r_{coil}) and the sample (r_{sample}) – discussed further in the section 1.4.7. Other loss mechanisms exist, such as radiated and dielectric losses, but they are typically low in clinical systems and can be omitted.

$$SNR = \frac{B_1}{\sqrt{r_{coil}+r_{sample}}} \qquad (1.20)$$

1.4.9 Traditional Flexible Coils Fabrication

Figure 1.14: Traditional head and current flexible cardiac coils on patient.

The most common method of fabricating flexible receive coils employs flex-PCB circuits encased in a foam barrier [32-34]. Fabrication starts by soldering discrete high quality porcelain capacitors onto copper traces adhered to polytetrafluoroethylene (PTFE) or polyimide (PI) substrates. Next, diodes, inductors, and pre-amplifier boards are soldered onto the copper traces. Typically, solder joints are backed with fiberglass boards to create stress relief to prevent the mechanical forces from breaking the solder. Other stiff plastic or metal pieces may be added to prevent bending in the mechanically fragile areas [33, 35]. Once cables are attached, the entire structure is enclosed in foam to provide a soft cleanable surface that protects the coils against contact from body parts or fluids. Commercial coils are built to standards that must comply with international ratings for flammability, mechanical composition, and electrical safety – set by Underwriters Limited (UL) 94, International Electrotechnical Commission (IEC) 60601-2-33, and Center for Devices and Radiologic Health (CDRC) guidelines. To achieve all these requirements with the current fabrication procedure, designers construct robust coils.

However, this results in a coil array that is heavy, uncomfortable, and not very flexible. Figure 1.14 shows two examples of current state of the art coils on a patient. The patient's head is in a head array while a current flexible cardiac coil is on the patient's chest. Note that the flexible cardiac array on the chest of the patient is only flexible in the direction across the patient's chest and not down their body. The packaging and materials used to construct the coil determine the thickness and flexibility of the cardiac array.

Other methods of assembly have been investigated to achieve a better patient fit. For instance, hinge joints and flexures can be implemented in coil design, similar to the techniques used in making a suit of armor, to join various hard inflexible circuit modules. One such example is the 32-channel coil designed for pediatric applications by Vasanawala et al. [35]. In this work, groups of coils are encased in hard plastic enclosures that move independently from each other to conform to the patient. Another example for a 7 T system used conductive hinges to add adjustability [36]. Flexible coils designs have even incorporated liquid metal into their design, such as the mercury filled tube - shown in figure 1.15 A [37, 38]. This approach was very flexible, but was never widely adopted due to the substantial manufacturing and safety concerns stemming from the high toxicity of mercury.

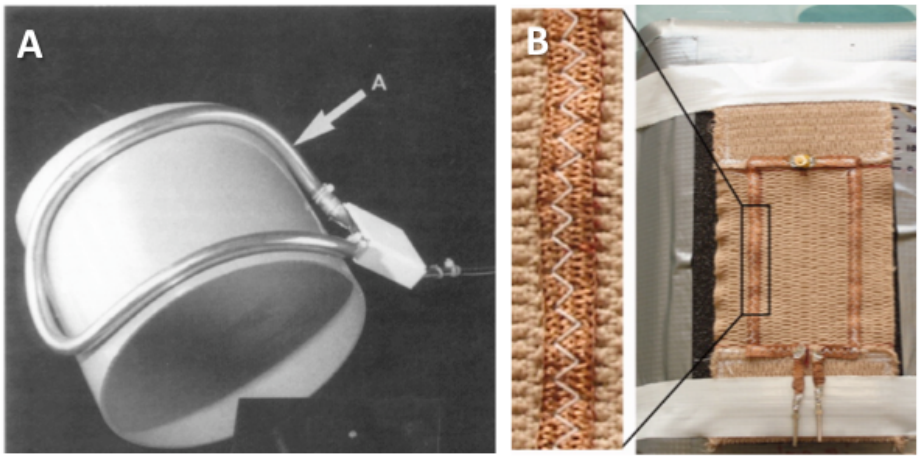

Figure 1.15: **A.** mercury filled tube creating flexible coil (Reproduced with permission from Malko et al.[37]). **B.** Copper wire sewn into stretchable fabric to create flexible and stretchable coil. Inset shows close up of copper sewn into fabric. (Reproduced with permission from Nordmeyer-Massner et al. [39])

Another unique approach to construct a flex coil is to sew conductive metal fibers into a flexible and stretchable fabric, such as the one created by Nordmeyer-Massner et al. [39] for imaging knees on a 3 T system. Figure 1.15 B shows a picture of this coil made of elastic fiber cloth (91% cotton and 9% polyimide) with a zig-zag stich of sewn copper braid to form the coil elements. Using this technique, the authors made an 8-channel stretchable array. Since the sewn coil was stretchable, large changes in input impedance and resonance frequency were reported. The change in input impedance was partially addressed by implementing a split-resonance pi-matching network. However, even with a matching network that could be retuned they still observed a notable decrease in SNR as the coil stretched. When the coil was returned to its original shape, the SNR was maintained. While this technique is novel, it requires an automatic matching

adjustment technique [40], something that is still an area of research [41, 42]. Additionally, connections between the sewn portions of the coil were accomplished by soldering directly to the copper braid, making it prone to breaking. These issues, along with the challenge of mass-producing a precision sewing process to compete with adjustable knee arrays, have limited the implementation of this particular style of coil [39].

1.4.10 Solution Processed Flexible Coils Fabrication

To create a robust mass-produced array that is lightweight and flexible a different fabrication process is needed. One way to accomplish this is to create coils using printed electronics. Printed electronics is a manufacturing process that deposits electrically active material (i.e., conductors, insulators, and semiconductors) onto surfaces from solution. Using this technique, a wide variety of materials and substrates can be used to build electronic devices. This field has already shown promise for the fabrication of light emitting diodes, thin film transistors and photovoltaic devices [43-47]. In addition to a more streamlined fabrication process, the flexibility of printed electronics offers considerable advantages when in contact with the body [48, 49]. For example, a printed sensor can be made with a much larger area and flexibility than a traditionally made sensor, allowing it to cover larger areas on the body giving better results. These flexible large area sensors could then be used to monitor potential sites of pressure wounds or the state of wound healing [50, 51].

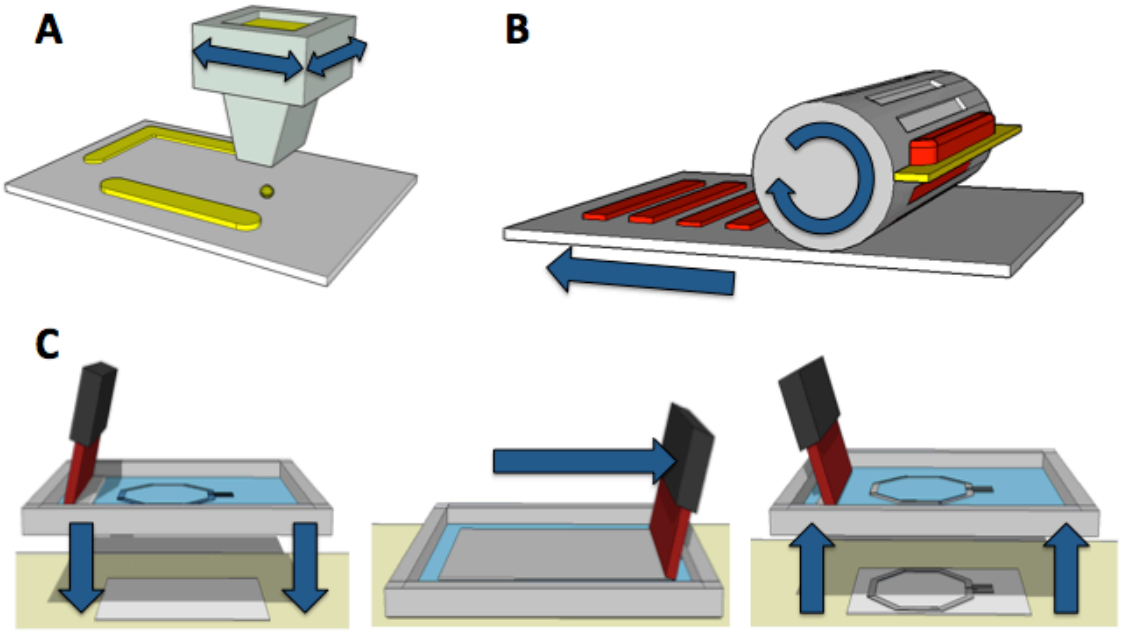

Figure 1.16: **A.** Inkjet printer nozzle depositing ink (yellow) drop-by-drop to create patterns on the substrate below. **B.** Gravure printer (gray cylinder) depositing ink (red) in a pattern as the etched cylinder is rolled along substrate. **C.** Screen printer depositing ink through patterned holes in the screen.

There are various techniques that can be used to deposit materials in patterns. Figure 1.16 shows three common forms of printing, inkjet, gravure, and screen printing. Inkjet printing, shown in Fig. 1.16 A, deposits ink drop-by-drop through precision actuated nozzles onto substrates creating very fine patterns [43]. Figure 1.16 B shows the gravure printing technique, which uses a rotating drum with patterns etched into it to form wells where the ink can be transferred onto a substrate. A flat bar, called a doctor blade, scrapes ink from the raised portions of the cylinder and ensures that the ink only fills the recessed portions of cylinder. The ink is then transferred as the cylinder rolls over the substrate. This technique can produce fine features very quickly, but the thickness of the film is limited [44]. Screen printing, illustrated in Fig. 1.16 C, passes ink through holes in a patterned mesh onto a substrate below [52]. A flexible hard rubber bar forces the ink through the holes in the screen. The blocking emulsion on the screen ensures the ink is only deposited in desired areas. This technique is high throughput and can deposit thicker films than inkjet or gravure printing, but the resolution is not as high. By utilizing these techniques, array designers can deposit materials to create highly flexible, lightweight devices that conform to the human body, much like tailored garments.

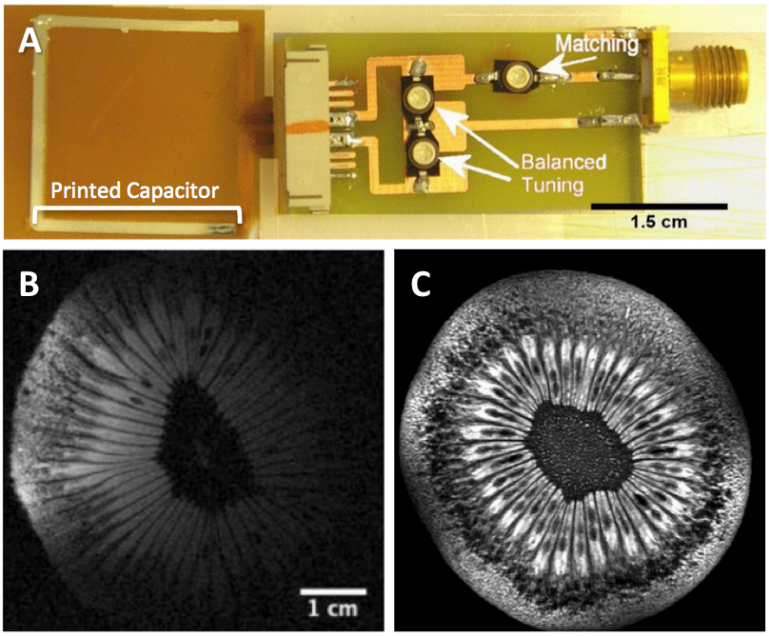

Figure 1.17: **A.** Photograph of a flexible coil fabricated using inkjet printing. **B.** Scan of a kiwi fruit using flex coil from Mager et al at 9.4 T. (reproduced with permission from Mager et al. [53]). **C.** Higher SNR image of kiwi fruit from 4.7 T scanner with a inflexible coil. (Image reproduced with permission from Erikson et al. [54]).

The first work that utilized printing techniques to build a receive coil was performed by Mager et al. in 2010. In that work, a thin flexible coil was developed by inkjet printing silver nanopowder suspension (U5603) from SunChemicals coil on polyimide combined with traditional PCB technology. This coil was designed to be used in a 400 MHz animal scanner and could be wrapped around a sample. As it is shown in figure 1.17 A, two of the three tuning capacitors of this coil were printed, but non-printed trimming and

matching capacitor were used to interface with the scanner. As a proof of concept, a kiwi fruit was imaged, which is shown in figure 1.17 B.

The images produced by the partially printed coil in Mager et al. did not match the performance expected from the scanner used. Specifically, the printed coils only provided half the SNR of a traditionally fabricated coil made for the study [53]. Since Mager did not include an image of the kiwi with a traditional coil for comparison, a higher SNR image of a kiwi fruit by Erikson et al. [54] produced by a different scanner is included in Figure 1.17 C. While these two images in Figs. 1.17 B and 1.17 C were from different scanners, used different sequences, and were averaged differently, the difference in SNR is similar to that reported in Mager et al. Specifically, the reported SNR from the traditional coil in Fig 1.17 C is 122 while the printed coil from Mager in Fig 1.17 B provided an SNR of 80 near the surface. Even though this not a direct comparison, the two kiwi images in Figs. 1.17 B and C make it clear that the SNR lost by using printed materials significantly degrades the fine detail in the image. This loss in quality comes from the relativity poor conductivity of the printed conductor and the low loss contribution of the sample. Currently, solution processed conductors present poorer electrical conductivity than their non-printed counterparts [53]. Furthermore, in a small sample system (i.e., a kiwi in a small animal scanner) there is more sensitivity to the electrical performance of the coil materials (discussed previously in section 1.4.6). Improved printed conductors are constantly being developed, so this technique may still one day be a viable way to make small sample coils, but for now traditional methods are more appropriate.

Another interesting approach to fabricate a coil is to use 3D printing. This printing technique uses a variety of methods to deposit structural material to build up a 3D solid layer-by-layer. The work by Horch et al. in 2015 showed a 3D printed custom coil support with a solution processed conductor [55]. The former had a void in the shape of the coil that was then filled with silver conductive ink and connected to an external matching network to form nuclear magnetic resonance (NMR) coils. This enabled a novel method to perform NMR by measuring liquid samples that flowed through a central hole in the 3D printed coil. While this approach was not flexible, it allowed the authors to rapidly produce custom coils. However, much like the inkjet printing attempts, limitations in coil quality prevented significant advancement of this technique for NMR where the sample is small [55]. While 3D printing is not a good match for small sample imaging it shows much promise for constructing coils for clinical systems and still represents an exciting avenue for future coils research.

The methods used previously for fabricated flexible printed coils have shown promise, but all still need to overcome their shortcomings before being widely adapted. In the remaining chapters a screen printed coil approach will be used to show the strengths of printing in a clinical environment.

1.5 References

[1] P. C. Lauterbur, "Image Formation by Induced Local Interactions - Examples Employing Nuclear Magnetic-Resonance," *Nature,* vol. 242, pp. 190-191, 1973.

[2] D. Nishimura, *Principles of Magnetic Resonance Imaging*: Stanford University, 2010.
[3] J. T. Vaughan and J. R. Griffiths, *RF coils for MRI*. Chichester, West Sussex: John Wiley and Sons Ltd., 2012.
[4] J.-M. Jin, *Electromagnetic analysis and design in magnetic resonance imaging*. Boca Raton: CRC Press, 1998.
[5] K. P. Pruessmann, M. Weiger, M. B. Scheidegger, and P. Boesiger, "SENSE: sensitivity encoding for fast MRI," *Magn Reson Med,* vol. 42, pp. 952-62, 1999.
[6] M. A. Griswold, P. M. Jakob, R. M. Heidemann, M. Nittka, V. Jellus, J. Wang*, et al.*, "Generalized autocalibrating partially parallel acquisitions (GRAPPA)," *Magn Reson Med,* vol. 47, pp. 1202-10, 2002.
[7] M. Lustig, D. L. Donoho, J. M. Santos, and J. M. Pauly, "Compressed sensing MRI," *Ieee Signal Processing Magazine,* vol. 25, pp. 72-82, 2008.
[8] P. Caravan, J. J. Ellison, T. J. McMurry, and R. B. Lauffer, "Gadolinium(III) chelates as MRI contrast agents: Structure, dynamics, and applications," *Chemical Reviews,* vol. 99, pp. 2293-2352, Sep 1999.
[9] H. B. Na, I. C. Song, and T. Hyeon, "Inorganic Nanoparticles for MRI Contrast Agents," *Advanced Materials,* vol. 21, pp. 2133-2148, Jun 5 2009.
[10] O. Ocali and E. Atalar, "Ultimate intrinsic signal-to-noise ratio in MRI," *Magn Reson Med,* vol. 39, pp. 462-73, Mar 1998.
[11] P. B. Roemer, W. A. Edelstein, C. E. Hayes, S. P. Souza, and O. M. Mueller, "The NMR phased array," *Magn Reson Med,* vol. 16, pp. 192-225, 1990.
[12] F. Wiesinger, P. Boesiger, and K. P. Pruessmann, "Electrodynamics and ultimate SNR in parallel MR imaging," *Magn Reson Med,* vol. 52, pp. 376-90, Aug 2004.
[13] D. I. Hoult and P. C. Lauterbur, "Sensitivity of the Zeugmatographic Experiment Involving Human Samples," *Journal of Magnetic Resonance,* vol. 34, pp. 425-433, 1979.
[14] J. Kurhanewicz, D. B. Vigneron, K. Brindle, E. Y. Chekmenev, A. Comment, C. H. Cunningham*, et al.*, "Analysis of cancer metabolism by imaging hyperpolarized nuclei: prospects for translation to clinical research," *Neoplasia,* vol. 13, pp. 81-97, Feb 2011.
[15] J. Ruiz-Cabello, B. P. Barnett, P. A. Bottomley, and J. W. Bulte, "Fluorine (19F) MRS and MRI in biomedicine," *NMR Biomed,* vol. 24, pp. 114-29, Feb 2011.
[16] J. B. Ra, S. K. Hilal, and C. H. Oh, "An algorithm for MR imaging of the short T2 fraction of sodium using the FID signal," *J Comput Assist Tomogr,* vol. 13, pp. 302-9, Mar-Apr 1989.
[17] D. I. Hoult, S. J. Busby, D. G. Gadian, G. K. Radda, R. E. Richards, and P. J. Seeley, "Observation of tissue metabolites using 31P nuclear magnetic resonance," *Nature,* vol. 252, pp. 285-7, Nov 22 1974.
[18] B. M. Goodson, "Nuclear magnetic resonance of laser-polarized noble gases in molecules, materials, and organisms," *J Magn Reson,* vol. 155, pp. 157-216, Apr 2002.
[19] C. Z. Cooley, J. P. Stockmann, B. D. Armstrong, M. Sarracanie, M. H. Lev, M. S. Rosen*, et al.*, "Two-dimensional imaging in a lightweight portable MRI

scanner without gradient coils," *Magnetic Resonance in Medicine,* vol. 73, pp. 872-883, 2015.

[20] A. Macovski and S. Conolly, "Novel approaches to low-cost MRI," *Magn Reson Med,* vol. 30, pp. 221-30, Aug 1993.

[21] R. D. Venook, N. I. Matter, M. Ramachandran, S. E. Ungersma, G. E. Gold, N. J. Giori*, et al.*, "Prepolarized magnetic resonance imaging around metal orthopedic implants," *Magn Reson Med,* vol. 56, pp. 177-86, Jul 2006.

[22] J. l. Mispelter, M. Lupu, and A. Briguet, *NMR probeheads for biophysical and biomedical experiments : theoretical principles & practical guidelines*. London: Imperial College Press, Distributed by World Scientific, 2006.

[23] L. Darrasse and J. C. Ginefri, "Perspectives with cryogenic RF probes in biomedical MRI," *Biochimie,* vol. 85, pp. 915-37, 2003.

[24] M. Rudin, *In-Vivo Magnetic Resonance Spectroscopy I: Probeheads and Radiofrequency Pulses Spectrum Analysis*. Berlin, Heidelberg: Springer Berlin Heidelberg,, 1992.

[25] W. A. Edelstein, G. H. Glover, C. J. Hardy, and R. W. Redington, "The intrinsic signal-to-noise ratio in NMR imaging," *Magn Reson Med,* vol. 3, pp. 604-18, Aug 1986.

[26] P. Mansfield and P. G. Morris, *NMR imaging in biomedicine*. New York: Academic Press, 1982.

[27] L. D. Landau and E. M. Lifshitz, *The classical theory of fields*, 3d rev. English ed. Oxford, New York,: Pergamon Press, 1971.

[28] S. M. Wright, "Full-wave analysis of planar radiofrequency coils and coil arrays with assumed current distribution," *Concepts in Magnetic Resonance,* vol. 15, pp. 2-14, Mar 2002.

[29] J. Tropp, "Image brightening in samples of high dielectric constant," *J Magn Reson,* vol. 167, pp. 12-24, Mar 2004.

[30] B. H. Suits, A. N. Garroway, and J. B. Miller, "Surface and gradiometer coils near a conducting body: the lift-off effect," *J Magn Reson,* vol. 135, pp. 373-9, 1998.

[31] C. E. Hayes and L. Axel, "Noise Performance of Surface Coils for Magnetic-Resonance Imaging at 1.5-T," *Medical Physics,* vol. 12, pp. 604-607, 1985.

[32] D. Lu, "Flexible RF coils for MRI system," US 5548218 A, 1996.

[33] P. H. Chan and M. X. Zou, "Flexible multi-section MRI radio frequency array coil," USA Patent US 6650926 B1, 2003.

[34] H. Fujita, P. H. Chan, D. Chu, J. Murphy-Boesch, L. S. Petropoulos, and M. X. Zou, "Coil arrays for parallel imaging in magnetic resonance imaging," 2005.

[35] S. Vasanawala, T. Grafendorfer, P. Calderon, G. Scott, M. Alley, M. Lustig*, et al.*, "Millimeter Isotropic Resolution Volumetric Pediatric Abdominal MRI with a Dedicated 32 Channel Phased Array Coil," presented at the International Socieity of Magentic Resosnance and Medicine 19, Montreal, Canada, 2011.

[36] G. Adriany, P. F. Van de Moortele, J. Ritter, S. Moeller, E. J. Auerbach, C. Akgun*, et al.*, "A geometrically adjustable 16-channel transmit/receive transmission line array for improved RF efficiency and parallel imaging performance at 7 Tesla," *Magn Reson Med,* vol. 59, pp. 590-7, Mar 2008.

[37] J. Rousseau, P. Lecouffe, and X. Marchandise, "A new, fully versatile surface coil for MRI," *Magn Reson Imaging,* vol. 8, pp. 517-23, 1990.
[38] J. A. Malko, E. C. McClees, I. F. Braun, P. C. Davis, and J. C. Hoffman, Jr., "A flexible mercury-filled surface coil for MR imaging," *AJNR Am J Neuroradiol,* vol. 7, pp. 246-7, Mar-Apr 1986.
[39] J. A. Nordmeyer-Massner, N. De Zanche, and K. P. Pruessmann, "Stretchable coil arrays: application to knee imaging under varying flexion angles," *Magn Reson Med,* vol. 67, pp. 872-9, 2012.
[40] F. Hwang and D. I. Hoult, "Automatic probe tuning and matching," *Magn Reson Med,* vol. 39, pp. 214-222, Feb 1998.
[41] S. M. Sohn, L. DelaBarre, J. T. Vaughan, and A. Gopinath, "8-Channel RF Head Coil of MRI with Automatic Tuning and Matching," *2013 Ieee Mtt-S International Microwave Symposium Digest (Ims),* 2013.
[42] L. T. Muftuler, G. Gulsen, K. D. Sezen, and O. Nalcioglu, "Automatic tuned MRI RF coil for multinuclear imaging of small animals at 3T," *Journal of Magnetic Resonance,* vol. 155, pp. 39-44, Mar 2002.
[43] A. C. Arias, J. D. MacKenzie, I. McCulloch, J. Rivnay, and A. Salleo, "Materials and applications for large area electronics: solution-based approaches," *Chem Rev,* vol. 110, pp. 3-24, 2010.
[44] F. C. Krebs, "Polymer solar cell modules prepared using roll-to-roll methods: Knife-over-edge coating, slot-die coating and screen printing," *Solar Energy Materials and Solar Cells,* vol. 93, pp. 465-475, Apr 2009.
[45] C. D. Muller, A. Falcou, N. Reckefuss, M. Rojahn, V. Wiederhirn, P. Rudati*, et al.*, "Multi-colour organic light-emitting displays by solution processing," *Nature,* vol. 421, pp. 829-833, Feb 20 2003.
[46] H. Yan, Z. H. Chen, Y. Zheng, C. Newman, J. R. Quinn, F. Dotz*, et al.*, "A high-mobility electron-transporting polymer for printed transistors," *Nature,* vol. 457, pp. 679-U1, Feb 5 2009.
[47] A. Pierre, M. Sadeghi, M. M. Payne, A. Facchetti, J. E. Anthony, and A. C. Arias, "All-printed flexible organic transistors enabled by surface tension-guided blade coating," *Adv Mater,* vol. 26, pp. 5722-7, Aug 27 2014.
[48] G. Schwartz, B. C. Tee, J. Mei, A. L. Appleton, H. Kim do, H. Wang*, et al.*, "Flexible polymer transistors with high pressure sensitivity for application in electronic skin and health monitoring," *Nat Commun,* vol. 4, p. 1859, 2013.
[49] D. H. Kim, J. H. Ahn, W. M. Choi, H. S. Kim, T. H. Kim, J. Z. Song*, et al.*, "Stretchable and foldable silicon integrated circuits," *Science,* vol. 320, pp. 507-511, Apr 25 2008.
[50] S. L. Swisher, M. C. Lin, A. Liao, E. J. Leeflang, Y. Khan, F. J. Pavinatto*, et al.*, "Impedance sensing device enables early detection of pressure ulcers in vivo," *Nat Commun,* vol. 6, p. 6575, 2015.
[51] C. M. Lochner, Y. Khan, A. Pierre, and A. C. Arias, "All-organic optoelectronic sensor for pulse oximetry," *Nat Commun,* vol. 5, p. 5745, 2014.
[52] F. C. Krebs, "Fabrication and processing of polymer solar cells: A review of printing and coating techniques," *Solar Energy Materials and Solar Cells,* vol. 93, pp. 394-412, 2009.

[53] D. Mager, A. Peter, L. D. Tin, E. Fischer, P. J. Smith, J. Hennig*, et al.*, "An MRI receiver coil produced by inkjet printing directly on to a flexible substrate," *IEEE Trans Med Imaging,* vol. 29, pp. 482-7, 2010.

[54] M. G. Erickson, K. N. Kurpad, J. H. Holmes, and S. B. Fain, "TEM transmission line coil with double nuclear capability," *Magn Reson Med,* vol. 58, pp. 800-7, Oct 2007.

[55] R. A. G. Horch, J.C., "3D-Printed RF Coils for solution-state NMR: Towards low-cost, high-throughput arrays," in *ISMRM 2015*, Toronto Canada, 2015.

Chapter 2

2. Coil Characterization

2.1 Introduction

In the previous chapter important coil parameters such as quality factor (Q) and image signal-to-noise ratio (SNR) were introduced. However, many factors can influence coil Q or image SNR so a full understanding of the experimental setup and measurement is needed. This chapter describes the factors that can impact the characterization of a coil and how to account for them. First, an overview of MRI phantoms for coil testing is described. Then, several electrical characterization techniques using a vector network analyzer are detailed. Finally, aspects of scanner setup, connection, and data interpretation are explained. Using the techniques described in this chapter the Q and image SNR from a coil can be measured reliably.

2.2 Phantoms for Characterization

Several coil measurements depend on loading a coil with a conductive sample. In a scanner, the sample is the patient being imaged, however the inherent variation of the electric properties of living tissue makes volunteers poorly suited for reliably and consistently characterizing coil performance. For example, the conductivity between two volunteers in the same area of the body can vary by almost an order of magnitude depending on the tissue composition [1-3]. Even if the measurements are done on the same person in the same position, changes in tissue conductivity due to varying hydration levels can significantly change the coil response. To address this issue, the coil characterization is performed using a stable, reproducible, and homogeneous phantom.

Since the coils are designed for a specific application, it is important to have a phantom that is representative of the tissue the coil is used on. Conductivity and dielectric constants vary widely throughout the body. At the extremes are cortical bone showing an average of 0.092 S/m with a relative dielectric constant of 14.9 and fluid in the eyes at 1.83 S/m with a dielectric constant of 74 [1-3]. Air in the body can also significantly impact the local conductivity and the dielectric constant. For example, the average dielectric constant near the lungs is much lower than it is in the rest of the chest due to the low conductivity and dielectric constant of air. Fortunately, a phantom with a conductivity of 0.67 S/m is sufficient to approximate most areas of the body [1-3]. Ideally the phantom would have a relative dielectric constant near 50 [1-3], however for most setups it is more practical to use water, which has a dielectric constant of 80 at 37 °C. This difference causes a small shift in the loaded resonance frequency, particularly if the coils are very close to the sample, but it is usually negligible.

The most commonly used phantoms consist of solutions of deionized water, salt, and other ionic solutions because of its ease of manufacturing, stability, and availability of components [4, 5]. Phantoms comprised of an agar gel may also be used, but are more complex to fabricate [6, 7]. A phantom comprising of only water and salt would provide

an accurate representation of the tissue conductivity to tune the coils, but would have very long relaxation times that poorly represent those seen in most soft tissues. To create a phantom with a relaxation time closer to soft tissue, copper, chlorine, manganese, nickel, or gadolinium ions can be added to the solution [4, 5, 8]. A practical strategy is to first select the target concentration of ions for a certain tissue relaxation time and then add salt (NaCl) to reach the desired conductivity. Target relaxation times for various tissues are available in Kato, et al, Pykett et. al, and Morgan et al. [4, 5, 8]. The conductivity of a solution can be verified by comparing the Q_{Loaded} response of a coil loaded with a phantom to the response of the same coil located on the area of the body that will be imaged – more detail on measuring Q_{Loaded} is available in section 2.3.2.

The vessel that holds the phantom material is usually a non-conductive polymer or glass container. The materials commonly used for containers are polyethylene, polycarbonate, and acrylic due to their low MR signal. It is important to note that these plastic containers are not completely impervious to water causing it to evaporate and diffuse out through the walls over time. Since the materials used to dope the phantom do not escape with the water, the phantom becomes more conductive. This process is much slower than the length of a scanning session and can be easily corrected by adding more deionized water before scanning or replacing the solution every few months.

The phantom used in this work is a water filled 7L cubic phantom doped with 3.356 g/L $NiCl_2*6H_20$ and 2.4 g/L NaCl for conductivity of 0.68 S/m at 123 MHz. The acrylic walls of the phantom are 6.4 mm thick.

2.3 Electrical Characterization

To accurately characterize the sources of loss in a coil, experimental setup must only measure the losses in the system due to coil materials and sample composition. However, the measurement environment also influences the electrical response of a coil. To minimize the unintended interactions with the measurement environment the following sections describe the theory, tools, and methods used to characterize a coil.

2.3.1 Scattering and Impedance Parameters

The properties of electrical circuits and components are normally described using complex impedance. To characterize a circuit's impedance at DC and low frequency, voltages and currents can be easily measured. However, at the frequencies that MR scanners operate at and the size of coils that are measured, measuring the impedance directly with the test equipment is more complicated due to the lack of a true open or short circuit reference at these frequencies. At frequencies common to MRI, any gap making an open circuit possess a non-negligible capacitance and any wire used to produce a short circuit possess a finite inductance [9, 10]. Furthermore, the amplifying circuits used in coil design are unstable if they are loaded by open or short circuits so other means are needed to accurately characterize the impedance.

To address this problem the device under test, also referred to as a network, can be characterized using the response of incident waves, particularly by measuring the magnitude and phase of the transmitted and reflected signal. The transmitted and reflected waves are compared with the incident wave to create a matrix of scattering

parameters that is used to describe the device under test. Figure 2.1 shows a common configuration detailing the scattering parameters for a 2-port network. In Fig. 2.1, incident waves originating at each port interact with the network and transmit or reflect back to each port. For example, a wave (represented by an arrow) injected in port 1 and reflected back to port 1 would be used to calculate S_{11} and any wave transmitted through to port 2 from port 1 is used to calculate S_{21} (and likewise for any wave originating from port 2). This procedure of comparing incident and response waves can also be extended to a many port network [10].

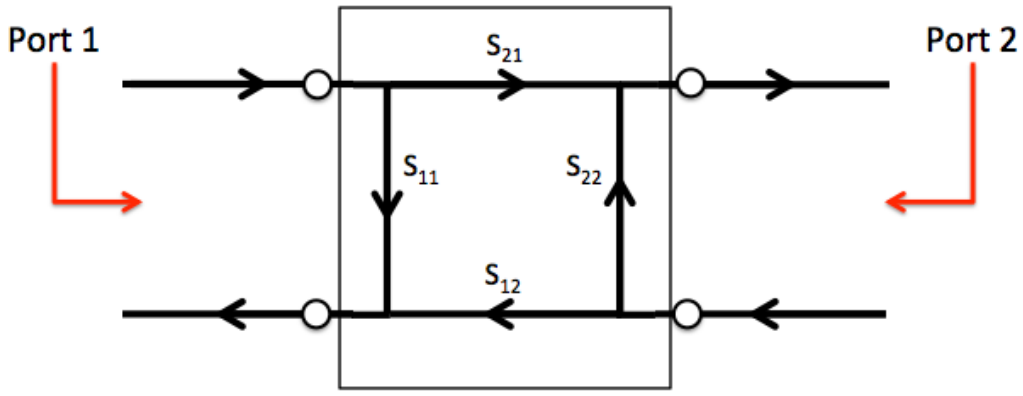

Figure 2.1: Scattering parameters from a general 2-port network. The scattered waves from ports 1 and 2, represented by arrows, are shown as the scattering parameters S_{11}, S_{12}, S_{21}, S_{22}.

If the scattering parameters and the characteristic impedance (Z_0) of the test port are known, it is possible to calculate the impedance of the network using equations 2.1-2.4 [9].

$$Z_{11} = Z_0 \frac{(1+S_{11})(1-S_{22})+S_{12}S_{21}}{(1-S_{11})(1-S_{22})-S_{12}S_{21}} \qquad (2.1)$$

$$Z_{12} = Z_0 \frac{2S_{12}}{(1-S_{11})(1-S_{22})-S_{12}S_{21}} \qquad (2.2)$$

$$Z_{21} = Z_0 \frac{2S_{21}}{(1-S_{11})(1-S_{22})-S_{12}S_{21}} \qquad (2.3)$$

$$Z_{22} = Z_0 \frac{(1-S_{11})(1+S_{22})+S_{12}S_{21}}{(1-S_{11})(1-S_{22})-S_{12}S_{21}} \qquad (2.4)$$

The scattering parameters are obtained by probing the device under test with a vector network analyzer (VNA), however accurate scattering parameters require special attention to the equipment setup, particularly with the position of the device under test to any nearby conductor. Placing the device under test near any conductive material, or any tuned loop of wire will cause the device to couple to it and change its properties. The

following sections examine some of the most commonly used setups to measure coils. A detailed reference to general VNA setup can be found in Dunsmore et al. [11].

2.3.2 Quality Factor Measurement

A common way to characterize the properties of a resonant circuit, such as a coil, is to measure the system's quality factor (Q). Q is simply a relationship between the real resistance, Re[Z], from a system compared to any imaginary reactance, Im[Z], as shown in equation 2.5. Resistance accounts for the energy lost in the form of heat while reactance quantifies any energy stored in an electric or magnetic field. For example, a coil with high Q indicates that there is not much loss in the system compared to the amount of energy the coil can store in an electric or magnetic field.

$$Q = \frac{Im[Z]}{Re[Z]} = \frac{Energy\ Stored}{Energy\ Lost} \qquad (2.5)$$

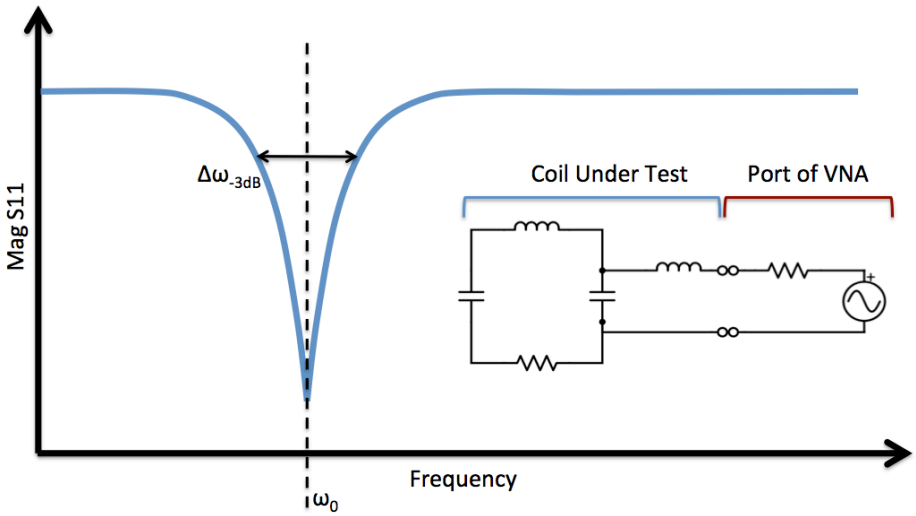

Figure 2.2: Illustration detailing calculation of quality factor for a surface coil by direct S_{11} measurements. Inset shows the resistance of the port that will dissipate half of the power, artificially lowering the measured Q.

Q can be measured by connecting the coil to a port on the network analyzer, however, to get an accurate measurement, the coil must be tuned to show exactly the impedance of the test port – typically 50 Ω. If the coil is mismatched, some of the energy will be lost as a reflection, artificially lowering the estimated Q. Figure 2.2 shows a typical S_{11} magnitude plot used to calculate Q. In Fig, 2.2 the full width half max point highlighted (or -3dB point on a log scale) of the S_{11} magnitude plot and center frequency (ω_0) of the resonance peak can be used to calculate Q as described by equation 2.6 [12]. For an MRI coil, the center frequency is the Larmor frequency of the scanner. However the loss from the matched port must also be accounted for. Since the coil is matched to the port, half of the power is dissipated in the port, the other half, in the coil; as a result the actual Q is twice as high than the reported Q [12]. The inset of Fig 2.2 shows the circuit that the coil makes with the port, note that the resistance of the port will influence the measurement by dissipating some power. This method is poorly suited for measuring a coil in and out

of the presence of a phantom since the coil will change impedance as it is loaded and will require retuning in both instances.

$$Q_{Matched_{S11}} = \frac{2\omega_0}{\Delta\omega_{-3dB}} \qquad (2.6)$$

A different approach to measure coil Q is to lightly couple two broadband probes to the coil. In this setup, one probe transmits while the other receives any signal radiated by the coil under test. Figure 2.3 shows an example S_{21} magnitude plot produced using this method. Similar to the previous method, the Q can then be measured from the width of the 3dB point and the center frequency using equation 2.7 [12]. The coils are considered lightly coupled if the magnitudes of the S_{11} or S_{22} response are less than -100 mdB (approximately 1% coupled). If the coils are heavily coupled (i.e, the S_{11} or S_{22} magnitude is greater than -100 mdB), then the loss from the probes will be reflected on the measurement resulting in inaccurate readings. The probe must also be decoupled from each other to ensure that the probes are only measuring the response of the coil. This decoupling can be accomplished by separating the probes by a distance of several coil diameters, or critically overlapping them as it is shown in the inset of in Fig 2.3. Without a coil present, the probes should show an S_{21} response of approximately -70 dB [13].

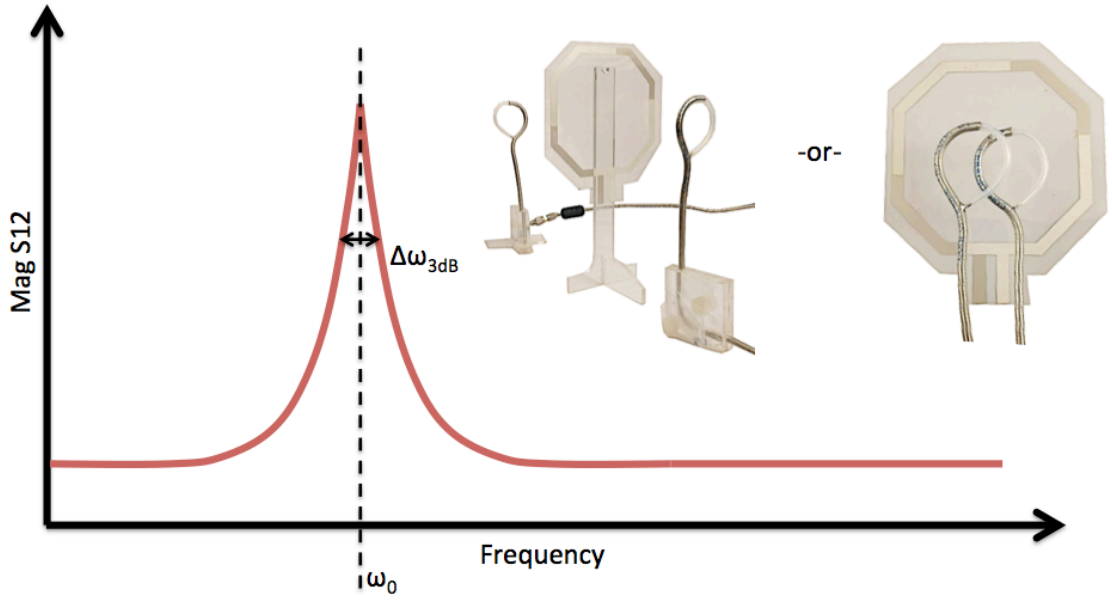

Figure 2.3: Setup and measurement of a surface coil's quality factor by an S_{21} measurement. Insets show two possible decoupling configurations used to perform the measurement. This technique does not require any special preparation of coil input impedance.

$$Q_{S12} = \frac{\omega_0}{\Delta\omega_{3dB}} \qquad (2.7)$$

For either of the two previously mentioned techniques for measuring Q, external factors to the measurement setup can affect the result. To ensure that the surrounding

environment is not influencing the Q measurements, the experimental setup should not contain any conductor close to the coil, including the operator. Keeping a coil 10 diameters away from conductive materials will ensure that the contribution from the environment is less than 0.01%, but even a distance of 5 coil diameters will produce a contribution of 0.1% [14]. Several ferrite beads can be inserted onto the outside of the cables near the connectors to remove the interaction of currents that may be on the outside of the cable.

An incorrect characterization can occur if the network analyzer is not set up properly for the measurement. If measuring a system with Q greater than 100, the network analyzer frequency sweep must have a sufficient number of measurement points to correctly measure Q. If an insufficient amount of measurement points are used in a frequency sweep, a low Q might be displayed artificially high. For example, a frequency sweep that uses only 400 measurement points will report a Q of 410 while one that uses 1600 will measure a more accurate Q of 273. It is also strongly recommended that the analyzer be averaged over several sweeps to reduce the measurement variation [11].

One often-overlooked source of error is the calibration standards and cables used with the network analyzer. One practical method to eliminate this source of error is to calibrate the tool with two different open, short, and load standards at least once to ensure that the calibration is correct. Additionally, the stability of cables can be checked by observing the phase of the signal as cables are moved around. If large variations are seen while flexing the cable the cable is worn out and needs to be replaced [11].

2.3.3 Input Impedance Measurement

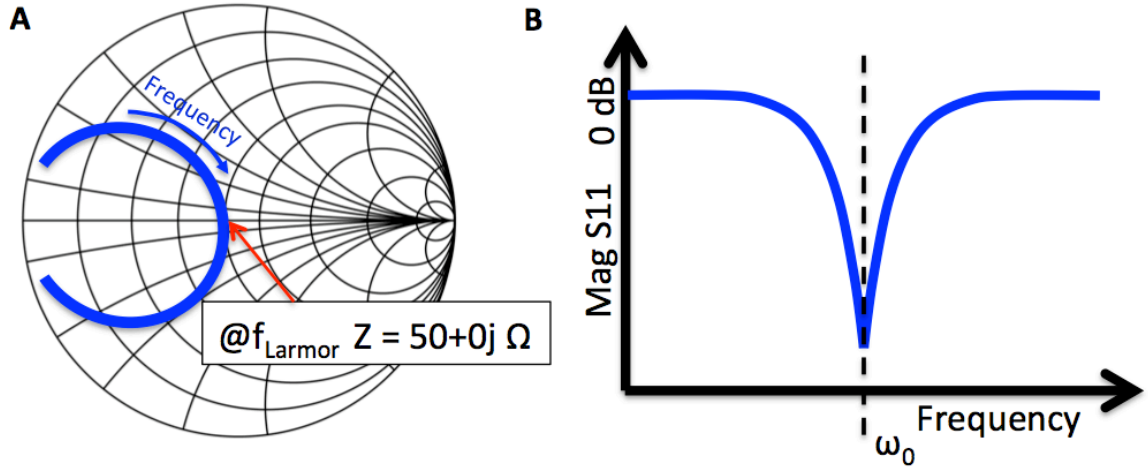

Figure 2.4: **A.** Smith chart of the coil impedance matched to 50 Ω at the Larmor frequency **B.** Magnitude of S_{11} response for a properly tuned coil showing minimum response at the Larmor frequency.

The coil input impedance can be measured by directly connecting the coil to one port of a network analyzer to simulate the connection to a scanner. A representative phantom is used to load the coil to accurately reflect the conditions that will be used during the scan. The composition and placement of the phantom will change the loading of the coil and affect the input impedance. A useful way to view the input impedance of a coil is by using a Smith chart, which represents the real and imaginary parts of the impedance over

a span of frequencies and it is exemplified in Figure 2.4 A. Each arc represents a constant resistance as the imaginary portion of the impedance changes. The center of the Smith chart represents 50 Ω without any imaginary portion. The far left and right of the circle represent a short and an open circuit, respectively. To match the coil, the input impedance must be at the center of the circle at the Larmor frequency. If a coil is matched to 50 Ω, then the magnitude of the S_{11} plot, shown in Fig. 2.4 B, will be at a minimum at the Larmor frequency.

2.3.4 Blocking Impedance Measurement

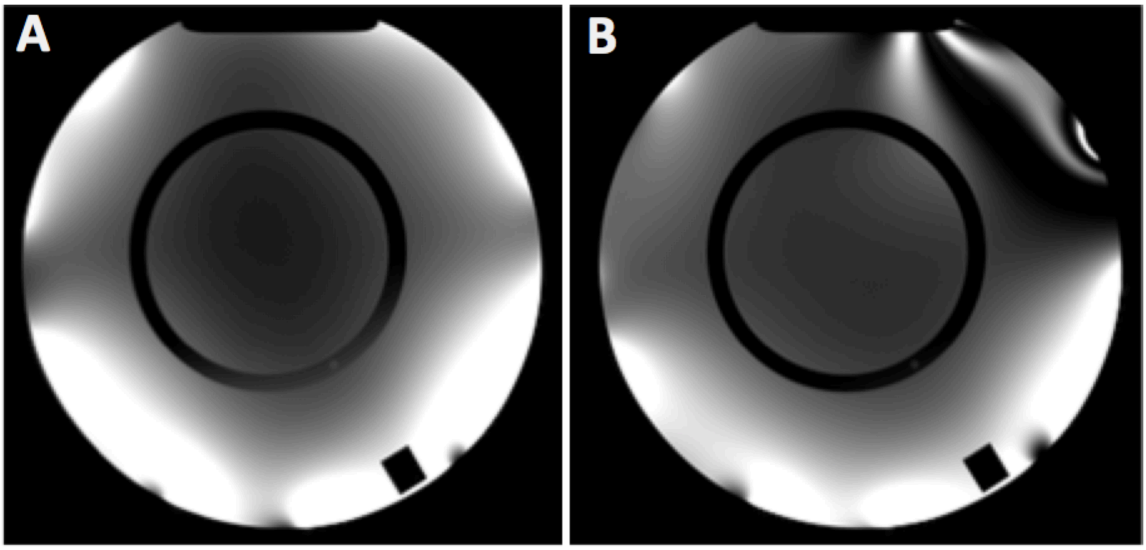

Figure 2.5: Images of phantom with (**A**) a properly functioning blocking circuit and (**B**) a non-functioning blocking circuit. The incorrectly spoiled surface coil is significantly distorting the excitation field resulting in banding artifacts.

The magnitude of the impedance that the blocking circuit (described previously in section 1.4.3) must provide depends on the frequency of operation, the size of the receive coil, and the type of the block [15]. A blocking circuit is sufficient if the coil does not distort the RF excitation pulse (B_1) by more than 5%. For a purely resistive type block, the minimum blocking impedance per area of the coil (Z_l/S) can be determined by equation 2.8 from Fraser et al. using only the Larmor frequency (f_o) of the scanner [16]. For example, a coil operating at 3T requires a minimum blocking impedance of 32 ohms/cm^2. There are methods to reduce the blocking impedance requirement, such as inductively tuning the blocking circuit or using a smaller coil. Large blocking values are achieved by implementing an additional blocking circuit. To illustrate the effects of a good and poorly performing blocking circuit, Fig. 2.5 shows an image of a cylindrical phantom acquired with an 8-channel surface array. In Fig 2.5 A, a clear image of the phantom is seen, while Fig. 2.5 B shows significant banding artifacts from an incorrectly tuned blocking circuit from the top right element of the 8-channel array. It is possible for a blocking circuit to be slightly mistuned producing less pronounced banding artifacts, but ideally none should be present.

$$\left.\frac{|Z_l|[Ohm]}{S[cm^2]}\right|_{5\%} \approx \frac{1}{4} f_0[MHz] \qquad (2.8)$$

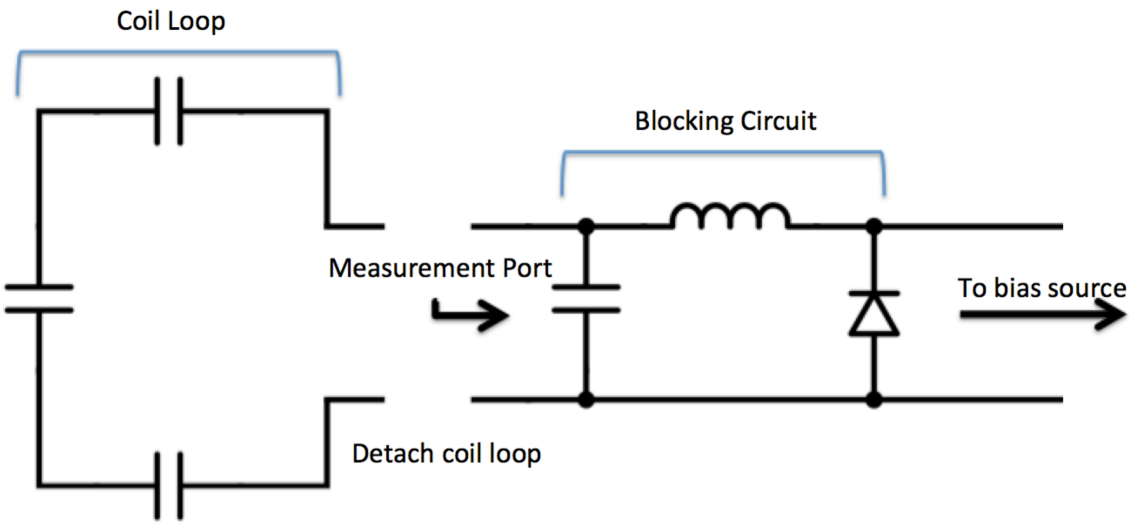

Figure 2.6: Diagram detailing the locations of the measurement port and the bias source to perform the blocking circuit tuning and characterization. Coil loop is detached from the blocking circuit characterization to prevent coil from coupling to the blocking network.

To measure the blocking impedance, the impedance across the matching capacitor is recorded. However, if the matching capacitor is left connected to the main coil, the tuned coil loop will couple to the blocking circuit and affect the measurement. To prevent this, the blocking circuit must be detached from the coil. Figure 2.6 shows the correct location to measure a blocking circuit with the coil detached. A voltage is applied to the blocking circuit to bias the diode and form the trap circuit between the matching capacitor and the inductor described previously in section 1.4.3. If measuring with a standard network analyzer, a DC blocking bias-tee network is needed inline with the port to prevent damage to the analyzer. The resonant frequency of the blocking circuit is tuned by changing the value of the in-series inductor.

2.3.5 Balun Impedance Measurement

As previously described in section 1.4.5, a balun is a resonant trap circuit that prevents current on the outside of a cable. It possesses a limited bandwidth so it must be resonant at the correct frequency. The frequency and the magnitude of the impedance provided by the balun can be characterized by probing the balun with the network analyzer. Several methods to characterize balun resonant frequency and input impedance are described below.

If the magnitude of the balun impedance has been characterized previously, as in the case when tuning a known design for a production array, only the center frequency of the balun needs to be measured. To quickly characterize this, a multi-turn loop can be used to

probe the balun. Figure 2.7 shows how the multi-turn probe is brought near the balun to couple to it and probe the resonant frequency of the balun. If an accurate characterization of the blocking impedance is desired, such as with a new prototype balun, other characterization techniques must be used such as those described in the following paragraphs.

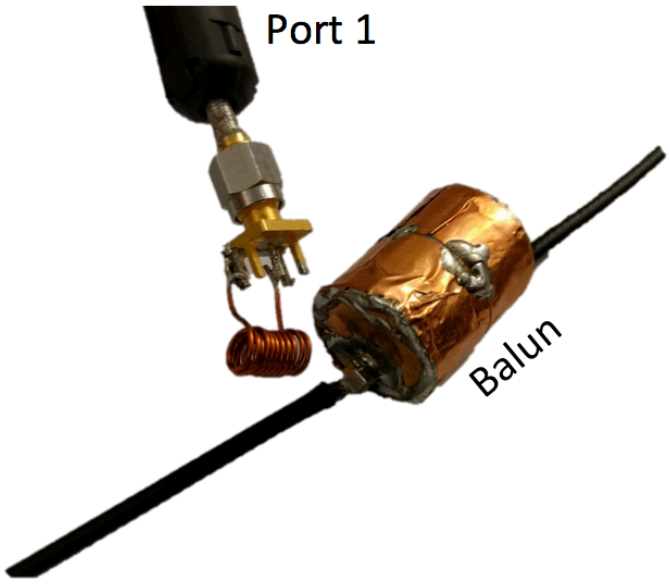

Figure 2.7: Photograph illustrating the multi-turn probe measurement of the balun center frequency.

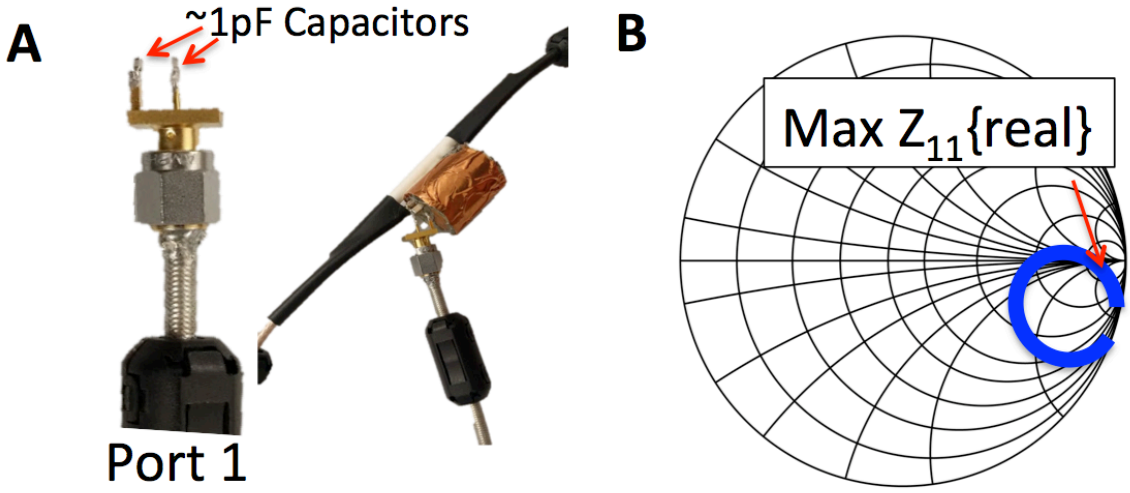

Figure 2.8 **A.** Photograph showing the setup used for the balun input impedance measurement by making contact across the tuning capacitor. **B.** Smith chart illustrating the location of the maximum real impedance of the balun using a capacitor tipped probe.

Figure 2.8 A illustrates one method to probe a balun and characterize the blocking impedance. In this figure, direct contact to the balun is made across the capacitor of the balun with two small capacitors (≥ 2pF) on top of a calibrated probe measuring S_{11}. The low value capacitors on the tip of the probe ensure that the probe is only lightly coupled to the balun, preventing the 50 Ω impedance of the port from changing the response of the balun. The capacitors on the probe only contribute to the reactive portion of the reported impedance, while the real portion of the balun's impedance is the main interest. Since the capacitors only affect the imaginary portion of the impedance, the magnitude of the real portion of the impedance value can be obtained with a Smith chart. Figure 2.8 B illustrates an approximate location of the maximum point of the real impedance using this method on a Smith Chart. The magnitude of the real portion of the impedance is the impedance of the balun.

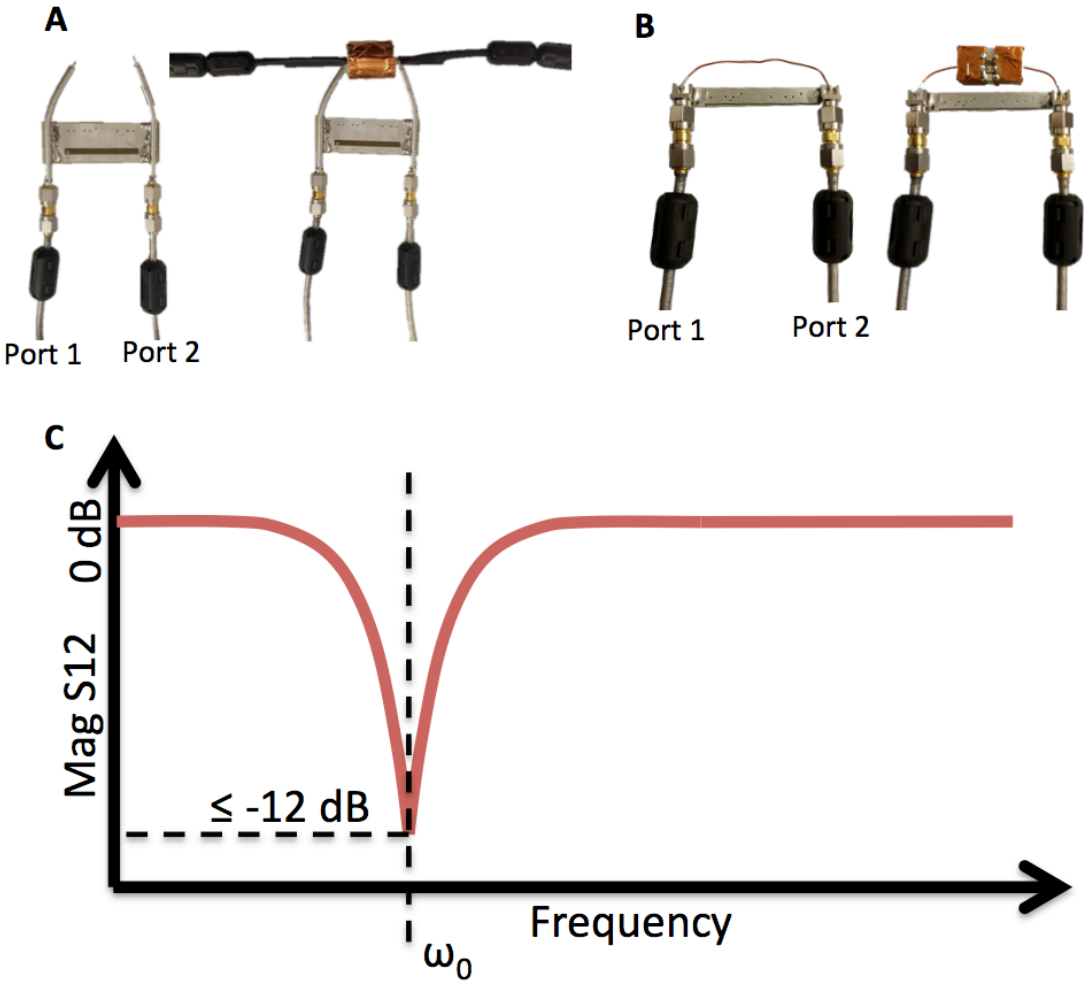

Figure 2.9 **A.** Photograph of the measurement setup to make momentary contact across the balun with an S_{12} probe and characterize the impedance. **B.** Photograph of the measurement setup used to measure the balun attenuation by an inductively coupled S_{12} probe. **C**. Typical S_{12} response of a tuned balun highlighting the location and magnitude of the center frequency.

Another way to characterize a balun is to measure the amount of signal transmitted through it by probing the outside of the cable. Figure 2.9 A shows how this is accomplished using two segments of a stripped coaxial cable to make momentary contact on each side of the balun. As the network analyzer probes the balun across a span of frequencies, the balun will attenuate any current on the outside of the cable at the balun's center frequency with a certain magnitude. The S_{12} response is then used to obtain the magnitude and the center frequency of the balun's attenuation. Equations 2.2 and 2.3 can then be used to calculate the impedance. During this measurement it is necessary to isolate the balun from the rest of the cable. One way to isolate the balun without cutting the cable is to place ferrite chokes around the balun, seen as black nodes on the cables in Fig 2.9 A. A special case may arise if the impedance from the ferrite choke is significantly lower than the balun under test. In this case, a non-negligible amount of current can flow through the isolation chokes and to other portions of the circuit, invalidating the measurement. One way to check if this is occurring is to measure a resistor with a similar impedance to the balun and see if the impedance analysis matches the value.

In addition to the methods previously described, an inductively coupled balun can be characterized by placing it on a solid copper wire that is connecting port 1 and 2 of a network analyzer, as shown in Fig. 2.9 B. As the network analyzer transmits signal from port 1 to port 2, the balun will block the signal in the same way it would if it was connected to a cable in a scanner. Figure 2.9 C shows an example S_{12} magnitude response for a balun probed in this way. Here, the trace can be used to calculate both center frequency and blocking magnitude. The location and magnitude of the dip in S_{21} correspond to the resonant frequency and magnitude of the attenuation respectively. Usually it is the case that nearly all the flux from the balun is coupled to the cable (i.e., the coupling coefficient is near 1), therefore the blocking impedance can be calculated directly using equations 2.2 and 2.3 similar to the previous methods.

2.4 Scanning

Measuring the electrical performance of coils is a convenient procedure to estimate how the coils will perform in a scanner, but ultimately the SNR needs to be measured from images to obtain a complete characterization. This section discusses the details of characterizing coils on an MR scanner.

2.4.1 Connecting to Coils to a Scanner

A connection between the coil and the cable leading to the scanner is needed to acquire images. However, if the properties of this interface change during handling or mechanical vibration, it will result in artifacts in the image that will prevent an accurate coil characterization. The composition of this interface is particularly important because any mechanical stress from the cable or the coil is usually focused here. In traditional coils, this connection is created using locking screw-on connectors such as sub-micro type A (SMA), sub-micro type P (SMP), or Bayonet Neill–Concelman (BNC) connectors. These connectors are appropriate for traditional coils, but they are not always possible to implement in a coil that is thin and flexible.

Artifacts can occur in images if the connection to coils is poor or intermittent. To illustrate this effect, an intermittent connection that makes poor contact to a coil is examined. Figure 2.10 A shows a photograph of a coil that uses a loose fitting alligator clip that moves during scanning. This loosely fitting clip results in spiking (very high values causing the saturation of a pixel) in the k-space as the data is acquired on the scanner. These impulses in k-space manifest as sine waves over the image because the Fourier transform of an impulse is a sine [17]. Examples of images with this spiking artifact on a phantom and volunteer are shown in figure 2.10 B and C, where it is possible to observe alternate bands of bright and low signal across the images.

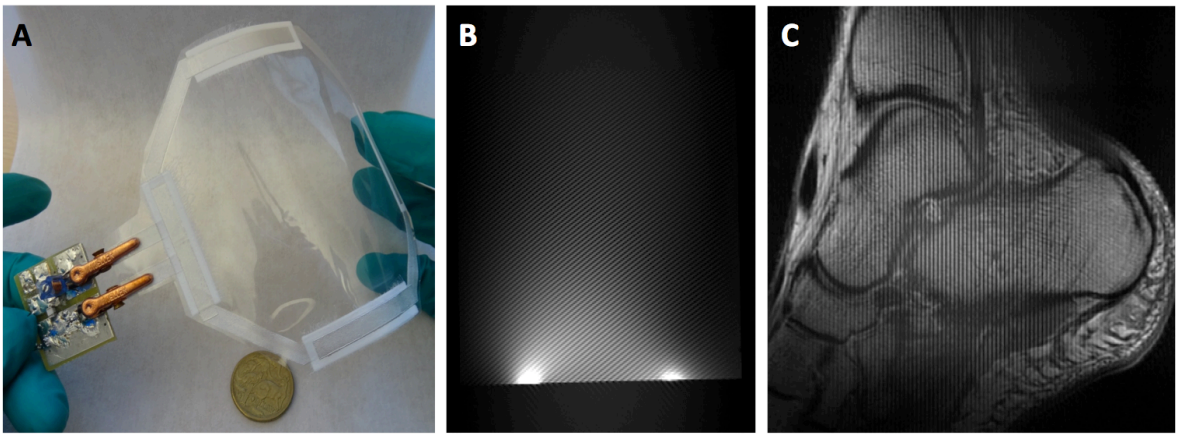

Figure 2.10: **A.** Photograph of a coil design connected to the scanner by a loose clamping alligator clips. **B.** Image of a phantom and **C** of a volunteer illustrating sine wave artifacts caused by the spiking educed by ineffective coil connection.

Other connection methods can be used to provide stable and reliable contact to a flexible coil. Connectors such as clamps, crimps, rivets, or brass bolts can make solid contact to the coils without significantly stressing this fragile area. Traditional flexible circuit board connectors could also be used, but they typically do not perform as well as the purpose built ones described in this thesis.

Mechanical fasteners such as rivets or brass bolts, respectively pictured in figure 2.11 A and B, can be used if the coil is on a static phantom. Both of these techniques can fail if the cable is pulled hard, but both methods are quick to implement and work well for imaging non-moving phantoms. Adding a reinforcing encapsulation such as an epoxy or glue can strengthen these connections. Figure 2.11 B shows a transparent epoxy encapsulating the bolts to spread out the mechanical stress and prevent the bolts from loosening.

A clamping fixture like the one shown in Fig 2.11 C can be used if a removable connection is needed, such as when testing multiple coil configurations. The board shown contains a gold plated non-magnetic connector, PIN diode, and discrete inductor for tuning the blocking circuit. The photograph of this connector in Fig. 2.11 C details how the nylon bolts are used to clamp through the coil and board. This method is efficient for initial testing, but lacks the flexibility and the mechanical stability needed for a clinical coil.

The best solution developed in this work to join the thin coils to the scanner is to use a brass crimp to lock two conductive traces together. Figure 2.11 D illustrates this

connection with a copper strip that is folded over a printed trace then locked together with a brass crimp. This method of connection ensures low stress at the joint by using two materials that are equally flexible. Any stress is evenly distributed throughout the joint, making it less prone to break. An encapsulation layer can also be used to increase the reliability of this joint adding additional strength.

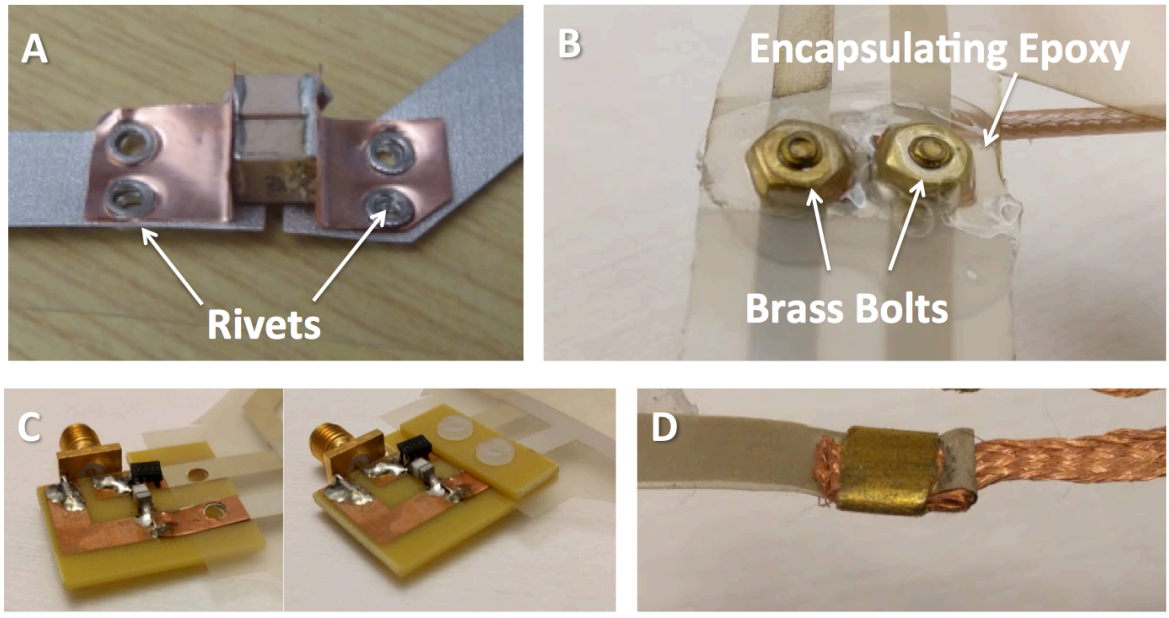

Figure 2.11: **A.** Photograph showing copper strips riveted to the printed coil. **B.** Photograph of the brass bolts clamping the coaxial cable to a printed coil **C.** Photographs showing the clamping board interfacing between printed and non-printed components for a single coil testing. A thin copper strip is soldered onto the board to make the top contact to the coil. **D**. Close up photograph showing the brass crimp used to join the printed array to the coaxial cables and copper braid.

2.4.2 Scanner setup

All clinical scanners perform an automatic pre-scan calibration that can change the gain of the system amplifiers along with the shim coils used to maintain the field uniformity in the system. If images from a scanner are used to compare two receive coils, it is recommended that the same gain and shim settings be used to obtain an accurate comparison.

Additionally, each scanner has a unique the center frequency due to slight variations of the main magnet. While there is some day-to-day variations in center frequency from the strength of the magnet drifting, it is usually negligible. However, between manufacturers there can be a wide deviation in the center frequency, particular between GE (f_{Larmor} = 127.73 MHz) and Seimens (f_{Larmor} = 123.32 MHz) 3T scanners. So coils that are designed to work on one system may not work correctly on another manufacturer's system. If the characterization on two different systems is desired, two different arrays must be built and tuned for an accurate comparison.

2.4.3 Image SNR

In clinical imaging, the signal in the MR image is usually much higher than the noise floor, making it easy to separate regions of noise from those containing signal. The SNR is calculated by using a ratio of signal to noise in an image. To define the noise portion of an image, a region of pixels in an image known to have no signal is used to calculate the standard deviation of the noise (σ_{noise}). A pixel or region of pixels containing signal is then used to define the signal (S). The SNR can then be estimated by using the relationship shown in equation 2.9 [18]. While the calculation itself is straightforward, there are some important details that must be considered when performing SNR analysis on images from a scanner.

$$SNR = \frac{S}{\sigma_{noise}} \qquad (2.9)$$

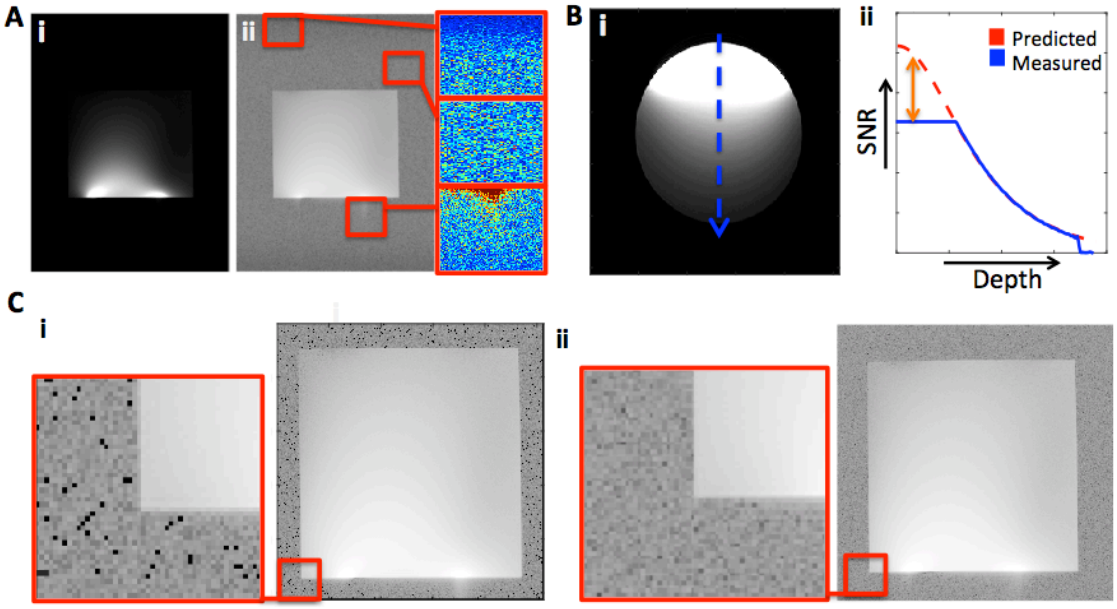

Figure 2.12: **A.** Magnitude image of a cubic phantom shown on a i. linear and ii. logarithmic scale. Insets show portions of signal or filtering extending into noise regions that could incorrectly bias the estimate of the standard deviation. Middle selection of noise provides accurate estimation of noise in the image. **B.** i. Compressed image of cylindrical phantom with ii. cutline of intensity shown. Orange line highlights discrepancy between predicted and measured signal. **C.** Log-magnitude images from compressed image (i.) and raw data image (ii.) produced by scanner.

Pixels chosen to estimate the noise must not contain any artifacts from nearby pixels containing signal. This is especially common if there is an abrupt transition between signal and no signal pixels – shown in the phantom image of Fig. 2.12 A. This streaking exists because the higher frequency components of the Fourier transform are not usually collected. This causes a Gibs ringing artifact across the image anywhere near an edge or corner [17].

Figure 2.12 A also shows the signal drop out added from the readout low pass filter of the scanner. These pixels near the edge of the image should not be used because they do not accurately represent the distribution of noise in the image. Both streaking and windowing artifacts may not be obvious under normal windowing, therefore it is recommended to display the log of the magnitude image in order to highlight any perturbations. When selecting a noise region, a sufficient amount of pixels (≥1000) is needed to accurately calculate the standard deviation [18]. A sample size that is too small results in an inaccurate standard deviation estimate. Figure 2.12 A also provides an example of an ideal uniform noise region to estimate the standard deviation of the noise.

By default, most clinical scanners will output images in a processed and compressed format that is easy for hospitals to manage. However, several issues arise if these images are used for characterizing coils. For example, Figure 2.12 B shows the signal being artificially low in a scan of a cylindrical phantom. The cross-section of the calculated SNR indicates a large discrepancy from what is expected for a coil sensitivity pattern and what is measured, leading to a gross underestimation of the SNR. This artifact is due to the limited dynamic range of the compressed images. Another problem with using the compressed images is that the noise regions in the image receive some level of filtering, causing an inaccurate representation of the standard deviation of the noise. As an example, figure 2.12 C shows a log-magnitude image of a cubic phantom from the (i) diagnostic image and (ii) raw data. The black spots around the cubic phantom represent noise regions outside the dynamic range of the compression sequence and are artificially set to zero. As a result, the regions of noise in the compressed image do not accurately represent the noise floor of the scan. To avoid these issues and accurately calculate SNR, the raw unformatted data must be taken from the scanner directly and used for the SNR calculation.

When measuring the SNR from a coil array an additional level of analysis must be used because the signal and the noise are spatially dependent. Normally, when combining several coil images into a single image this spatially varying information is lost. To correct for this, the sensitivity maps of each coil should be estimated with a technique such as ESPIRT [19] and then use with the noise correlation data to calculate the SNR. For this technique, the raw image data along with the noise-only images are needed.

Specifically, to calculate SNR from an array, methods from Roemer et al. [20] and Prussman et al. [21] are used. A summary of the methods proposed by Roemer and Prussman relevant to the arrays used in this thesis was done by Nordmerey-Massner et al. and is shown here in equations 2.9-2.15 [22]. Equation 2.8 defines the vector containing the complex image values that the different coils have for an individual pixel (d). This quantity depends on the coil sensitivity (S), the exact value of the transverse magnetization at the pixel's position (ρ) and the thermal noise contribution to that pixel (η) [22]. Equation 2.10 estimates the magnetization of a given pixel ($\hat{\rho}$) using A defined in equation 2.11 where Ψ is the noise covariance matrix. Superscript H indicates where the complex conjugate transpose should be taken, while (*) denotes the conjugate. To calculate the covariance matrix, equation 2.12 describes how noise only images acquired from a coil array with no RF excitation are used to estimate the noise correlation between the γth elements in an array [23]. Equations 2.9-2.12 can be combined resulting in equation 2.13, which estimates the pixel magnetization [22], note that this equation is simply a combination of the signal and noise portions of any given pixel.

$$\boldsymbol{d} = \boldsymbol{S}\rho + \boldsymbol{\eta} \quad (2.9)$$

$$\hat{\rho} = \boldsymbol{A}\boldsymbol{d} \quad (2.10)$$

$$\boldsymbol{A} = (\boldsymbol{S}^H\boldsymbol{\Psi}^{-1}\boldsymbol{S})^{-1}\boldsymbol{S}^H\boldsymbol{\Psi}^{-1} \quad (2.11)$$

$$\boldsymbol{\Psi}_{\gamma,\gamma'} = \eta_\gamma \eta_{\gamma'}{}^* \quad (2.12)$$

$$\hat{\rho} = \rho + \boldsymbol{A}\boldsymbol{\eta} \quad (2.13)$$

The variance of the noise component (σ^2) from equation 2.13 can then be calculated using equation 2.14. Combining equations 2.12 and 2.14 results in equation 2.16 which is a simplified expression for calculating the variance of the noise [22].

$$\sigma^2 = \boldsymbol{A}\boldsymbol{\psi}\boldsymbol{A}^H \quad (2.14)$$

$$\sigma^2 = (\boldsymbol{S}^H\boldsymbol{\Psi}^{-1}\boldsymbol{S})^{-1} \quad (2.15)$$

Equation 2.16 is obtained from combining equations 2.9-2.15 and it is used to estimate the SNR for a given array of coils. Equation 2.16 is only valid for high values of SNR, with a relative error following a trend of SNR^{-1} [22].

$$SNR = \frac{|\rho|}{(\boldsymbol{S}^H\boldsymbol{\Psi}^{-1}\boldsymbol{S})^{-1/2}} = \sqrt{\rho^*\boldsymbol{S}^H\boldsymbol{\Psi}^{-1}\boldsymbol{S}\rho} \approx \sqrt{\boldsymbol{d}^H\boldsymbol{\psi}^{-1}\boldsymbol{d}} \quad (2.16)$$

2.4.4 Location of the Preamplifiers

For the coils described in this thesis, half wavelength coaxial transmission lines are used to connect the coils to the preamplifiers. The preamplifiers then connect to the scanner. However, in commercial array designs, preamplifiers are usually located as close to the coil elements as possible in order to increase the SNR and by eliminating the matched-line attenuation loss from the connecting cable. For example, the matched transmission-line attenuation for a typical non-magnetic coaxial cable used in this thesis is 36db/100m (RG316). On a 3T system, this would mean that an 84 cm length of cable would attenuate the signal by 0.3 dB (~7%) [24].

This attenuation can actually be higher if the coil is no longer matched to 50 Ω, as is the case if the coil is in a different position than the one it was tuned in. To account for this mismatched line loss, the system voltage standing wave ratio (VSWR) can be measured to calculate the reflection coefficient using equation 2.17. The total mismatched line loss can then be calculated and accounted for with equation 2.18 [24] and used to estimate what the SNR would be if the preamplifiers were close to the coil.

$$|\rho| = \frac{VSWR-1}{VSWR+1} \quad (2.17)$$

$$Total\ Mismatched\ Line\ Loss = 10\log\left[\frac{a^2-|\rho^2|}{a(1-|\rho^2|)}\right] \qquad (2.18)$$

2.4.5 Coil Coupling

In an array of coils, there will always be some degree of coupling between each of the coil elements despite all mitigating efforts. The most straightforward method to characterize the isolation (i.e., the degree of coupling) between each channel of an array is to acquire noise-only images from each channel when there is no RF power or gradient pulses applied. The cross correlation (ρ_{cc}) of the noise in each channel can then be calculated using equation 2.19 from Duensing et al. [25] where N is the matrix of pixels from the noise-only image.

$$\rho_{cc} = \frac{\langle N_1 N_2 \rangle}{\langle N_1^2 \rangle \langle N_2^2 \rangle} \qquad (2.19)$$

For example, a commercial array that is far away from the sample typically presents noise correlation values of 0.1 or less. The reasons for a high coupling coefficient can be as simple as the array being too close to a conductive sample, but usually it is caused by high geometric coupling, insufficient preamplifier decoupling, poor cable routing, or a missing cable balun. The methods described in sections 1.4.4 and 1.4.5 can be used to reduce these sources.

2.4.6 Safety considerations for human imaging

Coils should always be designed with safety in mind, particularly if they are to be used on volunteers. Considerations focusing on fire safety, capacitive coupling, and coil heating are discussed here.

The materials choice is very important for fire safety. A small flame can quickly spread if the wrong materials are used. Ideally, materials that have a UL-94 rating of V0 are ideal because they will self extinguish once the heat source has been removed. Materials such as copper, fiberglass reinforced board (FR-4), polyethyleneimine (PEI), PEEK, and PTFE have a UL-94 rating of V0 and therefore are appropriate choices. Plastics like acrylonitrile butadiene styrene (ABS), Nylon, or polyethylene (PE) are not good choices for array construction because of their tendency to melt and stick to objects as they burn [26]. However, not all materials suitable for coil fabrication are fire-rated, in which case the coils should be enclosed or laminated in a UL-94 V0 rated material to minimize the risk of fire. Commercial receive-only coils have been built with materials meeting only UL-94 V2 requirements and are not as robust to fire, but those arrays have been submitted to more detailed tests when compared to the typical research arrays. To illustrate the importance of fire safety on the material choice, Fig 2.13 shows the site of an arcing event caused by a broken blocking circuit. In this image, black soot can be observed on the UL-94 V0 rated materials (PTFE) that easily contained the hot arc caused by a conductor failure. These materials prevented the arc from spreading and prevented any contact with the sample.

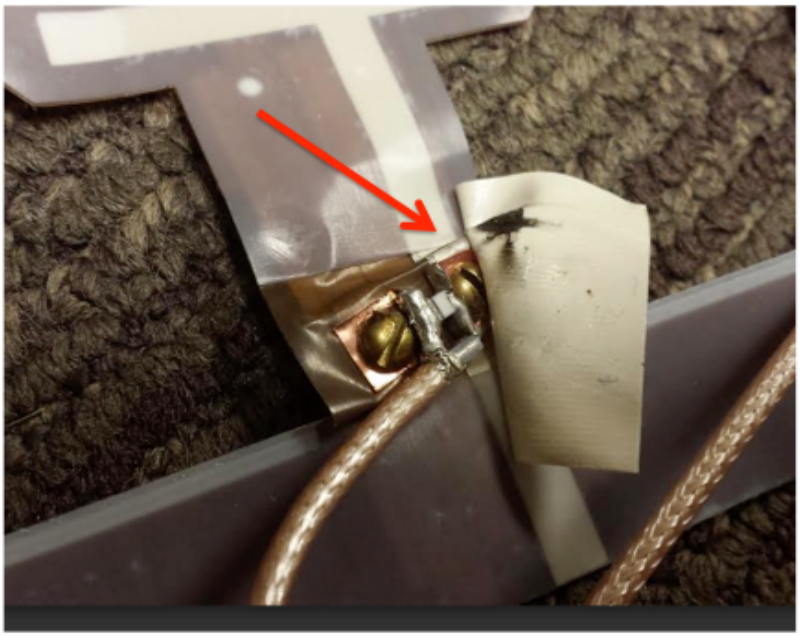

Figure 2.13: Photograph of an arcing failure site between the flexible coil (brown and silver) and the inflexible coil cabling (copper and gold). Red arrow highlights the location of the failure and the containment. Black soot can be observed where the arc was contained by the PTFE laminate, preventing it from spreading to other portions of the coil.

Coils placed too close to the skin can also adversely affect safety, particularly at high field strengths such as 3T. At these frequencies, capacitive coupling from the coil to the skin may be significant if the coil is close. If a large current were present on the coil, it will be coupled to the skin and cause a burn [27]. The International Electrotechnical Commission (IEC) suggests in their 60601-1 standards that a distance of 2-4 mm is sufficient to provide patient protection and is a sufficient starting point for a safe offset.

MRI scans require a patient to remain still for 30-40 minutes. During this time, portions of the coil can be in direct contact with their skin. It is important that these components do not heat to high levels throughout the scan, however the threshold for damage is low because of the long duration that patients remain in contact with the hot components. The maximum temperature allowed for any component in contact with the patient for longer than 10 minutes is 43°C, according to IEC 60601-1.

A long scan can be used with a high amount of RF energy delivered as a worst-case scenario to characterize how much the coil components heat up during the scan. This is usually accomplished by prescribing the maximum flip angle and the shortest repetition and echo time the scanner will allow. A sequence like this will impart the most RF energy into the patient while maintaining the least amount of time for heat to diffuse away. Any sequence type can work so long as the specific absorption rate (SAR) limit is at maximum. To perform this test, the coil should be positioned in the scanner without a phantom to prevent heat from conducting away from the coil (a phantom should still be used for locating the coils and to set pre-scan the settings). An infrared image of the coil before and after this sequence should be taken to verify where and how much the coil

heated up – example heat maps are shown in Fig 2.14. The red spots shown in the right of Fig. 2.14 indicate where portions of the coil heated up during the scan. If required, this test can be followed up by a longer scan and with thermal probes located on the previously characterized hotspots, running the scan for 40 minutes or more until the hotspots have reached a steady-state.

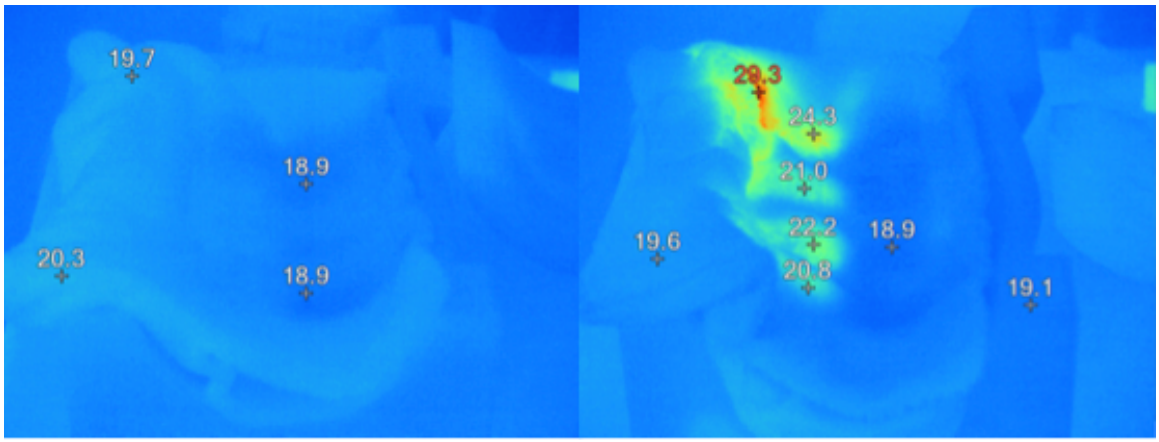

Figure 2.14: Thermal images of a coil array before and after a thermal stress test scan. If a more detailed thermal analysis needs to be done, thermal probes can be placed on the hot spots recorded in the right image during a longer scan.

If the thermal characterization indicates that the coil is getting too hot, the easiest method to prevent patient contact with warmer portions of the coil, such as the blocking circuitry, traps, or baluns, is simply to create a 5 mm air gap between the patient and the coil. If a cable or trap is getting too hot, adding more traps to a cable or coil can reduce the peak temperature of any hotspot. The temperature of the cable traps can also be reduced by positioning them away from the walls of the scanner, where the magnitude of the RF pulses are the highest, but this usually is not a clinically viable solution [28].

2.5 References

[1] C. Gabriel, S. Gabriel, and E. Corthout, "The dielectric properties of biological tissues: I. Literature survey," *Phys Med Biol,* vol. 41, pp. 2231-49, Nov 1996.

[2] S. Gabriel, R. W. Lau, and C. Gabriel, "The dielectric properties of biological tissues: III. Parametric models for the dielectric spectrum of tissues," *Phys Med Biol,* vol. 41, pp. 2271-93, Nov 1996.

[3] S. Gabriel, R. W. Lau, and C. Gabriel, "The dielectric properties of biological tissues: II. Measurements in the frequency range 10 Hz to 20 GHz," *Phys Med Biol,* vol. 41, pp. 2251-69, Nov 1996.

[4] H. Kato, M. Kuroda, K. Yoshimura, A. Yoshida, K. Hanamoto, S. Kawasaki*, et al.*, "Composition of MRI phantom equivalent to human tissues," *Med Phys,* vol. 32, pp. 3199-208, Oct 2005.

[5] I. L. Pykett, B. R. Rosen, F. S. Buonanno, and T. J. Brady, "Measurement of spin-lattice relaxation times in nuclear magnetic resonance imaging," *Phys Med Biol,* vol. 28, pp. 723-9, Jun 1983.

[6] K. A. Kraft, P. P. Fatouros, G. D. Clarke, and P. R. Kishore, "An MRI phantom material for quantitative relaxometry," *Magn Reson Med,* vol. 5, pp. 555-62, Dec 1987.

[7] M. D. Mitchell, H. L. Kundel, L. Axel, and P. M. Joseph, "Agarose as a tissue equivalent phantom material for NMR imaging," *Magn Reson Imaging,* vol. 4, pp. 263-6, 1986.

[8] L. O. Morgan and A. W. Nolle, "Proton Spin Relaxation in Aqueous Solutions of Paramagnetic Ions. II. Cr+++, Mn++, Ni++, Cu++, and Gd+++," *The Journal of Chemical Physics,* vol. 31, pp. 365-368, 1959.

[9] D. M. Pozar, *Microwave engineering*, 3rd ed. Hoboken, NJ: J. Wiley, 2005.

[10] A. M. Niknejad, *Electromagnetics for high-speed analog and digital communication circuits*. Cambridge ; New York: Cambridge University Press, 2007.

[11] J. P. Dunsmore, *Handbook of microwave component measurements : with advanced VNA techniques*. Chichester, West Sussex, United Kingdom: Wiley, 2012.

[12] J. l. Mispelter, M. Lupu, and A. Briguet, *NMR probeheads for biophysical and biomedical experiments : Theoretical principles & practical guidelines*. London: Imperial College Press, Distributed by World Scientific, 2006.

[13] B. Keil, "Construction of Receive Arrays," in *ISMRM*, Salt Lake City, Utah, 2013.

[14] L. D. Landau and E. M. Lifshitz, *The classical theory of fields*, 3d rev. English ed. Oxford, New York,: Pergamon Press, 1971.

[15] A. Kocharian, P. J. Rossman, T. C. Hulshizer, J. P. Felmlee, and S. J. Riederer, "Determination of appropriate RF blocking impedance for MRI surface coils and arrays," *MAGMA,* vol. 10, pp. 80-3, Jun 2000.

[16] V. T. P. C. F. Robb, "Minimal Acceptable Blocking Impedance for RF receive coils " in *ISMRM*, 2010.

[17] D. Nishimura, *Principles of Magnetic Resonance Imaging*: Stanford University, 2010.

[18] O. Dietrich, J. G. Raya, S. B. Reeder, M. F. Reiser, and S. O. Schoenberg, "Measurement of signal-to-noise ratios in MR images: influence of multichannel coils, parallel imaging, and reconstruction filters," *J Magn Reson Imaging,* vol. 26, pp. 375-85, Aug 2007.

[19] M. Uecker, P. Lai, M. J. Murphy, P. Virtue, M. Elad, J. M. Pauly*, et al.*, "ESPIRiT--an eigenvalue approach to autocalibrating parallel MRI: where SENSE meets GRAPPA," *Magn Reson Med,* vol. 71, pp. 990-1001, Mar 2014.

[20] P. B. Roemer, W. A. Edelstein, C. E. Hayes, S. P. Souza, and O. M. Mueller, "The NMR phased array," *Magn Reson Med,* vol. 16, pp. 192-225, 1990.

[21] K. P. Pruessmann, M. Weiger, M. B. Scheidegger, and P. Boesiger, "SENSE: sensitivity encoding for fast MRI," *Magn Reson Med,* vol. 42, pp. 952-62, 1999.

[22] J. A. Nordmeyer-Massner, N. De Zanche, and K. P. Pruessmann, "Mechanically adjustable coil array for wrist MRI," *Magn Reson Med,* vol. 61, pp. 429-38, Feb 2009.
[23] K. P. Pruessmann, M. Weiger, P. Bornert, and P. Boesiger, "Advances in sensitivity encoding with arbitrary k-space trajectories," *Magn Reson Med,* vol. 46, pp. 638-51, Oct 2001.
[24] American Radio Relay League., "The ARRL handbook for radio communications," in *Radio amateur's library publication no 6*, ed. Newington, CT: ARRL, 2002, p. v.
[25] G. R. Duensing, H. R. Brooker, and J. R. Fitzsimmons, "Maximizing signal-to-noise ratio in the presence of coil coupling," *J Magn Reson B,* vol. 111, pp. 230-5, Jun 1996.
[26] J. G. Quintiere, *Fundamentals of fire phenomena*. Chichester: John Wiley, 2006.
[27] B. Keil and L. L. Wald, "Massively parallel MRI detector arrays," *J Magn Reson,* vol. 229, pp. 75-89, Apr 2013.
[28] D. M. Peterson, B. L. Beck, G. R. Duensing, and J. R. Fitzsimmons, "Common mode signal rejection methods for MRI: Reduction of cable shield currents for high static magnetic field systems," *Concepts in Magnetic Resonance Part B: Magnetic Resonance Engineering,* vol. 19B, pp. 1-8, 2003.

Chapter 3

3. Fabrication of Printed Coils

3.1 Introduction

Surface receive coil and arrays are built to acquire images with the highest possible SNR for a specific area of the body [1]. The current manufacturing process for commercial coils relies on the use of high quality electronic components such as porcelain capacitors, thick copper traces, and low-loss substrates. These electrical components are then packaged inside medical grade, fire resistant materials that contribute to the size and weight of a given array. Fig. 3.1 shows examples of two current typical coil arrays used for head and chest imaging on an adult [2]. Note that the array on the patient's chest has the ability to flex right to left some degree, but is still very inflexible down the patient due to the materials used for construction.

Figure 3.1: Two separate conventional MRI receive arrays on the chest and head of a patient.

In order for a surface coil to deliver high SNR, it should be placed in close proximity to the tissue to be imaged [3, 4]. To illustrate the benefits of a properly fitting coil, Fig. 3.2 compares a cervical spine image obtained by a printed flexible coil that fits perfectly against the neck to an image obtained using a conventional surface coil on the patient-table 8 cm away from the base of the neck. The image from the poorly positioned coil shown in Fig 3.2 A has much lower SNR than the image from the close fitting coil in Fig 3.2 B, highlighting the importance of coil placement during a scan [2].

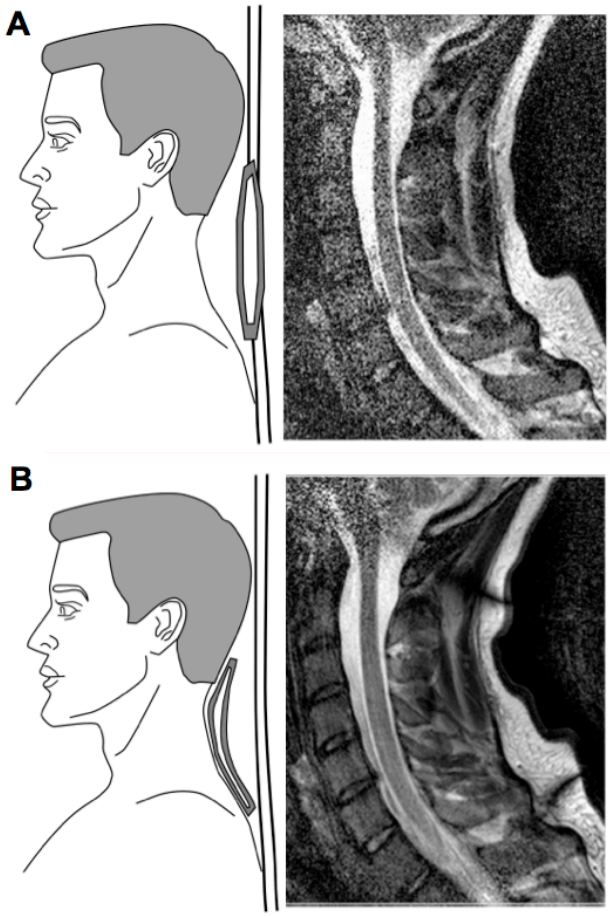

Figure 3.2: Cervical spine images of volunteer showing **A** low-SNR when using a coil placed 8 cm away from the spine and **B** high SNR when placed against the skin. Images are acquired with a turbo spin echo (TSE) sequence on a 3T Siemens scanner with an echo time (TE) of 112 ms, repetition time (TR) of 3500 ms, and flip angle (FA) 90°. The field of view is 200 x 200 mm^2 with resolution of 436 lines in phase encodes and readout directions with slice thickness of 4 mm. To compensate for imaging intensity variation due to the coil sensitivity, the image is normalized with respect to a uniform body coil image [2].

When a receive coil is placed close to the body, its sensitivity to tissue signal is dramatically increased. However while in close contact, the coil is strongly affected by the conductivity of human tissue, imposing a limit on image quality that is not dependent on coil materials [5-8]. This provides an opportunity to use the highly flexible solution processed materials found in printed electronics, which have previously been dismissed due to higher loss. These materials can still perform adequately for receive coils without compromising image SNR while providing significant improvements in flexibility, lightness, and mass manufacturing ability. In the past, several works have focused on adding flexibility and conformity to MRI receive arrays by using a conductor sewn into fabric [9], a mercury based conductor [10, 11], and semi-flexible copper tape [12] – discussed previously in chapter 1.

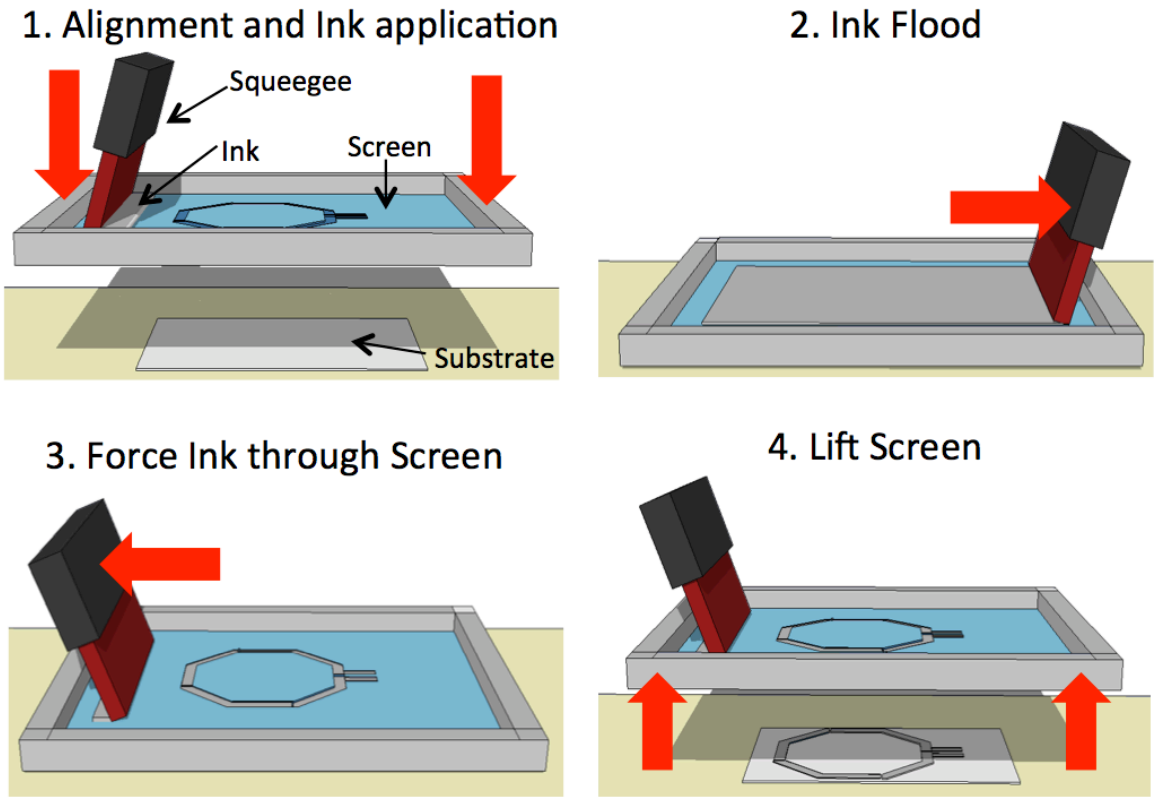

Figure 3.3: Schematic representation of fabrication process steps used to fabricated flexible printed coils. The screen is patterned with emulsion (blue) and shows the coil design. Ink (grey) is transferred to the substrate (white) during the screen-printing process.

In this thesis, coils are screen-printed layer-by-layer onto lightweight flexible substrates [2]. Figure 3.3 illustrates the screen printing process showing how a red flexible bar pushes the white conductive ink through holes in the screen onto the substrate to form the coil pattern [2, 13]. The advantage that printing has over previous techniques is the scalability and adaptability it possess, qualities necessary in order to become a commonly used technology. Printing can also be tailored by using different inks, substrates, and techniques enabling custom pattern design [14]. Screen-printing is ideal for coil fabrication because of the thick, low resistance conductive traces required over a large area (i.e., body size) at a high throughput, which are not easily produced with other methods of printing.

Advances in electronic materials processed from solution have already resulted in the demonstration of flexible electronic devices such as light emitting diodes, thin film transistors, and photovoltaic devices [13-17]. While flexible electronics applications targeting the consumer electronics market are very promising, flexible medical devices that are in contact with the human body add considerable functionality [18-20]. In our case, a well fitting array is critical in obtaining high SNR that can then be used to shorten scan time and reduce complications. For example, if the same chest array pictured in Fig. 3.1 were used on a smaller person or a child, the array would fit poorly creating large gaps between the coil elements and the body, squandering much of the SNR gained from

high quality components [21]. This problem is aggravated in small children, who do not fit the array well and require general anesthesia to restrict motion during the exam [22, 23].

To take advantage of the flexibility that printing offers and address the current problems in pediatric imaging, printed receive arrays could be integrated into lightweight fabric, like the baby blanket based coil shown in Fig. 3.4. The proof-of-concept array shown in Fig. 3.4 tightly wraps around the patient maintaining SNR, which could enable pediatric patients to receive shorter MRI exams with increased comfort and image quality.

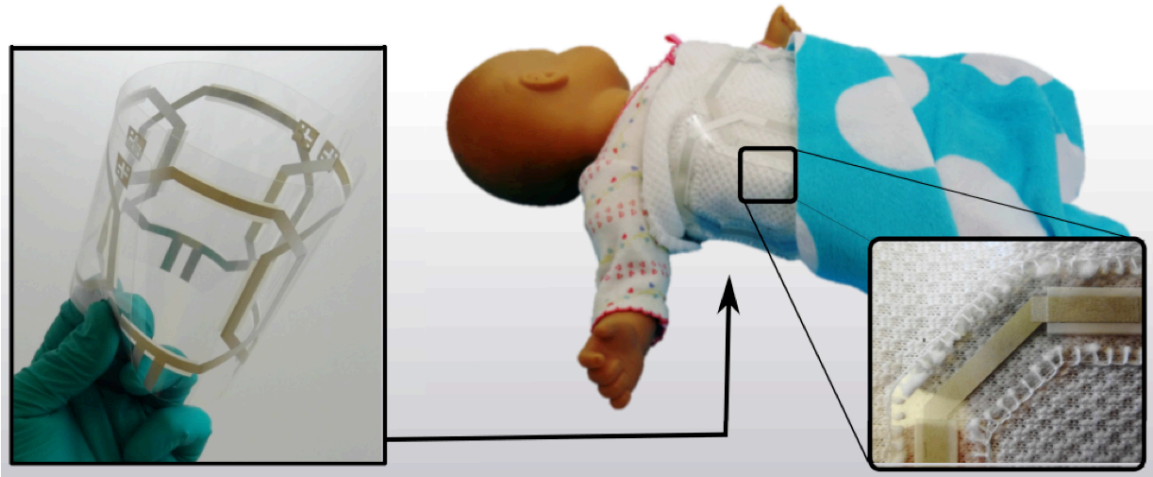

Figure 3.4. Photograph of a printed flexible four-channel coil array fabricated on plastic film and integrated into an infant blanket. The inset shows how a printed coil is stitched into the fabric.

This chapter covers the construction and characterization of the first fully printed flexible coils for 1.5 T and 3 T clinical scanners. A detailed analysis of the material properties and the performance of printed components are characterized. The imaging performance of coils is analyzed using scans of phantoms and volunteers. From our results we identify the most promising avenues for coil optimization (covered further in Chapter 4).

3.2 Fabrication of Printed Coils for 1.5 and 3T

Receive coils are tuned loops of wire with in-series capacitors resonant at the Larmor frequency of the scanner. For clinical imaging, this frequency is approximately 64 MHz at 1.5 T or 127 MHz at 3.0 T [1, 24]. The resonant frequency of a conductive loop is determined by its inductance and capacitance, which both depend on the geometry and materials used. The size of the loop is typically predetermined, fixing the inductance. Therefore tuning capacitors (C_t) are added to the loop to tune the desired resonant frequency. To minimize reflection losses at the interface between coil and cable, a matching capacitor (C_m) is added to match the input impedance to 50 Ω [1, 24]. Figure 3.5 A shows a typical coil circuit that meets these requirements.

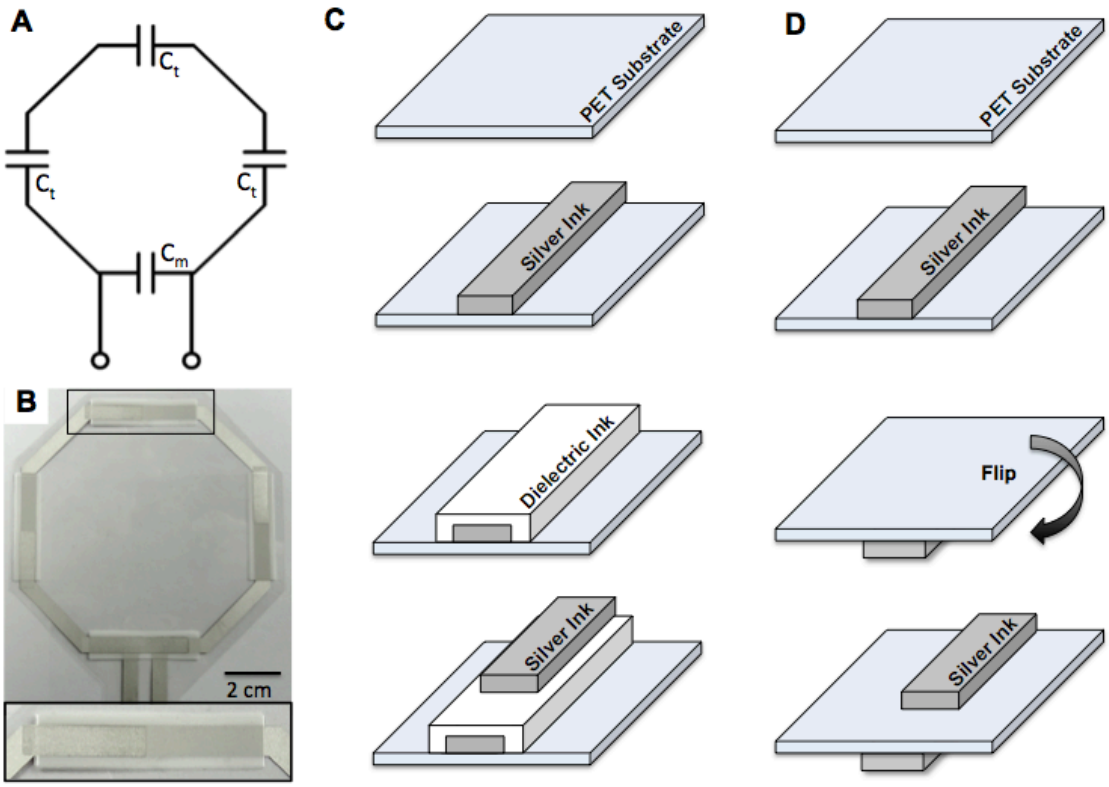

Figure 3.5: **A.** Schematic of a printed coil showing tuning, C_t, and matching, C_m, capacitors. **B.** Photograph of a printed coil. Inset highlights top-down view of printed capacitor. **C.** Coil printing process flow with printed dielectric D. Coil printing process flow using the substrate as a dielectric.

To create a printed coil, the circuit in Fig. 3.5 A is fabricated layer-by-layer using a screen printer to deposit the conductive and insulating layers. Figure 3.5 B shows a picture of a completed printed coil with matching and tuning capacitors created by printing dielectric and conductive material.

In this chapter we examine the two topologies used to create receive coils for clinical use. The first all printed approach, illustrated in Fig. 3.5 C, consists of 3 layers of printed material with two conductive printed silver traces sandwiching a printed dielectric on top of a flexible substrate [2]. The second method is illustrated in Fig. 3.5 D and only uses 2 printed silver layers on either side of a flexible substrate [25]. Sections of the coil where the printed conductors overlap form the capacitors used to tune the coil.

The following sections describe the design parameters taken into consideration when fabricating a printed coil. This includes a discussion on coil size as well as the specific materials used to make the coils.

3.2.1 Calculating Coil Size

When the sample conductivity and coil conductivity are known, it is possible to determine at which coil diameter the losses due to the sample are much larger than losses from the coil. If the losses due to the sample are much greater than the losses from the coil the system is referred to as sample-noise dominated (also known as body-noise

dominated). In a sample noise dominated system any improvements to the coil material would only have a marginal impact in the overall SNR performance. Using equations 1.6 and 1.7 from Darrasse et al. previously descried in chapter 1 (reproduced here) it is possible to model at what coil radii (a) would the majority of losses come from the sample [6].

$$R_c = \sqrt{0.5\rho_c\mu_0\omega}\left(\xi\frac{a}{r}\right) \qquad (1.6)$$

$$R_S \approx \frac{2}{3\pi}\sigma\mu_0^2\omega^2 a^3 \tan^{-1}\left(\frac{\pi a}{8d}\right) \qquad (1.7)$$

To perform this estimate, we assumed a sample temperature (T_s) of 37 °C, coil temperature (T_c) of 20 °C, sample conductivity (σ) of 0.66 S/m, printed trace resistivity (ρ_c) of 1.25 μΩ-m, copper trace resistivity of 16.7 nΩ-m, trace thickness of 12 μm, and a circular coil with one turn directly on the surface of the sample. The geometric proximity effect factor ($\xi a/r$) describes the effects of current crowding, in our analysis we used a value of 45 [6]. Analysis is performed over frequencies (ω) between 10-400 MHz with a trace width (r) radius of 5 mm to produce the trends seen in Fig. 3.6.

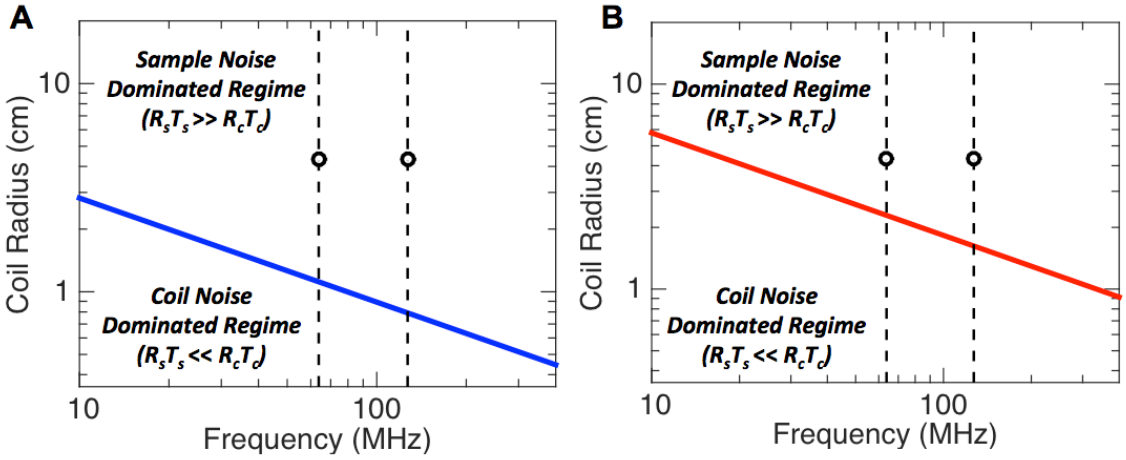

Figure 3.6: Frequency dependence of sample noise and coil noise dominated regimes. For **A** copper based coil and **B** printed conductor coil. Black circles highlight coil used in example at 1.5 and 3 T.

The trend-lines shown in Fig. 3.6 highlights where coil and sample noise are equal. Any coil size greater than this critical value (i.e, above the line) is limited primarily by the losses in the body, allowing flexibility in material choice. While the distance between the test coil radius of 2.75 cm and the equilibrium line is greater if a copper conductor is used, the coils made with a printed conductor are still body noise dominant. As printed materials improve in conductivity, the effects of coil loss become smaller, allowing coils of smaller radii to be built while maintaining sample-noise dominance. Different coil sizes, particularly smaller coils, can enable denser arrays to be built, further decreasing

scan time [26, 27]**.** Based on this analysis we chose our coils to have a of 8.7 cm in diameter and conductor width of 0.5 cm to ensure body-noise dominance and maintain useable coil penetration [21].

3.2.2 Printed Dielectric

To make a coil using an all printed design, previously illustrated in Figure 3.5 C, we deposited solution-processed materials on one side of a flexible substrate. The first metal layer of the conductive coil is screen printed, using an ASYS APM101 screen printer, onto a 75 μm thick polyethylene terephthalate (PET) film using a silver micro-flake ink, with flake size of 7 μm, purchased from Creative Materials (118-19A/B). The metal layer is annealed at 125 °C for 15 minutes prior to the deposition of the dielectric material. Two types of dielectric inks are used when printing the tuning and matching capacitors, a UV-curable resin (Creative Materials 116-20) and a barium titinate ($BaTiO_3$) ink (Conductive Compounds BT-101). A 60 μm thick layer of UV-curable resin is used for coils tuned for a 3 T scanner and cured with a mercury arc lamp, with 24 W/cm^2 power flux for 3 seconds. Coils designed to work in 1.5 T scanners required higher dielectric constant. For these, 30 μm thick layers of $BaTiO_3$ ink are used as the dielectric layer of the capacitors. After deposition, the $BaTiO_3$ ink is annealed on a heating plate at 125 °C for 15 minutes. The top electrode of the capacitors is formed with a 30 μm thick layer of silver micro-flake ink. The finished coil is further annealed at 125 °C for 15 minutes on a heating plate.

3.2.3 Substrate Dielectric

The materials for printed devices are constantly evolving and better-suited inks are becoming available for a wider variety of substrates. One of the benefits of our printing process is that it lends itself very well to rapid prototyping with these new materials without the need for completely redesigning the printing process. For example, it is possible to use the substrate as the dielectric for the printed capacitors without a significant change in coil design. To demonstrate this case, we created a coil with an improved conductive silver ink (Silver micro-flake, Dupont 5064H) printed on both sides of a low-loss substrate, 75 μm thick polyether ether ketone (PEEK), forming capacitors where the layers overlap as shown in Fig. 3.5 D. These layers are annealed at 140 °C for 15 minutes. Capacitors with the PEEK substrate as the dielectric have significantly lower loss than the printed dielectric ones, and can greatly improve the SNR of printed coils. This design is the result of further optimizations detailed in Chapter 4.

3.3 Printed Capacitor Characterization

The printed capacitors set the correct resonant frequency and the input impedance of our printed coils. Unlike the discrete capacitors used in current coil construction, the printed coils will have capacitors comprised of printed conductors sandwiching a flexible dielectric material. Since the dielectric is solution processed, the composition can be

changed in order to meet process goals. To investigate the properties of printed capacitors, several are made with different concentrations of high ($BaTiO_3$ ink) and low (UV-curable resin) dielectric constant material with an area of 35 mm^2 (approximately the size of the final design). For each measurement, capacitors are mounted with plastic clamps on a copper printed circuit board (PCB) test fixture over a 30x30 mm^2 opening in the board. The experimental fixture is calibrated using identically shaped open, short, and 50 Ω calibration boards.

Figure 3.7 A shows the dielectric constant linearly increasing as the composition of the dielectric ink is changed. As can be seen, the dielectric constant increases linearly as more $BaTiO_3$ ink is added. The maximum dielectric constant measured is 15, which is much lower than pure $BaTiO_3$. This is due to the fact that our ink is a mixture of $BaTiO_3$ and other binders, making the dielectric constant significantly lower. The self-resonant frequency of these capacitors is also characterized to ensure that they did not operate near it. Figure 3.7 B shows the self-resonant frequency of the capacitors as the area is increased. In this figure, the lowest self-resonant frequency is 247 MHz, sufficiently far enough away from 127.72 MHz, which is the highest frequency of operation at 3T.

The printed coils are tuned by changing the value of the printed capacitors. This is accomplished by changing the printed capacitor's area of the top electrode, the thickness of the dielectric, and the composition of the dielectric layer. To characterize the range of capacitance that could be achieved, printed test capacitors that are 5 mm wide with an overlap ranging from 1 to 30 mm in length are characterized using the same procedure as previously described.

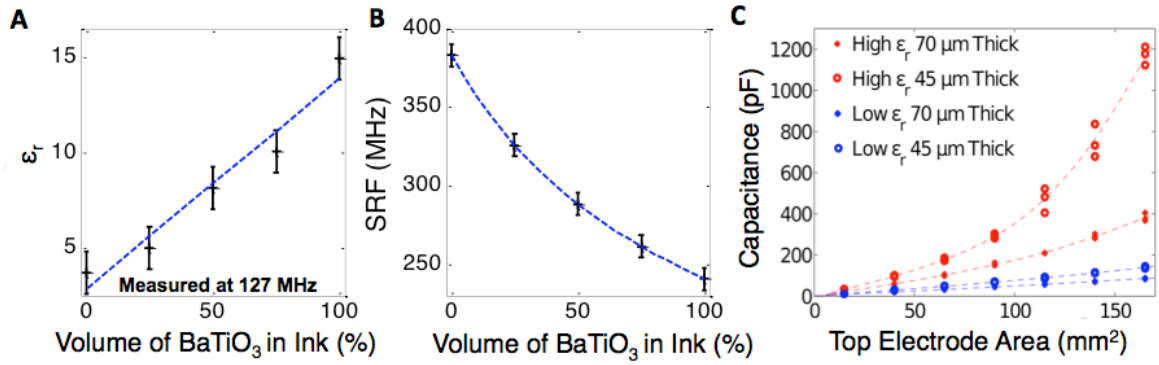

Figure 3.7: **A** Relative dielectric constant, measured at 127 MHz, as the volume of barium titanate in the ink is increased. High dielectric constant is achieved with barium titanate ink, while low dielectric constant is achieved with ultraviolet-curable ink. Error bars show standard deviation. **B.** Self-resonant frequencies of printed capacitors vs. dielectric ink composition **C.** Dependence of capacitance with top electrode area, dielectric thickness and ink composition.

The dependence of capacitance with printed dielectric thickness (45 µm and 70 µm), composition of dielectric ink (ε_r = 15 or ε_r = 4), and top electrode area is summarized in Fig. 3.7 C. Figure 3.7 C shows that this process had an experimental window that allowed us to achieve capacitances ranging from 2 pF to 1200 pF, matching the ranges needed for tuning coils to different frequencies with similar coil geometry. The non-linear effects seen for higher value capacitors (i.e, the upward curve seen in the high ε_r materials as the

top electrode area is increased) are due to a self-resonant frequency that is near 127.72 MHz. However, these large values are not used in our coils for 1.5 and 3 T and do not significantly impact coil design.

With the capacitor properties shown in Fig. 3.7 it is possible to design capacitors for printed coils that are targeted for a particular value while avoiding operating near the self-resonant frequency of the capacitor.

3.4 Printed Coil Characterization

The viability of using our printed flexible coils in a clinical setting is evaluated by characterizing quality factor and image SNR using a $NiCl_2$-doped saltwater (0.68 S/m at 3T) phantom as a model for human tissue. In our study, we fabricated five different types of coils: an all-printed flexible coil, a copper coil in which printed capacitors replaced the conventional capacitors, a coil with printed silver conductors integrated with low-loss porcelain capacitors, a coil with improved printed silver conductors utilizing the low-loss PEEK substrate as the dielectric for capacitors and a semi-flexible control coil composed of copper conductors and low-loss porcelain capacitors. Specifically, control coils are fabricated using a 70 μm thick etched copper on 75 μm thick Pyralux AP low-loss substrate. Advanced Technical Ceramics (ATC) 100B low-loss porcelain-based capacitors are soldered onto the copper traces to form tuned coils.

All coils had the same geometry, and the control coil is not placed in any mechanical enclosure, allowing us to flex and measure SNR with all five types of coils. To tune printed coils, the capacitance is modulated using different dielectric inks in addition to changing the size of conductive electrodes. It is found that the most effective strategy for coarse tuning the capacitance is to control the composition of the dielectric ink first for coarse tuning. Then, the area of top electrode could be changed to provide the fine-tuning needed to reach the specific frequencies. Control coils are tuned by soldering different values of ATC 100B capacitors to the copper traces. Coils are tuned so that they resonated at the Larmor frequency and displayed 50 Ω impedance [24].

3.4.1 Quality Factor Measurements

In order to characterize how printed materials compare to non-printed materials, Q_{Loaded} and $Q_{Unloaded}$ are measured. Coils are measured by placing them between two broadband magnetic field probes connected to an Agilent E5061B ENA network analyzer. The probes are 30 cm apart and facing each other to minimize the $|S_21|$ noise floor to approximately -90 dB [28]. During all measurements, it is ensured that the coil test apparatus is at least 50 cm away from any conductive material to prevent artificial loading of the coil. To measure Q_{Loaded}, coils are taped to a cubic phantom 7 L in volume, filled with solution of 3.356 g/L nickel chloride hexa-hydrate (NiCl2*6H20) and 2.4 g/L of sodium chloride (NaCl) for conductivity of 0.68 S/m at 123-127 MHz. $Q_{Unloaded}$ is measured using the magnitude of the S_{21} response with 1601 points averaged 16 times, centered at the Larmor frequency with the network analyzer set to a frequency span of 25 MHz, while Q_{Loaded} is measured with a span of 100 MHz.

The results of characterizing the 5 types of coils are shown in Tables 3.1 for 3 T while a comparison of a printed coil to a control coil is shown in Table 3.2 for 1.5 T. From the characterization at both 1.5 and 3 T these values indicate that the $Q_{Unloaded}$ of the printed materials is lower than non-printed materials. However, the difference in Q_{Loaded} is less pronounced, leading to the small difference in predicted SNR. Predicted SNR is calculated by taking the ratio of $\sqrt{Q}_{loaded}$ for each coil type compared to the control. It is important to note that there is a larger difference between Q_{Loaded} and predicted SNR at 1.5 T between printed and control coils. This is due to the smaller effect body noise dominance has at lower frequencies.

In the following section the SNR predicted by Q values is compared to the SNR seen in images from scanners.

Table 3.1. Loaded, unloaded, predicted, and measured SNR for coils created for 3 T system. Several regions within the phantom are used to calculate SNR.

Coil Type	$Q_{unloaded}$	Q_{loaded}	Predicted SNR vs. Control	Measured SNR vs. Control
Control (non-printed)	395	11.4	100 %	100 %
Printed Conductor	76	9.8	93 %	96±3 %
Substrate Capacitor	73	9.5	91 %	93±3%
Printed Capacitor	22.3	7.6	82 %	86±3 %
All Printed	17.9	6.7	77 %	79±3 %

Table 3.2. Loaded, unloaded, and predicted SNR for coils created for 1.5 T system. Several regions within the phantom are used to calculate SNR.

Coil Type	$Q_{unloaded}$	Q_{loaded}	Predicted SNR vs. Control	Measured SNR vs. Control
Control (non-printed)	367	28.9	100 %	100%
All Printed	23	13.2	67 %	69±3 %

3.4.2 SNR at 1.5T and 3T

Measurements on 3T scanner are used to verify predictions from bench top testing. SNR measurements are performed on the scanner by placing the coils on the same 7 L phantom used to measure Q_{Loaded}. To interface with the scanner, all coils are clamped into a test fixture board that had a PIN diode to deactivate the coil during the transmit phase of each scan as previously described in section 2.4.1. This fixture is connected via half-wavelength long coaxial cables to an interface box that houses preamplifiers connected to

the scanner. The half-wavelength coaxial cable contained a cable-trap circuit tuned to the Larmor frequency. Image reconstruction methods are unchanged from those used in conventional coils.

The scans used to measure SNR are 2D Gradient Echo (GRE) sequences on 3 T (Siemens TIM Trio, Erlangen: Germany) and 1.5 T (General Electric Signa, Waukesha: United States) scanners with an encoding time (TE) of 10 ms, readout time (TR) of 438 ms, and flip angle (FA) of 25°. Field of view is 200x200 mm^2 with resolution of 256 phase encodes and readouts. Slice thickness is 5 mm. The same prescan settings are used for all experiments, reducing variations due to differing magnet shimming, analog gain, and digital gain. Images of phantoms have SNR measured by dividing signal (i.e., pixel in phantom) by an estimate of the noise standard deviation. The noise is estimated from an image area with no signal containing at least 2800 points at least 5 pixels from the edge of the image, to avoid effects from the scanner's low-pass filter. The noise only area did not contain any signal artifacts from other regions in the image. Measured SNR is reported for values seen across the entire phantom and away from the surface of the phantom. A diagram illustrating the experimental imaging setup and relative SNR in cross-section through the phantom are shown in Fig. 3.8 A.

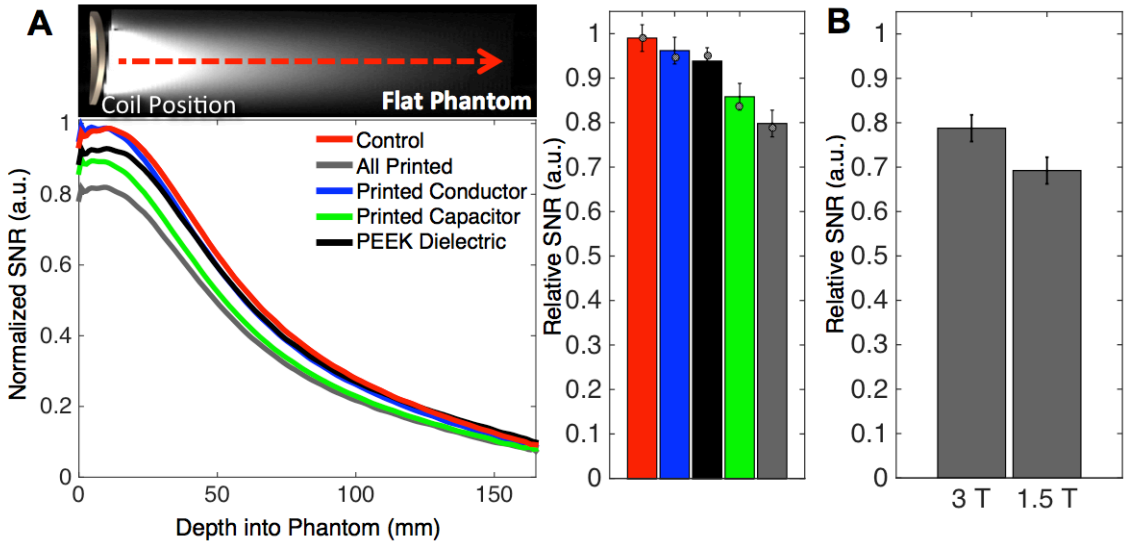

Figure 3.8: **A.** Normalized SNR versus depth into the phantom for coils fabricated with different permutations of printed components at 3T, with schematic showing coil position 3 mm away from conductive fluid. Bar graph summarizes trends shown in relative SNR for each coil type. Dot on bar graph shows predicted SNR, extracted from bench top quality factor measurements. **B.** Relative measured (bars) and bench top-predicted (dots) image SNR of printed coils at 1.5T and 3T.

Figure 3.8 A shows that coils close to the phantom at 3T present 79±3%, 86±3%, 93±3%, and 96±3% relative SNR corresponding to fully-printed, printed capacitors, PEEK capacitors, and printed conductor respectively. SNR values are normalized with respect to the control coil and the SNR predicted from bench tests is shown as a dot in the bar graph of Fig. 3.8 A. The fully printed coils show slightly higher relative SNR when

used at 3T compared to 1.5T system, as shown in Fig. 3.8 B. This difference is attributed to the larger role coil loss plays at lower frequencies [6]. All predicted SNR values are within the standard deviation of the SNR measured in images.

The analysis of the results shown in Fig. 3.8 indicates that for fully printed coils, the printed dielectric represents a large source of loss for coil performance. Image SNR could be significantly increased from the dielectric material improvement. For example, if a near perfect dielectric is used (as is almost the case for coils made with ATC capacitors) the printed design could achieve as high as 96% image SNR compared to the control at the same distance. This finding is examined further in chapter 4.

3.4.3 Offset Imaging

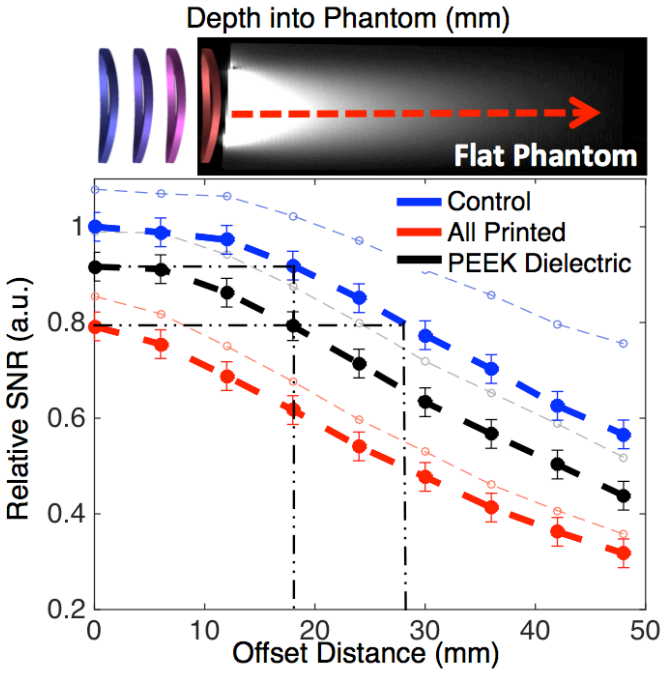

Figure 3.9: Relative SNR for control and printed coils versus increasing coil offsets from the top surface of the phantom. Black dashed-dotted line highlights the position offset where the control coil shows equal SNR to the printed coils when the printed one has no offset from the top surface of the phantom. Light dashed lines represent the calculated best-case performance when preamplifiers are added to the coil to reduce transmission mismatched line losses. Error bars show standard deviation.

To evaluate where the SNR gained from a well fitting printed coil would overcome the SNR lost by a poorly fitting high quality coil, the printed and control coils are placed at increasing offsets from the phantom and the SNR is measured in images. To maintain a uniform offset for the experiments, different thicknesses of polycarbonate sheet are inserted between the phantom and each coil.

The summary of SNR tests in Fig. 3.9 shows that the SNR decreases for all the coils as they are moved away from the phantom. However, when the printed coils are kept in close contact with the phantom, the SNR of the control coil is surpassed by the printed

coils at phantom offsets of 18 mm for the PEEK dielectric and 28 mm using printed dielectric.

In our experiments, all coils show additional losses from the cables used to connect to them to the preamplifiers. This loss is made worse if there is an impedance mismatch between the coil and the cable since we do not place preamplifiers directly on the coils. In the offset experiments, the impedance presented by the coils is affected by the coil loading as it moved away from the phantom. This mismatch adds transmission line losses that made the control coil exhibit lower SNR. Modern arrays often use coil-mounted preamplifiers that do not show these losses, so coils with mounted preamplifiers will exhibit slightly higher SNR than ours. To predict the scale of the effect, we measured the system voltage standing wave ratio (VSWR) as the coils are moved away from the conductive phantom. From the VSWR measurements and the matched transmission-line attenuation (36.09 dB/100m for the RG316 coaxial cable used) the coils reflection coefficient (ρ) and total mismatched line loss are calculated using equations 2.9 and 2.10 (reproduced here) [29]. When coils are close to the phantom (i.e., matched), the loss is only from the matched attenuation (a) of the cable (0.3 dB for our 84 cm length of RG316 coaxial cable). As coils moved farther away from the phantom, and their impedance shifted away from 50 Ω, the total mismatched line loss became more pronounced peaking at 0.97 dB for non-printed coils and 0.46 dB for printed ones. The calculated SNR considering the use of preamplifiers is shown as thin dotted lines in Fig. 3.9. As can be seen in Fig. 3.9, the dashed lines all have increased SNR. This increased SNR does not significantly affect the offset distance at which the SNR of the printed coils will be equal to the control coil, changing from 26 mm to 31 mm for fully printed coils and 18 mm to 21 mm for the PEEK substrate coils.

$$|\rho| = \frac{VSWR-1}{VSWR+1} \tag{2.9}$$

$$Total\ Mismatched\ Line\ Loss = 10\log\left[\frac{a^2-|\rho^2|}{a(1-|\rho^2|)}\right] \tag{2.10}$$

3.4.4 Curved Phantoms

If coils are very flexible, then it is likely that they will be used in ways that give them a high degree of curvature. If the coil is curved, then it will change the inductance, and potentially significantly impact the tuning of the coil. To investigate the degree that the coil is impacted, a highly curved phantom and a flat phantom with the same volume are imaged. Coils are measured first on a flat phantom then again wrapped around a phantom with a 22 mm radius of curvature. Both phantoms are 7 L in volume and contained a solution of 3 g/L of copper sulfate ($CuSO_4$) and 3g/L NaCl. Coils are not retuned between each scan.

Figure 3.10 compares the normalized SNR profiles around a curved and flat phantom of the same volume and composition. As can be seen, the sensitivity profile of the coils is not significantly changed between each phantom. The similar profiles are due to the phantom loading the coil. That is, when a coil is placed in close proximity to the sample,

the coils are heavily loaded, therefore changes in tuning due to the different geometry have a negligible effect on image SNR.

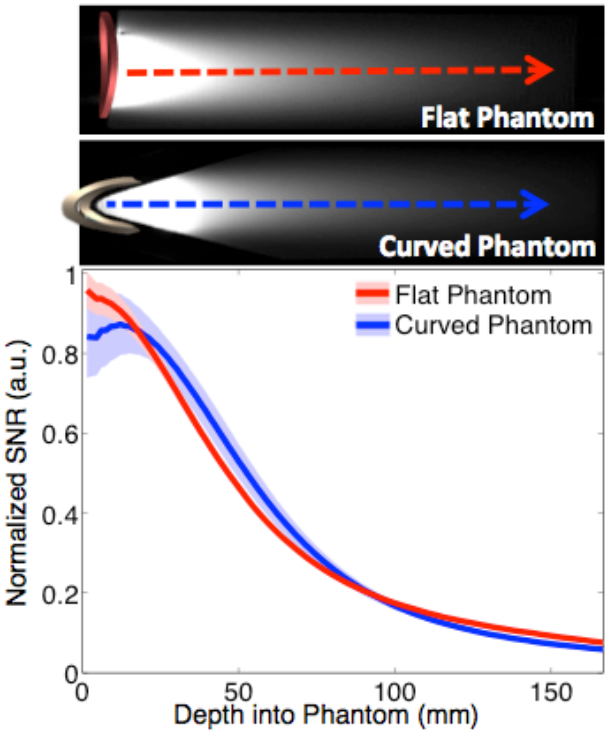

Figure 3.10: Average normalized SNR profile for printed coils flexed around the surface of a curved saltwater phantom (blue) and placed on a flat phantom (red) at 3 T. Wide colored bands indicate the standard deviation across several coils.

3.5 Volunteer Imaging with a Printed Array

The focus of this work is on the design, fabrication, and performance analysis of single surface coils. However, most clinical coils today are used in arrays. Therefore it is important to demonstrate that the printing process is scalable to printing coil arrays. A simple 4-channel receive array is developed to demonstrate that it is possible to produce arrays using printing. The array is designed for a 3 T scanner and is composed of 4 overlapped coil elements. Fig. 3.22 A shows the layout of the 4-channel array with neighboring coils printed on alternate sides of the substrate. The leads of each coil, along with a PIN diode, formed the blocking circuit that detunes the coils during the transmit portion of the scan. The PIN diode is attached using copper rivets pressed into the silver ink traces to form the electrical contact. The amount of coil overlap in the array is determined using two single coils and connecting each to one port of a network analyzer. Coils are overlapped until the magnitude of S_{21} between the coils is minimized. The array is connected to the low input impedance preamplifiers to take advantage of preamplifier decoupling, to reduce the amount of cross-channel coupling [4].

This array is used to image the cervical spine and knee areas of a volunteer since these are highly curved regions where other arrays struggle to conform. (This study operates under the University of California at Berkeley Internal Review Board studies

"High-Sensitivity Flexible MRI Coils via Printed Electronics (2013-07-5491)" and "Improved Magnetic Resonance Imaging Systems (2010-07-1830)".) Figure. 3.11 B shows an image of the cervical spine region on a volunteer acquired with the printed array using a T2-weighted spin echo sequence: TE 114.8 ms. TR 3500 ms, FA 90°, and 2 averages on a General Electric 3T scanner. The image in Fig. 3.11 B also shows uniform sensitivity along the spine from high SNR provided by the closely fitting array elements. The improved coverage and sensitivity of flexible coil arrays is also illustrated in Fig 3.11 C and D which compares images in taken with a single element to those taken with the array. The image produced from the array in Fig. 311 D has much more coverage and SNR in the meniscus region highlighted than the one from the single coil in Fig 3.11 C. Knee scans used a T2-weighted TSE with sequence parameters of TE of 39 ms, TR 3000ms, FA 150°, and 1 average.

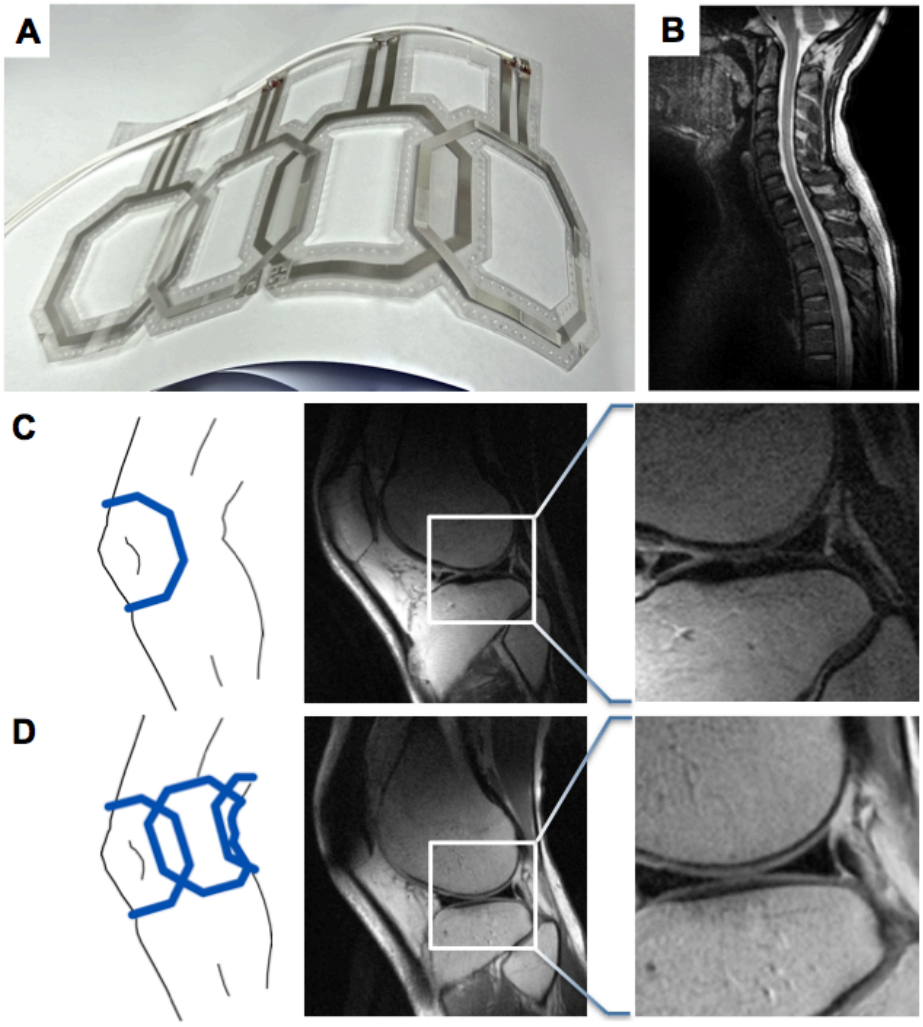

Figure 3.11: **A.** Proof of concept, prototype of printed flexible 4-channel receive array. **B.** Sagittal cervical spine MRI image showing excellent penetration due to the conformity of the array. **C.** Single element MRI image of a knee. **D.** Scan showing the expected improved penetration using a 4-channel array wrapped around the leg of a volunteer. Highlighted areas show region of interest with higher SNR from increased field of view from array. [Reproduced with permission from Corea et al. [2]]

Even though our prototype array did not focus on optimizing array geometry, coupling, or fit it produced high-quality images. Utilizing printing as a technique, other arrays with more elements can be built that include strain relief cuts, pre-curved substrates, more conformable materials, or advanced topography to better address even complex areas of the body - however this advanced approach is beyond the scope of this work.

3.6 Conclusions

The methods outlined in this chapter for printing receive coil arrays addresses the imaging limitations of poorly fitting coils by producing highly flexible, lightweight devices that conform to the human body. We provide a detailed analysis of the materials properties and the performance of the printed components. Using this material characterization, we created the first fully functional, printed and flexible MRI coils, and array for 1.5 and 3 T clinical scanners. Our unique designs achieved a remarkable 80–93% of the control coil's SNR depending on materials and construction. While current custom-built conventional coils have less intrinsic loss compared with current printed materials, it is impractical for custom traditional arrays to be built for each patient. The ease of adjustability in the printing process lends itself well to new geometries and materials, as is shown with our coil using the substrate as the dielectric. While printed coils with solution processed dielectric capacitors exhibit lower SNR in a one-to-one comparison with control coils, printed coils that use the PEEK substrate as the dielectric display less loss. In fact, they near the performance of the control coils, in a typical sample-loaded, sample-noise dominated regime. Additionally, when the printed coils conform to patients and can be placed in close proximity to the body, they provide similar or better image quality than conventional ones that do not necessarily fit as well. The printed array integrated into a baby blanket is extremely lightweight and provides new opportunities for conformity and comfort with a mass manufacturing technique.

These printed coils discussed here form the basis for the optimization and application specific designs discussed in the following chapters.

3.7 References

[1] J. T. Vaughan and J. R. Griffiths, *RF coils for MRI*. Chichester, West Sussex: John Wiley and Sons Ltd., 2012.

[2] J. R. Corea, A. M. Flynn, B. Lechene, G. Scott, G. D. Reed, P. J. Shin*, et al.*, "Screen-printed flexible MRI receive coils," *Nat Commun,* vol. 7, p. 10839, 2016.

[3] L. D. Landau and E. M. Lifshitz, *The classical theory of fields*, 3d rev. English ed. Oxford, New York,: Pergamon Press, 1971.

[4] P. B. Roemer, W. A. Edelstein, C. E. Hayes, S. P. Souza, and O. M. Mueller, "The NMR phased array," *Magn Reson Med,* vol. 16, pp. 192-225, 1990.

[5] W. A. Edelstein, G. H. Glover, C. J. Hardy, and R. W. Redington, "The intrinsic signal-to-noise ratio in NMR imaging," *Magn Reson Med,* vol. 3, pp. 604-18, Aug 1986.

[6] L. Darrasse and J. C. Ginefri, "Perspectives with cryogenic RF probes in biomedical MRI," *Biochimie,* vol. 85, pp. 915-37, 2003.

[7] B. H. Suits, A. N. Garroway, and J. B. Miller, "Surface and gradiometer coils near a conducting body: the lift-off effect," *J Magn Reson,* vol. 135, pp. 373-9, 1998.

[8] M. Rudin, *In-Vivo Magnetic Resonance Spectroscopy I: Probeheads and Radiofrequency Pulses Spectrum Analysis*. Berlin, Heidelberg: Springer Berlin Heidelberg,, 1992.

[9] J. A. Nordmeyer-Massner, N. De Zanche, and K. P. Pruessmann, "Stretchable coil arrays: application to knee imaging under varying flexion angles," *Magn Reson Med,* vol. 67, pp. 872-9, Mar 2012.

[10] J. A. Malko, E. C. McClees, I. F. Braun, P. C. Davis, and J. C. Hoffman, Jr., "A flexible mercury-filled surface coil for MR imaging," *AJNR Am J Neuroradiol,* vol. 7, pp. 246-7, Mar-Apr 1986.

[11] J. Rousseau, P. Lecouffe, and X. Marchandise, "A new, fully versatile surface coil for MRI," *Magn Reson Imaging,* vol. 8, pp. 517-23, 1990.

[12] G. Adriany, P. F. Van de Moortele, J. Ritter, S. Moeller, E. J. Auerbach, C. Akgun*, et al.*, "A geometrically adjustable 16-channel transmit/receive transmission line array for improved RF efficiency and parallel imaging performance at 7 Tesla," *Magn Reson Med,* vol. 59, pp. 590-7, Mar 2008.

[13] F. C. Krebs, "Fabrication and processing of polymer solar cells: A review of printing and coating techniques," *Solar Energy Materials and Solar Cells,* vol. 93, pp. 394-412, 2009.

[14] A. C. Arias, J. D. MacKenzie, I. McCulloch, J. Rivnay, and A. Salleo, "Materials and applications for large area electronics: solution-based approaches," *Chem Rev,* vol. 110, pp. 3-24, 2010.

[15] C. D. Muller, A. Falcou, N. Reckefuss, M. Rojahn, V. Wiederhirn, P. Rudati*, et al.*, "Multi-colour organic light-emitting displays by solution processing," *Nature,* vol. 421, pp. 829-833, Feb 20 2003.

[16] H. Yan, Z. H. Chen, Y. Zheng, C. Newman, J. R. Quinn, F. Dotz*, et al.*, "A high-mobility electron-transporting polymer for printed transistors," *Nature,* vol. 457, pp. 679-U1, Feb 5 2009.

[17] A. Pierre, M. Sadeghi, M. M. Payne, A. Facchetti, J. E. Anthony, and A. C. Arias, "All-printed flexible organic transistors enabled by surface tension-guided blade coating," *Adv Mater,* vol. 26, pp. 5722-7, Aug 27 2014.

[18] G. Schwartz, B. C. Tee, J. Mei, A. L. Appleton, H. Kim do, H. Wang*, et al.*, "Flexible polymer transistors with high pressure sensitivity for application in electronic skin and health monitoring," *Nat Commun,* vol. 4, p. 1859, 2013.

[19] C. M. Lochner, Y. Khan, A. Pierre, and A. C. Arias, "All-organic optoelectronic sensor for pulse oximetry," *Nat Commun,* vol. 5, p. 5745, 2014.

[20] D. H. Kim, J. H. Ahn, W. M. Choi, H. S. Kim, T. H. Kim, J. Z. Song*, et al.*, "Stretchable and foldable silicon integrated circuits," *Science,* vol. 320, pp. 507-511, Apr 25 2008.

[21] S. Vasanawala, T. Grafendorfer, P. Calderon, G. Scott, M. Alley, M. Lustig*, et al.*, "Millimeter Isotropic Resolution Volumetric Pediatric Abdominal MRI with a Dedicated 32 Channel Phased Array Coil," presented at the International Socieity of Magentic Resosnance and Medicine 19, Montreal, Canada, 2011.

[22] D. P. Frush, G. S. Bisset, and S. C. Hall, "Pediatric sedation in radiology: The practice of safe sleep," *American Journal of Roentgenology,* vol. 167, pp. 1381-1387, Dec 1996.

[23] K. P. Mason, D. Zurakowski, S. E. Zgleszewski, C. D. Robson, M. Carrier, P. R. Hickey*, et al.*, "High dose dexmedetomidine as the sole sedative for pediatric MRI," *Pediatric Anesthesia,* vol. 18, pp. 403-411, May 2008.

[24] J. l. Mispelter, M. Lupu, and A. Briguet, *NMR probeheads for biophysical and biomedical experiments : Theoretical principles & practical guidelines*. London: Imperial College Press, Distributed by World Scientific, 2006.

[25] J. R. Corea, P. B. Lechene, M. Lustig, and A. C. Arias, "Materials and Methods for Higher Performance Screen-Printed Flexible MRI Receive Coils," *Magn Reson Med,* Sep 9 2016.

[26] K. P. Pruessmann, M. Weiger, M. B. Scheidegger, and P. Boesiger, "SENSE: sensitivity encoding for fast MRI," *Magn Reson Med,* vol. 42, pp. 952-62, 1999.

[27] M. A. Griswold, P. M. Jakob, R. M. Heidemann, M. Nittka, V. Jellus, J. Wang*, et al.*, "Generalized autocalibrating partially parallel acquisitions (GRAPPA)," *Magn Reson Med,* vol. 47, pp. 1202-10, 2002.

[28] C. E. Hayes and L. Axel, "Noise Performance of Surface Coils for Magnetic-Resonance Imaging at 1.5-T," *Medical Physics,* vol. 12, pp. 604-607, 1985.

[29] American Radio Relay League., "The ARRL handbook for radio communications," in *Radio amateur's library publication no 6*, ed. Newington, CT: ARRL, 2002, p. v.

Chapter 4

4. Optimization of Printed Coils

4.1 Introduction

For receive coils in a clinical scanner, the two main sources of loss that reduce image SNR are the properties of the receive coil and the sample it is imaging [1, 2]. While the materials used in coil fabrication contribute to these losses, at 1.5 and 3 T, the majority of loss is contributed by the patient (i.e., the sample) [1]. A common way to characterize the origin of the losses (i.e., the effective resistance) generated by a coil-sample system, is to measure the coil's quality factor (Q) with and without the presence of a conductive (i.e., loading) material – Q_{Loaded} and $Q_{Unloaded}$ respectively [3]. The losses associated with materials used in the fabrication of coils can be inferred from the value of $Q_{Unloaded}$, while Q_{Loaded} provides insight on loss contribution from the sample. Higher Q indicates less loss, which translates into better SNR in images [4].

As stated in previous chapters, the current strategy used in conventional coil fabrication is to get the highest possible $Q_{Unloaded}$ by using materials with very low electrical loss such as thick bulk copper traces and high quality porcelain capacitors [5]. This method works well in cases where the sample noise is not the dominant factor, as is the case in low frequency MR, NMR systems, or preclinical imaging where both sample and coils are small. However in clinical scenarios where the patient is the largest source of loss, as the coil's $Q_{Unloaded}$ continues to increase, only a marginal increase in SNR is observed [1]. This reduces the need to use inflexible high quality materials for the coil construction, allowing array designers to use unconventional materials for the coil fabrication without incurring a large SNR penalty [6, 7]. These new materials offer other benefits, for example, while conductive traces screen-printed from solution are less conductive than copper foil they enable a coil that is more flexible and lightweight compared to what can be achieved with traditional materials [8].

We have shown in chapter 3 that flexible screen-printed coils with relatively low $Q_{Unloaded}$ could generate SNR in images within 20% of a high quality traditionally made coil. [6]. Furthermore, the high flexibility of printed coils enables them to surpass conventional coils when they fit better and are closer to the sample [6]. Printing also represents a quick fabrication pathway, ideal for unique applications, as was previously shown by inkjet printing coils on polyimide film for use in small animal systems [9] and 3D printed NMR coils [10]. While the results of previous work have been promising, image SNR from printed coils still lags behind conventional coils when compared in identical situations, mostly due to the quality of the materials. In particular, the printed capacitor's dielectric has been identified as an area of possible improvement [6].

In this chapter, fabrication methods and materials are explored for printed coils to produce high image SNR. Specifically this chapter focuses on a coil design where the substrate also acts as the capacitor's dielectric instead of the printed dielectric detailed in chapter 3. Careful selection and optimization of the low-loss plastic substrate material provides significant gains over previously printed capacitor dielectric materials. To this

end, an experimental apparatus is created to mimic the printed coil geometry by using copper foil for the traces. This apparatus enables rapid characterization of the dielectric properties of plastic substrates allowing several substrates to be rapidly screened. This quickly identifies the most suitable dielectric for printed coils. The influence of the printed silver trace properties on the $Q_{Unloaded}$ of the coils is also investigated. To guide the optimization of the printed coils, an experimental procedure that relates a coil's $Q_{Unloaded}$ to its SNR in images of a representative phantom is developed. From these optimizations, a coil with $Q_{Unloaded}$ values of 100 provides 97% of the SNR that a traditional coil produces on a representative phantom at 3 T. Finally, optimized coils are assembled into an 8-channel array for a 3T scanner. The SNR and noise correlation of this array are characterized on a conductive phantom and its performance is demonstrated by scanning the head of a volunteer. These results are compared to a commercial 12-channel array (Siemens 3T Head MATRIX A Tim Coil).

4.1.1 Predicting SNR

In this section an experimental method is developed to relate the $Q_{Unloaded}$ of a coil with the SNR it will produce in an image of a conductive phantom to aid in the characterization of the printed coil materials.

If the $Q_{Unloaded}$ and Q_{Loaded} on a particular phantom are known, the efficiency of a coil can be predicted using equation 1.11 from Rudin et al. [3] (reproduced here), where SNR_0 is the intrinsic SNR. [11, 12]

$$SNR = SNR_0\sqrt{1 - \frac{Q_{Loaded}}{Q_{Unloaded}}} \tag{1.11}$$

Another way to evaluate the coil materials is to relate the $Q_{Unloaded}$ of coils to the SNR in images by estimating the loss contribution from the sample.

The Q_{Loaded} of a coil-sample system is related to the total loss of the system, with contributions from the coil materials (R_{Coil}) and the sample (R_{Sample}). $Q_{Unloaded}$ is only influenced by R_{Coil} while R_{Coil} and R_{Sample} affect Q_{Loaded}. Equation 4.1 and 4.2, from Rudin et al. [3] describe the relationship between coil loss and Q using the inductance of the coil (L), and the resonance frequency (ω) [1, 4, 13].

.

$$Q_{Loaded} = \frac{\omega L}{R_{Coil} + R_{Sample}} \propto \frac{1}{R_{Coil} + R_{Sample}} \tag{4.1}$$

$$Q_{Unloaded} = \frac{\omega L}{R_{Coil}} \propto \frac{1}{R_{Coil}} \tag{4.2}$$

The SNR of an image obtained from a coil can then be related to its Q_{Loaded}, as described by equation 4.3 [3, 4, 14, 15].

$$SNR \propto \sqrt{Q_{Loaded}} \tag{4.3}$$

There are a multitude of factors that impact image SNR and affect the coefficient of proportionality implied in equation 4.3. To determine a coil's performance without having to estimate this coefficient, one strategy is to compare it with a geometrically identical coil known to have low-loss (i.e., a coil which has an efficiency of approximately 99% or greater). If two coils have the same geometry and are in the same position, then L and R_{Sample} are not significantly changed. Making this assumption, it is then possible to predict the relative SNR in images obtained from a test coil with the SNR obtained from a high quality control coil as shown in equation 4.4.

$$Relative\ SNR(\%) = \frac{\sqrt{Q_{LoadedTest}}}{\sqrt{Q_{LoadedControl}}} \tag{4.4}$$

The Q_{Loaded} of a coil can be estimated from its $Q_{Unloaded}$ and sample loss factor (R_{Sample}) by equation 4.5.

$$Q_{Loaded} \propto \left(\frac{1}{Q_{Unloaded}} + R_{Sample}\right)^{-1} \tag{4.5}$$

Measuring $Q_{Unloaded}$, Q_{Loaded}, and SNR of several coils allows the estimation of R_{Sample} for a particular phantom. Finally, by combining equations 4.4 and 4.5, the relative SNR of a test coil can be compared to that of a control coil from the measurement of its $Q_{Unloaded}$ as is shown in equation 4.6.

$$Relative\ SNR(\%) = \sqrt{\frac{(Q_{UnloadedControl})^{-1} + R_{Sample}}{(Q_{UnloadedTest})^{-1} + R_{Sample}}} \tag{4.6}$$

4.2 Fabrication

Coils using a plastic substrate as the dielectric are fabricated by printing the metal features on each side of the substrate. Fig. 4.1 A illustrates the fabrication process and shows the overlapped portions of the metal traces sandwich the substrate, forming integrated tuning and matching capacitors, further highlighted in Fig. 4.1 B [6, 16]. The area of overlap between the two plates of the capacitors, as well as the substrate's thickness, determines the resulting capacitance. Adding or removing ink on each side of the substrate controls the capacitor area, and in turn, tunes the coil. This method is the same technique used to make the substrate dielectric coil briefly discussed in chapter 3. Figure 4.2 A shows an example of a completed coil, note that the capacitors are distributed over a larger area, and have approximately 18 mm of overlap. Figure 4.2 B shows the exact dimensions of the 8.75 cm diameter octagonal coils, highlighting the

width of 5 mm traces. The total thickness of the coil is 125 µm, contributing to the overall flexibility of the device.

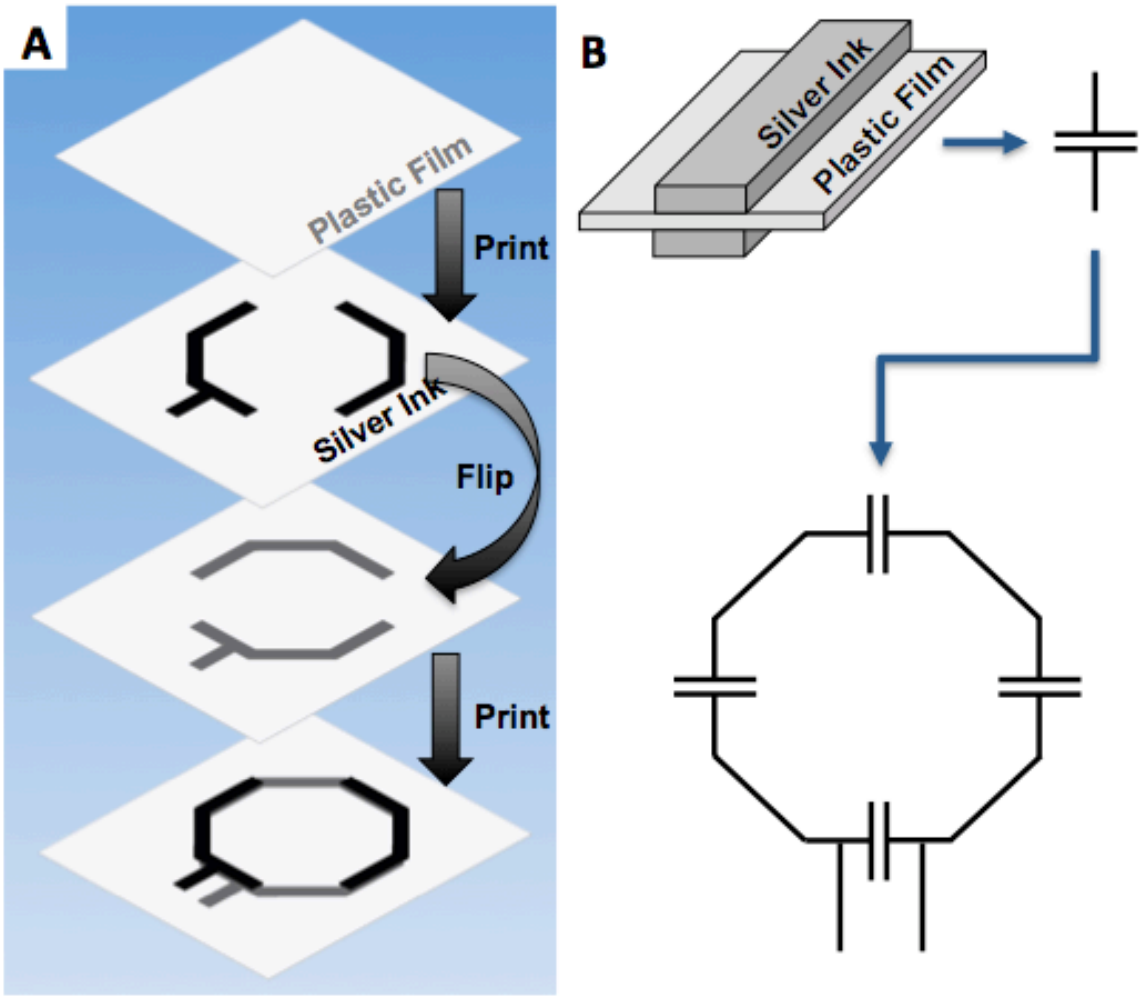

Figure. 4.1: **A.** Illustration of the printed coils fabrication process. Conductive features are printed on each side of the substrate to form tuning and matching capacitors. **B.** Cross-section schematic of coil capacitors formed between two printed metal features and the plastic substrate along with the equivalent circuit of the printed portion of the receive coil.

Multi-channel coil arrays can be fabricated by shifting the single coil pattern during the printing process to an adjacent position on the substrate. Figure 4.3 A shows an example of a multichannel array built in this way. Note that the array maintains the flexibly that the single channel coil had in Fig 4.2 A. Figure 4.3 B details the overlapping scheme used to make a multichannel coil array highlighting how coils overlap front and back. The critical overlap distance to decouple adjacent elements is determined by positioning coils so that their $|S_{12}|$ interaction is minimized [17-19]. The overlap between each single coil element in the array is 11.7 mm, which results in approximately 29 cm of lateral coverage for a 4-channel array, as detailed in figure 4.3 B.

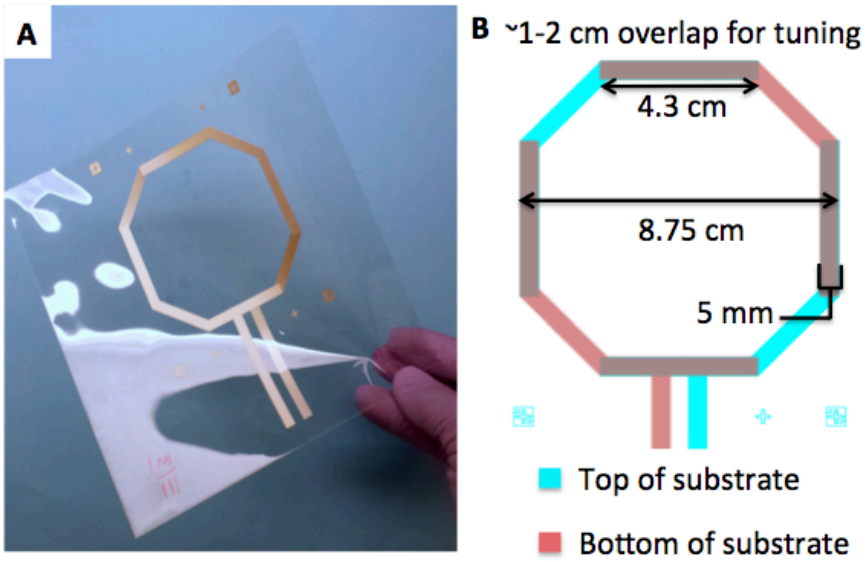

Figure 4.2: **A.** Photograph of a single element printed flexible coil. **B.** Detailed dimensions of the printed coils.

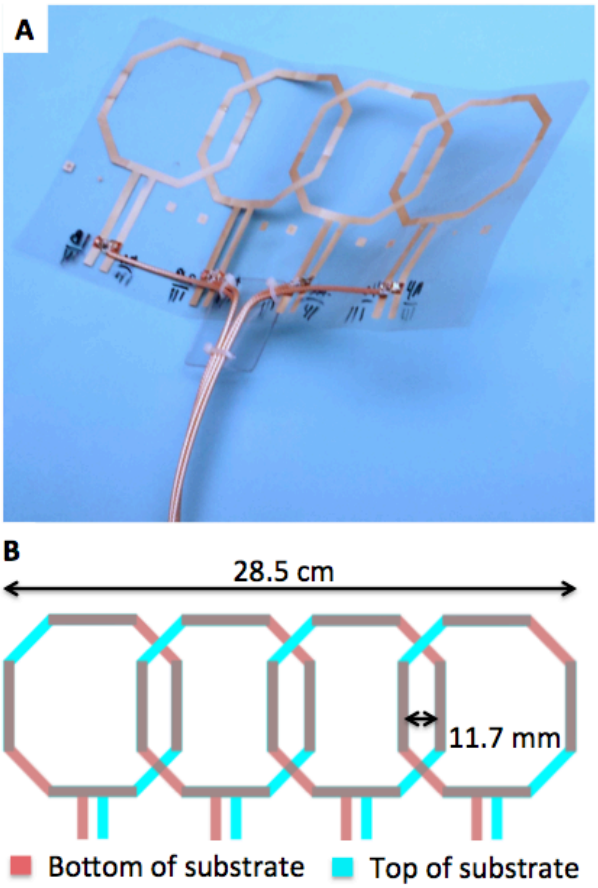

Figure 4.3 **A.** Photograph of coil array. Transmission lines connecting the coils to the MRI scanner are also shown coming out of the bottom of coil array. **B** Single coil elements are shifted to adjacent positions to form a multi-channel array.

4.2.1 Dielectric Optimization

In the coil configuration used in this chapter, the loss characteristics of the plastic substrate directly impact the quality of the printed capacitors and the image SNR. Dielectric loss is reported for most plastic substrates at limited standard set of frequencies, but rarely at frequencies common to clinical MRI (i.e., 64, 123.3 and 127.7 MHz). To characterize the dielectric properties of several materials, the flat plastic substrates are clamped between two 7 mm thick acrylic plates with 70 μm thick copper traces (resistivity = 1.68×10^{-6} Ω-cm) in the same geometry as our coil. Fig. 4.4 A shows an illustration of this testing rig with a cross-section highlighting the material stack. Acrylic was chosen for the plates due to its ease of manufacturing, isotropic (orientation independent) electrical properties, ability to withstand clamping forces, and transparency – which aids in positioning the coils. Other mechanically stable materials with low dielectric constant could be used for this fixture, including commonly available fiberglass reinforced circuit board. It should be noted that the acrylic plates of the testing rig contribute a small amount to the overall coil capacitance since their dielectric constant is higher than air. To characterize this interaction, completed coils with printed conductor were clamped in the test rig without the copper film to measure any shift in resonance frequency or Q. Resonance frequency shifted down 1.4 MHz on average, implying an increase of ~0.25 pF from the testing rig. We hypothesis that this increase in capacitance is due to the fringe fields interacting with the increased dielectric constant of the acrylic testing rig that surrounds it while it is being measured. Quality factor with and without the acrylic plates changed less than 0.3%, indicating any contribution from the acrylic plates is negligible.

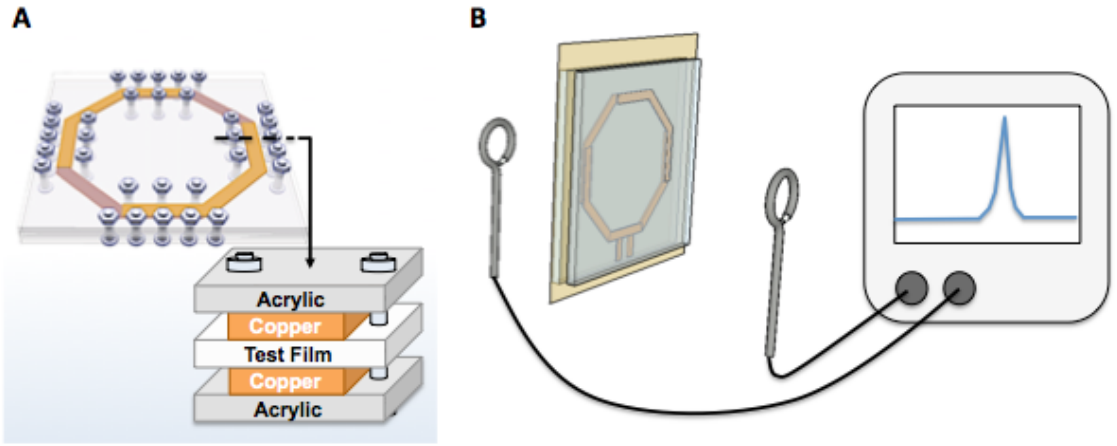

Figure 4.4: **A.** Illustration of the testing rig developed to characterize the dielectric loss of flexible substrates prior to printing. This setup mimics the geometry of the printed coils. The stack of materials is highlighted in lower right. **B.** Illustration of $Q_{Unloaded}$ measurement setup using two probes separated by several diameters with test rig in the center.

For each substrate tested, the lengths of the metal traces are adjusted to obtain coil resonance at 123.3 MHz – the Larmor frequency of our scanner. To measure $Q_{Unloaded}$, the coils are placed at least 50 cm away from any conductive material and the $|S_{12}|$ response from two lightly coupled probes is recorded [4]. Figure 4.4 B illustrates this measurement setup with the two magnetic field probes spaced several diameters apart around the test rig. Probes were decoupled by separating them until the $|S_{12}|$ response without a coil present was below -70 dB. To prevent the probes from influencing the measurement, light coupling to the coil under test was ensured by keeping any $|S_{11}|$ or $|S_{22}|$ response above 100 mdB. The Q is measured on a calibrated Agilent E5061B ENA network analyzer with 1601 points averaged 16 times, centered at the Larmor frequency (123.3 MHz) with the vector network analyzer set to a frequency span of 25 MHz. It is important to note that the Q measured on a network analyzer in this way is dependent on the position, orientation, calibration, frequency sweep/span, and day-to-day variation of the experimental setup. This includes the difficult to control for humidity and temperature dependent film parameters. To best account for these variations, our experimental setup was characterized to have a repeatability of 5% by measuring our control coil several times on different days.

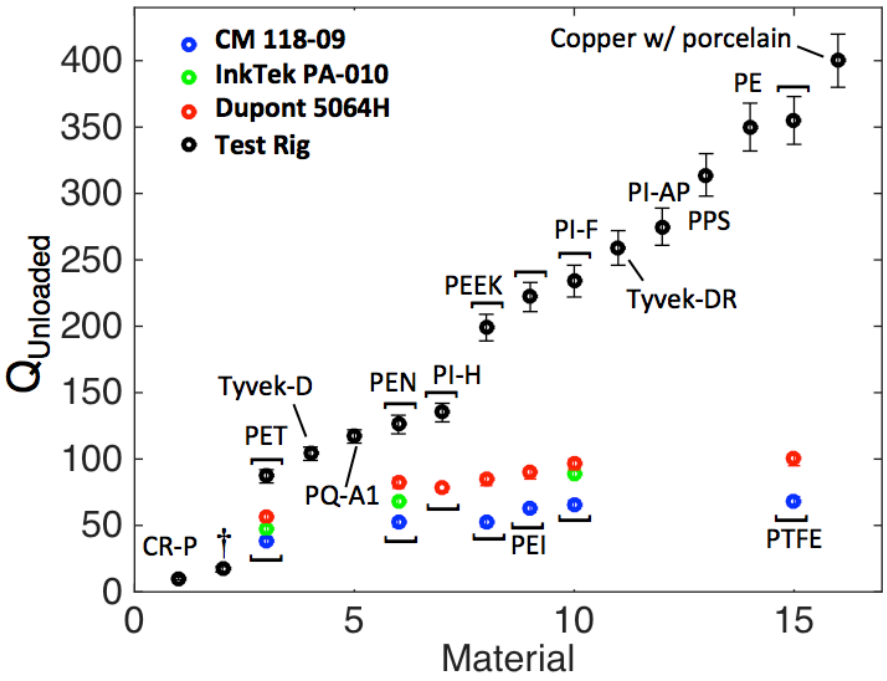

Figure 4.5: Summary of $Q_{Unloaded}$ of coils obtained with flexible substrate from the testing rig and printed conductive inks. Black points are results from testing rig with copper traces. Blue, green, and red points are from coils printed with CM 118-09, PA-010 and Dupont 5046H respectively. † Denotes the use of the dielectric ink from previous work (10). PTFE is identified as the dielectric with the lowest loss, as it has a highest $Q_{Unloaded}$ in the testing rig at 355 while PET shows the lowest at 87.

The characterized plastic substrates are selected based on their compatibility with the printing process. The substrates studied are commercially available in a thickness

between 50-150 μm, able to withstand at least 125°C during annealing, and mechanically stable enough to be handled during processing. The plastic substrates tested are polyethylene (PE), polyethylene terephthalate (PET), polyethylene-napthalate (PEN), polyethylene-napthalate with an adhesion layer (PQA1), kapton 100HN (PI-N), kapton 200FN919 (PI-F), polyphenylene sulfide (PPS), polyetherimide (PEI), polyether ether ketone (PEEK), polytetrafluoroethylene (PTFE), cleanroom paper cellulose with acrylic binder (CR-P), tyvek 1025D (Tyvek D), tyvek brillion 4173DR (Tyvek DR), and pyralux AP (PI-AP).

Table 4.1: $Q_{Unloaded}$ of printed coils and substrates in testing rig. A mark of "-" denotes that the ink was unable to adhere to material. †Printed coils from previous work [6] were tested with a printed conductor, not in the copper and acrylic test rig.

Substrate	Testing rig 1.68e-6 Ω•cm	CM 118-09 7.99e-5 Ω•cm	IT PA-101 3.94e-5 Ω•cm	DP 5064H 1.84e-5 Ω•cm
Copper Coil with ATC Capacitors	400 ± 20	-	-	-
Polytetrafluoroethylene (PTFE)	355 ± 18	68.7 ± 3	-	100 ± 5
Poly Ethylene (PE)	350 ± 18	-	-	-
Polyphenylene Sulfide (PPS)	314 ± 16	-	-	-
Pyralux AP (PI)	275 ± 14	-	-	-
Tyvek Brillion 4173DR (TyvekDR)	259 ± 13	-	-	-
Kapton 200FN919 (PI-N)	234 ± 12	66 ± 3	89 ± 5	97 ± 5
Ultem Polyetherimide (PEI)	222 ± 11	63 ± 3	-	90 ± 5
Polyetheretherketone (PEEK)	199 ± 10	52 ± 3	-	85 ± 5
Kapton 100HN (PI)	135 ± 7	-	-	79 ± 4
Polyethylene Naphthalate Q65HA (PEN)	126 ± 7	52 ± 3	68 ± 4	83 ± 5
Polyethylene Naphthalate PQA1 (PQA1)	117 ± 5	-	-	-
Tyvek 1025D (TyvekD)	104 ± 5	-	-	-
Polyethylene Terephthalate (PET)	87 ± 5	38 ± 2	48 ± 3	57 ± 3
Prior Printed Coils [6]	17 ± 2†	-	-	-
Clean Room Paper (CR-P)	10 ± 2	-	-	-

Figure 4.5 summarize the $Q_{Unloaded}$ of all substrates tested in the copper/acrylic testing rig as well as the $Q_{Unloaded}$ of some printed coils made from the same substrates with the three silver inks (tabulated in table 4.1). The $Q_{Unloaded}$ in the testing rig ranges from 10 for CR-P to 355 with PTFE, which is very close to the $Q_{Unloaded}$ of control coils made with high quality porcelain capacitors. However, for the printed coils the $Q_{Unloaded}$ for all 3 silver inks do not reach values higher than 100 despite using substrates that achieve high $Q_{Unloaded}$ in the copper test rig. For example, the PTFE film has the highest $Q_{Unloaded}$ in the copper test rig, but when a printed conductor is used, the $Q_{Unloaded}$ is 100, which is not significantly higher than a printed coil made with PI-F, PEI, or PEEK.

Since high conductivity copper foil is used for the conductive part of the loop, it can be assumed that the coil losses are dominated by the dielectric losses, and therefore $Q_{Unloaded}$ is an indirect measurement of the dielectric quality of each tested material. The gap seen in $Q_{Unloaded}$ between the printed and test rig coils in Fig. 4.5 indicates that, for most substrates, the $Q_{Unloaded}$ of printed coils is limited by the conductivity of the printed

conductors. However, on the substrates that display higher loss, such as PET, changing the silver ink only raises $Q_{Unloaded}$ from 38 to 57 suggesting that the low values of $Q_{Unloaded}$ stem from losses of both the substrate and the conductive ink.

Overall, these results illustrate the potential of plastic substrates to be used as the dielectric in printed capacitors to produce very high $Q_{Unloaded}$ printed coils. However, when printed conductors are used, they tend to limit the maximum values attainable for $Q_{Unloaded}$. As a result, other substrate properties, such as mechanical or thermal stability, can be taken into account to select the best suitable substrate for a particular application of printed coils. Reducing the losses generated by the printed conductors represents a major avenue for improving the $Q_{Unloaded}$ of printed coils and is discussed in the following section.

4.2.2 Conductive Ink Optimization

One method to increase the conductivity of printed silver traces, and in turn coil $Q_{Unloaded}$, is to increase the trace thickness, as illustrated in Fig. 4.6 A. Three different silver-based conductive inks are compared. Micro-flake Creative Materials 118-09, nanoparticle InkTek PA-010, and micro-flake DuPont 5064H (with resistivity of 7.99×10^{-5} Ω-cm, 3.94×10^{-5} Ω-cm, and 1.84×10^{-5} Ω-cm respectively as measured by 4-point probe). Prior to printing, the substrates are preheated to 140 °C for 10 minutes and cooled again at room temperature to relieve any stress and prevent distortion in future processing steps. Then, the conductive inks are screen-printed (ASYS Group ASP01M, Dornstadt: Germany) through a 400 mesh-count stainless steel mesh onto the flexible substrate and annealed at 140 °C for 15 min. This procedure is repeated on the reverse side of the flexible substrates, completing the coils. Printing multiple layers also allows variation of the thickness of the conductive trace, with each layer adding 5 µm to the printed conductor.

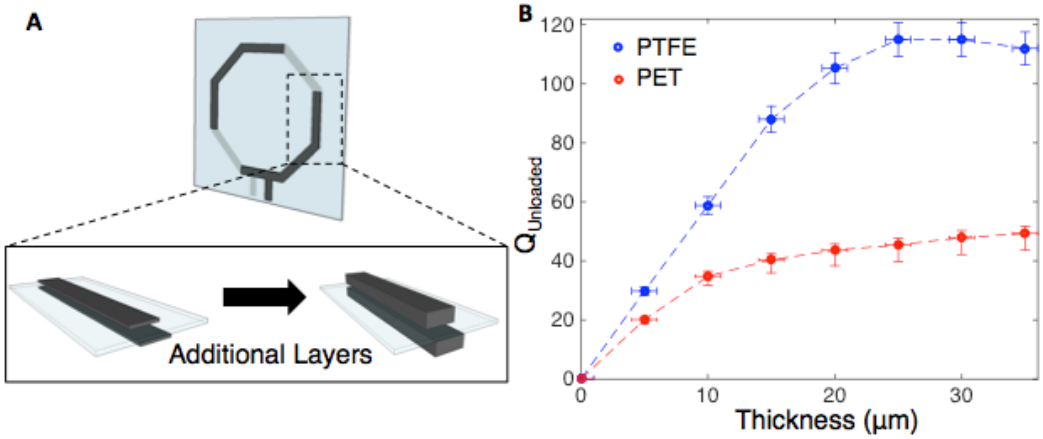

Figure 4.6: **A.** Illustration of a printed coil with inset showing an increase of the printed layer (grey) thickness, obtained by printing additional layers of conductor. **B.** $Q_{Unloaded}$ of coils made with increasing thickness of DuPont 5064H silver ink for highest (PTFE) and lowest (PET) performing flexible substrates in blue and red. [Reproduced with permission from Corea et al. [7]]

Coils with conductive trace thicknesses of 5-35 μm are examined to characterize the relationship between conductive film thickness, coil $Q_{Unloaded,}$ and mechanical stability. Conductive trace thickness was measured using a stylus profilomter (Dektak 6M Stylus Profilometer, Veeco: Oyster Bay, New York). This characterization is performed with the highest conductivity ink (DuPont 5064H) on low-loss (PTFE) and higher-loss (PET) substrates to show the relative benefits of the conductive ink optimization.

Figure 4.6 B shows that as the thickness of the silver ink was increased from 5 to 35 μm on the PET and PEEK substrates, a diminishing return in coil $Q_{Unloaded}$ was observed above 20 μm of ink. Furthermore, it was seen that the silver thickness has a more dramatic influence on $Q_{Unloaded}$ with the PTFE substrate than PET due to the higher dielectric loss of PET.

In Fig 4.6 B it is also shown that thicker films of printed conductor do not significantly improve $Q_{Unloaded}$. This is because the current density distribution at 127 MHz causes more charge to move near the surface of the conductor rather than in the center [20]. Past a certain thickness the current near the center of the conductor is negligible, creating a situation where thicker films do not significantly increase the coil Q. A slight decrease in $Q_{Unloaded}$ is seen for the thickest conductive silver films on PTFE, where an increase in the trace resistivity is observed. This increase in trace resistivity is due to the silver ink cracking and delaminating from the substrate, limiting the current flow. Based on those observations, a thickness of 15 μm of silver printed from the DuPont 5064H ink is chosen as the optimal fabrication parameter for subsequent coils to maintain sufficient SNR while avoiding film cracking.

4.2.3 Single Coil Optimization

Coils are made for SNR measurements by printing DuPont 5064H silver ink on several types of substrates. The coils are tuned to the Larmor frequency of protons of our 3T scanner (123.3 MHz - 3T Siemens TIM Trio, Erlangen: Germany) and have an input impedance of 50 Ω when loaded [20]. To serve as reference, control coils are fabricated by soldering high quality ATC capacitors on 35 μm thick copper traces on Pyralux AP substrates. The geometry of the control coil is identical to the printed ones. To predict the SNR of printed coils without scanning, Q_{Loaded} is measured and compared to that of a control coil. To load the coils, they are placed directly on top of a water filled 7L cubic phantom doped with 3.356 g/L $NiCl_2*6H_20$ and 2.4 g/L NaCl for conductivity of 0.68 S/m at 123 MHz. The acrylic walls of the phantom were 6.4 mm thick. The values of Q_{Loaded} obtained for the substrates tested are tabulated in table 4.2. The Q_{Loaded} are then used to predict the image SNR using equation 4.6 also shown in table 4.6.

Some of the substrates tested, specifically PPS, PE, Tyvek-D, Tyvek-DR, and cleanroom paper, could not be used to fabricate printed coils because the 140 °C temperature in the curing step caused significant warping or melting of the substrates. PQ-A1 is a poor candidate for this process because of a Q-lowering adhesion layer that was only on one side of the film, additionally polyimide based Pyralux AP was not available without a copper cladding. Some inks did not adhere well to all the substrates and delaminated preventing a complete coil circuit to be formed. As a result, these substrates are not included in table 4.2.

To get a direct measurement of SNR, the coils are used to image the conductive phantom on a 3T scanner (3T Siemens TIM Trio, Erlangen: Germany). Figure 4.7 A

illustrates how the coil is positioned on the phantom to load coils. A 2D gradient echo sequence (GRE) with TE of 10 ms, TR of 438 ms, FA of 25°, and slice thickness of 5 mm is used to scan. The field of view is 200x200 mm^2 with resolution of 256 phase encodes and readouts. Printed portions of the coil were clamped into a test board which contained a PIN diode to deactivate the coil during the transmit phase of each scan. This board is connected to a gateway box (Stark Contrast, Erlangenm Germany) containing preamplifiers via half-wavelength long coaxial RG-316 cable. Several cable traps are placed on the half-wavelength coaxial cable to reduce coupling of the cable to the scanner's body transmit coil. The SNR of images is measured by dividing the average signal (i.e., the average magnitude from a 4 x 18 cm region of pixels along the entire length of the phantom) by an estimate of the noise standard deviation. Pixels near the center of the coil are chosen to measure the signal to avoid clipping artifacts from saturated regions near the edges of the coil where the conductor traces are located (more detail on this procedure is available in section 2.4.3). Image analysis is performed on raw data files from the scanner, rather than exported images to avoid compression and signal clipping artifacts. The noise is calculated from an area with no signal containing at least 2800 points at least 5 pixels from the edge of the image with no streaking artifacts. All SNR measurements are normalized to images taken with the traditionally made high quality ($Q_{Unloaded}$ = 400) coils. To show the benefit of using the substrate as the dielectric compared to printing the dielectric inks, a coil was fabricated using the same Creative Materials 116-20 dielectric ink as previously reported in chapter 3 [6].

Table 4.2: Bench top measurements and scanning results of SNR relative to control coils. Printed coils were fabricated with DuPont 5064H ink.

Substrate	$Q_{Unloaded}$	Q_{Loaded}	Predicted SNR	Measured SNR
Copper Coil with ATC Capacitors	400 ± 20	10.2 ± 0.3	100.0	100.0 ± 0.3
Teflon (PTFE)	100 ± 5	9.6 ± 0.3	97 ± 2	97 ± 0.7
Kapton 200FN919 (PI-N)	97 ± 5	9.4 ± 0.3	96 ± 2	95.4 ± 1.0
Ultem Polyetherimide (PEI)	90 ± 5	9.1 ± 0.3	94 ± 2	93.2 ± 0.9
Polyetheretherketone (PEEK)	85 ± 5	9.5 ± 0.3	96 ± 2	93.7 ± 0.9
Polyethylene Naphthalate Q65HA (PEN)	83 ± 5	8.9 ± 0.3	93 ± 2	94.8 ± 1.0
Kapton 100HN (PI-N)	79 ± 4	9.2 ± 0.3	95 ± 2	94.9 ± 0.6
Polyethylene Terephthalate (PET)	57 ± 3	8.5 ± 0.3	91 ± 2	91.8 ± 0.5
Prior Printed Coils[6]	17 ± 2	6.0 ± 0.3	77 ± 2	79.6 ± 0.6

The SNR extracted from images from printed coils on a conductive phantom are summarized in Fig. 4.7 B. The SNR shown in Fig. 4.7 B indicates that all coils improve significantly over the printed coil previously reported with a solution processed dielectric [6]. Furthermore, all coils are within 8% percent of SNR of the high quality control coil. The diminishing effect a coil's $Q_{Unloaded}$ has on SNR in the conductive phantom images is illustrated in Fig. 4.7 C, where $Q_{Unloaded}$ of printed coils is plotted against SNR relative to the control coil (tabulated in Table 4.2). SNR values predicted by the model described in section 4.1.1 are also shown in Fig. 4 C with the sample fitting parameter, R_{Sample}, equal to 0.087 (R^2 = 0.97). The values obtained from our predictions are in close agreement

with the values predicted using intrinsic SNR calculations from Rudin et al. - discussed previously in chapter 1. [3].

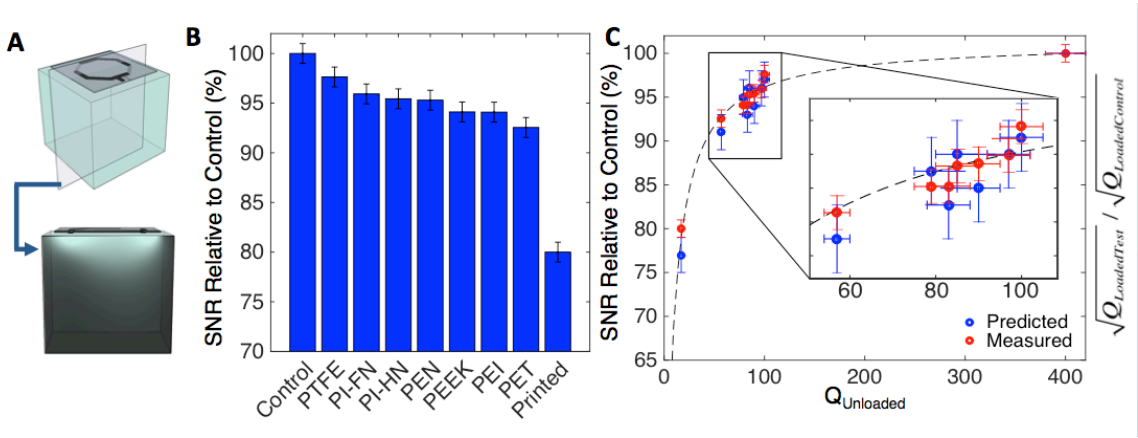

Figure 4.7: **A.** Illustration showing a coil on a 7L conductive phantom for measurements of Q_{Loaded} and image SNR. A slice of phantom is highlighted with an overlay of a scan showing the sensitivity profile for printed coils at 3T. **B.** Relative SNR of printed coils made with several substrates and Dupont 5064H silver ink loaded with a conductive phantom and measured at 3T as a percentage of the control. Measurements were taken at center of the coils along the length of the phantom. **C.** SNR relative to control vs. $Q_{Unloaded}$ for all coils as predicted from bench top measurements (blue) and on 3T scanner (red). Black dotted trend-line is the SNR trend obtained from the model described in section 4.1.1. (Reproduced with permission from Corea et al. [7])

The results shown in Fig. 4.7 C suggests that coils with a $Q_{Unloaded}$ of 100 or more would only display a marginal increase (~3%) in SNR compared to the control. Even a printed coil made of PET, which has a $Q_{Unloaded}$ of 58, displays 92% of the SNR of the control coil. To put it in perspective, a 3-8% decrease in SNR is roughly equivalent to a coil being offset from the body by only 1-1.8 cm [6]. In a worse case non-clinical scenario where the imaged sample would be non-conductive (and thus non-loading), the PTFE coil with $Q_{Unloaded}$ of 100 would still show 50% of the SNR of the control coil. Therefore, even with improvements in the properties of printed materials, only marginal improvements in SNR can be expected. However the high flexibility of printed coils may provide patients with more comfort while consistently delivering images with high SNR.

All coils made with flexible substrates show significantly improved $Q_{Unloaded}$ and image SNR than the fully printed dielectric coils described in chapter 3. This difference is attributed to the low loss the substrates display and to the higher loss in binders present in most types of printable dielectric ink.

4.2.4 Alternate Connection Method

In all the coils proposed so far, the matching capacitor has been a printed component on the coil as illustrated in Figure 4.8 A. This requires close placement of a Q spoiling inductor, diode, and any board needed to connect them to the coil (previously discussed in chapter 1). This thicker and often inflexible board can greatly inhibit the flexibility and utility of a printed array. One way to improve this circuit and make an even thinner and

lighter coil is to move these components farther away via a length of coaxial cable. Figure 4.8 B shows the circuit of a coil that accomplishes this by using a remote matching capacitor over a distance of 20 cm of cable.

To characterize the effects of having a remote blocking circuit and matching capacitor, 9 cm test coils were created with and without this length of line and imaged on a 3T scanner with the same imaging sequence and phantom as described previously. Figure 4.8 C shows the SNR from images and indicates a marginal performance loss (3%) for coils with a remote matching and tuning board. However, this small loss can be easily overcome by a well conforming purpose built array, especially if it is compared to poorly fitting array [4].

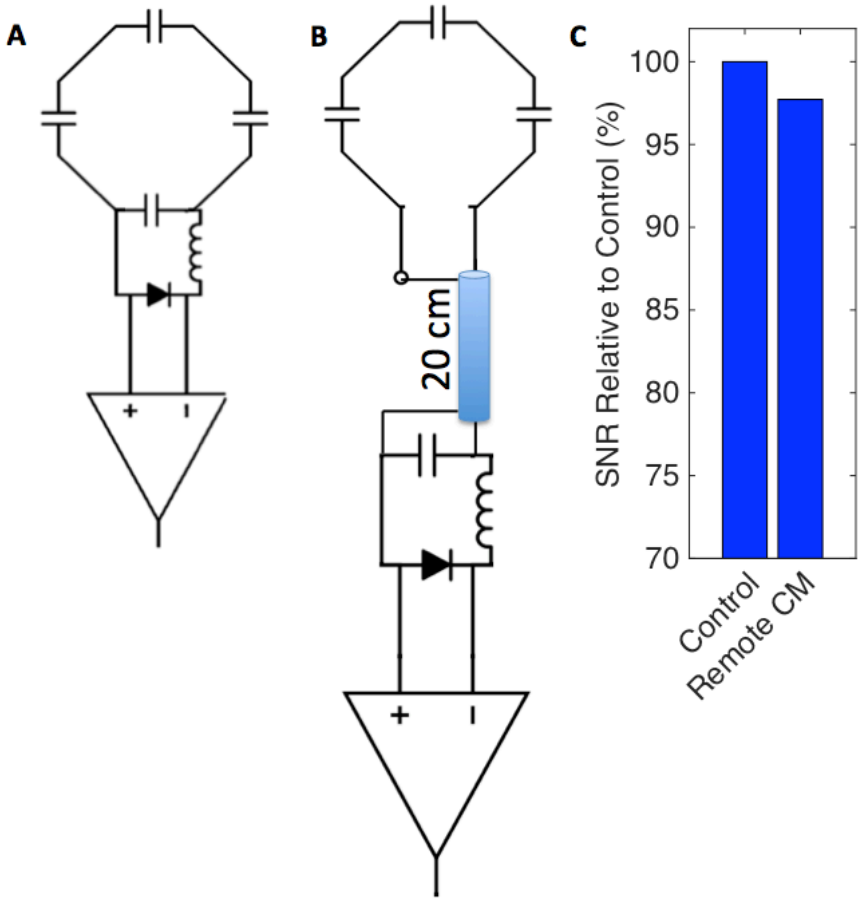

Figure 4.8: **A.** Schematic of the coil circuit with close Q-spoiling circuit. **B.** Schematic of coil with remote matching capacitor and Q spoiling circuit. **C.** SNR from scans taken with the coils using circuits shown in **A** and **B**.

4.3 Coil Array Characterization

While improved printed coil elements will create higher SNR in a printed array, it is of clinical interest to see how a printed array compares to a state of the art commercially available coil. To perform this comparison, the printed coil is compared to a production

coil on a phantom as well as on a volunteer. The commercially available array is a 12-channel Siemens 3T Head MATRIX A Tim Coil (Erlangen: Germany). The commercial array has elements approximately 25 cm long and 8 cm wide in a single row surrounding the enclosed cylindrical volume.

To simplify the processing and to be consistent with the single coil experiments, the same printed coil dimensions used for single coil characterization were kept for the printed array. The entire printed coil array is laminated in 125 μm of PTFE plastic to prevent skin contact, provide flame resistance, and maintain high breakdown strength for any DC bias that could exist on the coil. The printed array connects to the scanner in the same manner as the single coil elements, except for the interface between printed and non-printed portions. The printed films were cut to expose conductive leads that are folded over sections of non-magnetic co-axial cable and copper braid, locked into place using a brass ring crimp. Figure 4.9 shows a photograph detailing this connection between printed and non-printed components. Folding the printed and non-printed portions over each other provides a stable mechanical and electrical connection while the brass crimp holds everything in place. The entire crimped junction was then laminated in PTFE with the rest of the coil. Each of the two gateways accepts 4 channels, providing 8 channels in total. The commercial 12-chanel array uses the built-in commercial preamplifiers and connectors that can accommodate additional channels.

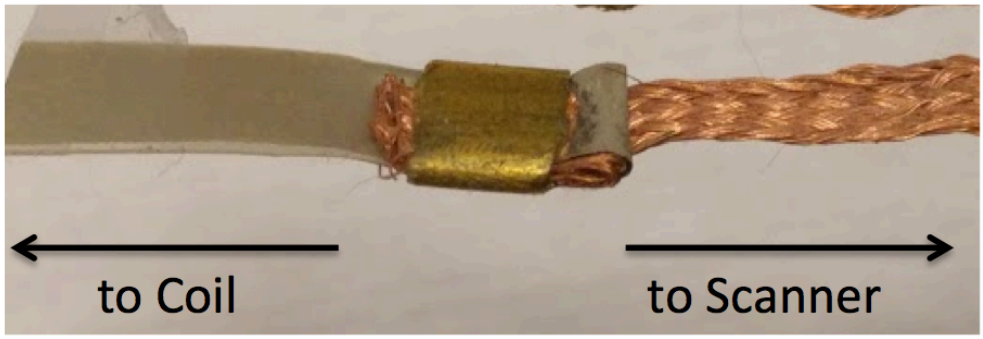

Figure 4.9: Photograph of flexible coil and copper braid crimp connection used to connect the printed array to the scanner.

The proof-of-concept array used for comparison is an 8-channel array, fabricated using DuPont 5064H and a PEEK substrate. Other substrates such as PTFE, PEI, and PI-F show better coil performance, but lack mechanical and environmental stability preventing their use in arrays that are suitable and safe for human imaging without additional steps. Specifically, PTFE had poor film adhesion that caused cracks to occur at any printed/non-printed interface that existed between the coil substrate and the cables used for the connection. Coils made from PEI and PI-F absorbed enough moisture from the air to significantly change tuning over time.

4.3.1 Phantom Image SNR

To clearly compare the SNR between conventional and printed coil arrays, both arrays are first used to image a homogeneous conductive phantom. Figure 4.10 A shows

how each array was position on the 3.8 L cylindrical loading phantom doped with 4.5 g/L NaCl and 2.9 g/L of $NiCl_2*6H_2O$. The phantom has 6 mm thick acrylic walls containing the loading solution. An SNR map is obtained by first computing the noise covariance matrices from noise images obtained using no excitation power or gradients. This data is then used in a Roemer optimal combination, i.e., SENSE with no acceleration factor [15, 17]. For this analysis, coil sensitivity maps are estimated with ESPIRiT [21]. The noise correlation coefficient (ρ_{cc}) matrix is calculated from noise images (η) from each coil channel (γ) obtained using no RF power or gradients and computed using equation 4.7 from Duensing et al. [22].

$$\rho_{cc} = \frac{\langle \eta_\gamma \eta_{\gamma'} \rangle}{\langle \eta_\gamma^2 \rangle \langle \eta_{\gamma'}^2 \rangle} \qquad (4.7)$$

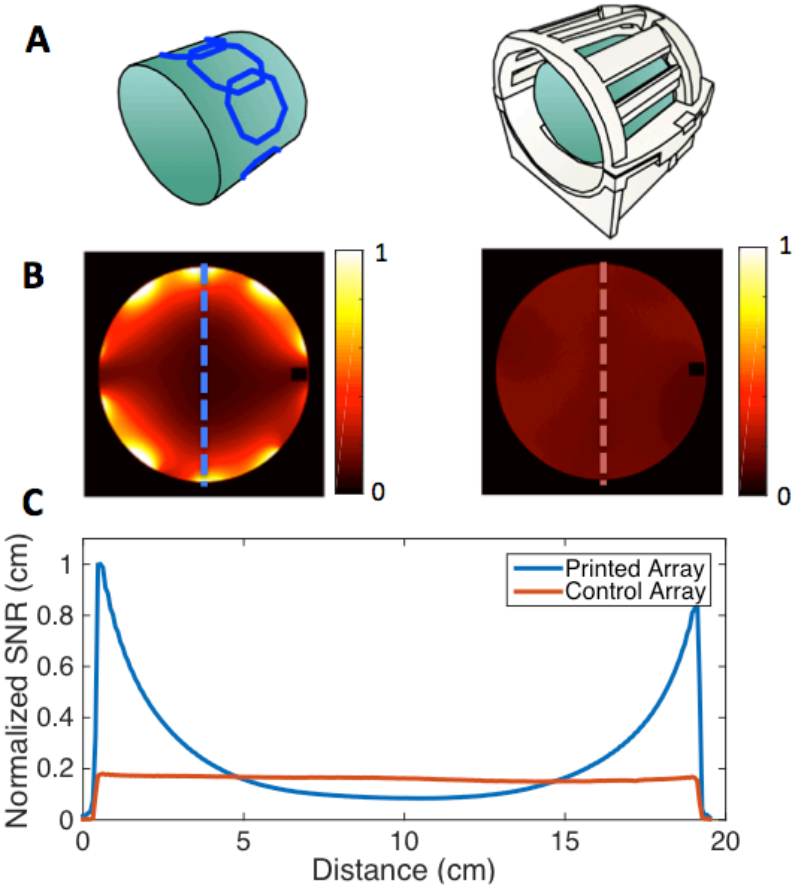

Figure 4.10: **A.** Illustration of a cylindrical conductive phantom (green) showing the placement of (top) 8-channel printed array and (bottom) a commercially available 12-channel head array. **B.** SNR maps of the phantom using (top) printed coil array and (bottom) commercial array. Blue and red dotted lines highlight the location of SNR cross-sections **C**. Centerline of SNR normalized to the maximum SNR obtained with the printed array. The printed array shows higher SNR near the surface and slightly lower in the center compared to the commercial array due to different element geometry and layout.

Figure 4.10 B show the SNR maps for each array. Comparing the two images, the printed coil has the highest SNR at the surface of the phantom and falls off towards the center of the phantom. Figure 4.10 C highlights the SNR trend by plotting the SNR for both the printed and commercial array along the centerline cross-section. From the SNR trends shown in Fig. 10 C, the regions near the conductive traces give 6 times higher SNR than in the commercially available array. However, near the center of the phantom, the printed array produced 49% of the SNR compared to the commercial array. The disparities in the SNR maps for the printed and control coils are most likely due to the differences in the surface area coverage, element positioning, coil layout, and preamplifier noise figure between the arrays.

The image quality is similar with both coil arrays despite the vast difference in the component quality and number of channels. While this is not a rigorous comparison between the two coil sets (e.g., coil shape, layout, and connection to scanner effected overall performance) this illustrates how close the performance of printed coils can be to conventional, commercial systems.

4.3.2 Array noise correlation on a phantom

The noise correlation coefficients for each array are characterized by noise images obtained from scans with no RF excitation. Figure 4.11 shows the noise correlation coefficients for both the printed and the control array, with the average correlation coefficient for the printed array being 0.105 and the control array 0.041. Coil overlap coupling capacitance is measured to be 21.4 pF. The isolation ($|S_{12}|$) between adjacent coil elements is measured to be 17.2±2.7 dB with a non-adjacent next nearest neighbor value of 20.4±2.3 dB.

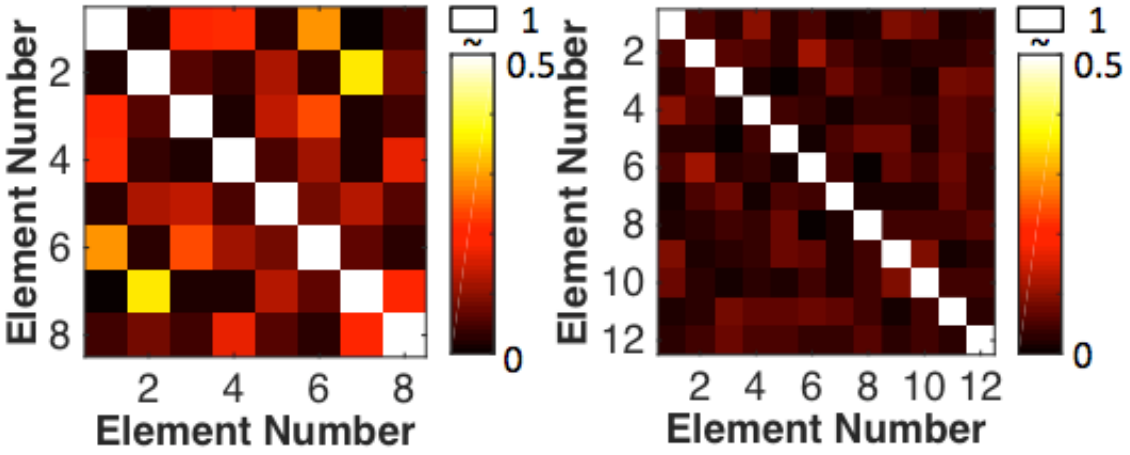

Figure 4.11: Noise correlation coefficient matrix for (left) printed array and (right) commercial array from images without RF excitation. The average off-diagonal coefficient for the printed matrix is 0.105 (min: 0.007 and max: 0.357) while the commercial array is 0.041 (min: 0.002 and max: 0.113).

While the printed array displays higher noise correlation than the control array in Fig 4.11, the magnitude of correlation is comparable to the literature on 3 T surface coil

arrays [23-25]. The higher correlation coefficient is attributed to the close proximity to the sample in addition to the relatively large mutual capacitance between the channels. We have identified other pathways for improvement of printed arrays, such as better cable management, optimized coil placement, and additional input baluns. Such optimizations would produce lower noise correlation numbers, but they are beyond the scope of the work that is presented here.

4.3.3 Volunteer Imaging

To further illustrate the performance of the printed coil array, the head of a volunteer is imaged with both a printed array and a production array. Figure 4.12 A shows a picture of the 8-channel printed array and how it is wrapped around the head of a volunteer during imaging. A 3D ultrafast gradient echo sequence is used with 1.1 mm cubic voxels. Readout and encode times were 1900 ms and 2.51 ms respectively. A 9^{o} flip angle is used with 246 phase and frequency encodes and no averaging. A foam matt 3 mm thick is placed in between coil and skin to reduce capacitive coupling. Human experiments were performed with approval of the Internal Review Board at the University of California, Berkeley.

Figure 4.12 B shows brain images taken with the printed 8-channel array and the 12-channel commercial array. As is seen, the images produced from each array are similar in quality, with SNR trends in agreement with the ones shown previously on the phantom in Fig. 4.10 B.

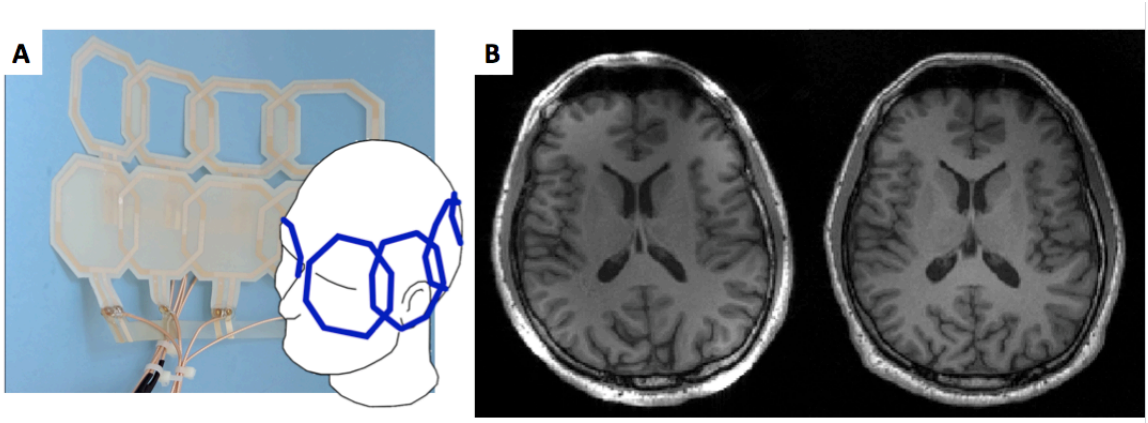

Figure 4.12: **A.** Photograph of two printed 4-channel arrays combined to make an 8-channel array and placement on a volunteer. **B.** Axial slice of a volunteers' brain using (left) the printed coil array and (right) the commercially available 12-channel head array. Similar to phantom images, printed coil shows higher SNR near surface of the brain and slightly lower in the center compared to commercial 12-channel array.

Several other areas on the volunteer are imaged with printed arrays including the elbow and shoulder with the same parameters as before to show the capabilities of the arrays. Figures 4.13 A and B show the placement of coils used to scan the shoulder and elbow of a volunteer along with the images obtained from the scan. Like the head imaging shown in Fig. 4.12, the printed arrays provide good coverage of the area and give good image quality. One advantage highlighted by the elbow images in Fig. 4., is

that the images are acquired with the volunteers elbow bent, which is not easily done with commercially available elbow arrays. These images only display the potential capabilities of the array since they are not directly compared to current commercially available arrays. However, the high SNR and flexibility of these arrays allows the coils to be easily adapted to other applications, which are further discussed in Chapter 5.

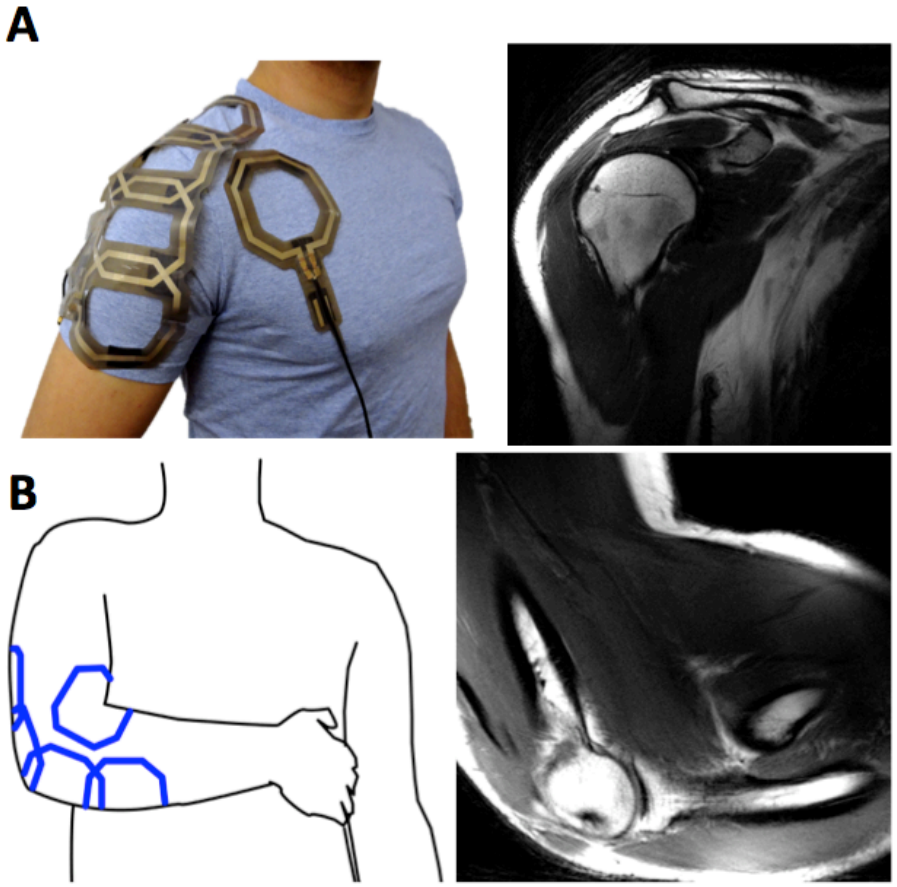

Figure 4.13: **A.** Photograph of the printed array on the shoulder of a volunteer with respective image taken with array. **B.** Illustration of coil on elbow of volunteer in bent position with respective scan from array.

4.5 Conclusions

As the materials and methods for printing continue to improve, the characterization techniques described in this chapter can serve as practical tools to enable quick identification of highly performing flexible substrates and conductors for printing MRI receive coil arrays. In this work, we demonstrated a printed coil with a SNR within 3 % of a conventionally fabricated control coil. The tests performed highlight the importance of optimizing the materials used in printed coils. Using this approach, we have shown that receive coil arrays fabricated using printing techniques are comparable to commercially available arrays, while offering new form-factors and lightweight construction.

4.6 References

[1] L. Darrasse and J. C. Ginefri, "Perspectives with cryogenic RF probes in biomedical MRI," *Biochimie,* vol. 85, pp. 915-37, 2003.

[2] B. H. Suits, A. N. Garroway, and J. B. Miller, "Surface and gradiometer coils near a conducting body: the lift-off effect," *J Magn Reson,* vol. 135, pp. 373-9, 1998.

[3] M. Rudin, *In-Vivo Magnetic Resonance Spectroscopy I: Probeheads and Radiofrequency Pulses Spectrum Analysis*. Berlin, Heidelberg: Springer Berlin Heidelberg, 1992.

[4] C. E. Hayes and L. Axel, "Noise Performance of Surface Coils for Magnetic-Resonance Imaging at 1.5-T," *Medical Physics,* vol. 12, pp. 604-607, 1985.

[5] F. D. Doty, "Solid State NMR Probe Design," in *Encyclopedia of Magnetic Resosnance*, ed: John Wiley & Sons, Ltd., 2007.

[6] J. R. Corea, A. M. Flynn, B. Lechene, G. Scott, G. D. Reed, P. J. Shin*, et al.*, "Screen-printed flexible MRI receive coils," *Nat Commun,* vol. 7, p. 10839, 2016.

[7] J. R. Corea, P. B. Lechene, M. Lustig, and A. C. Arias, "Materials and Methods for Higher Performance Screen-Printed Flexible MRI Receive Coils," *Magn Reson Med,* Sep 9 2016.

[8] F. C. Krebs, "Fabrication and processing of polymer solar cells: A review of printing and coating techniques," *Solar Energy Materials and Solar Cells,* vol. 93, pp. 394-412, 2009.

[9] D. Mager, A. Peter, L. D. Tin, E. Fischer, P. J. Smith, J. Hennig*, et al.*, "An MRI receiver coil produced by inkjet printing directly on to a flexible substrate," *IEEE Trans Med Imaging,* vol. 29, pp. 482-7, 2010.

[10] R. A. G. Horch, J.C., "3D-Printed RF Coils for solution-state NMR: Towards low-cost, high-throughput arrays," in *ISMRM 2015*, Toronto Canada, 2015.

[11] W. A. Edelstein, G. H. Glover, C. J. Hardy, and R. W. Redington, "The intrinsic signal-to-noise ratio in NMR imaging," *Magn Reson Med,* vol. 3, pp. 604-18, Aug 1986.

[12] P. Mansfield and P. G. Morris, *NMR imaging in biomedicine*. New York: Academic Press, 1982.

[13] D. M. Pozar, *Microwave engineering*, 3rd ed. Hoboken, NJ: J. Wiley, 2005.

[14] J. T. Vaughan and J. R. Griffiths, *RF coils for MRI*. Chichester, West Sussex: John Wiley and Sons Ltd., 2012.

[15] K. P. Pruessmann, M. Weiger, M. B. Scheidegger, and P. Boesiger, "SENSE: sensitivity encoding for fast MRI," *Magn Reson Med,* vol. 42, pp. 952-62, 1999.

[16] M. N. O. Sadiku, *Elements of electromagnetics*, 5th ed. New York: Oxford University Press, 2011.

[17] P. B. Roemer, W. A. Edelstein, C. E. Hayes, S. P. Souza, and O. M. Mueller, "The NMR phased array," *Magn Reson Med,* vol. 16, pp. 192-225, 1990.

[18] S. M. Wright and L. L. Wald, "Theory and application of array coils in MR spectroscopy," *NMR Biomed,* vol. 10, pp. 394-410, Dec 1997.

[19] B. Keil and L. L. Wald, "Massively parallel MRI detector arrays," *J Magn Reson,* vol. 229, pp. 75-89, Apr 2013.

[20] J. l. Mispelter, M. Lupu, and A. Briguet, *NMR probeheads for biophysical and biomedical experiments : Theoretical principles & practical guidelines*. London: Imperial College Press, Distributed by World Scientific, 2006.

[21] M. Uecker, P. Lai, M. J. Murphy, P. Virtue, M. Elad, J. M. Pauly*, et al.*, "ESPIRiT--an eigenvalue approach to autocalibrating parallel MRI: where SENSE meets GRAPPA," *Magn Reson Med,* vol. 71, pp. 990-1001, Mar 2014.

[22] G. R. Duensing, H. R. Brooker, and J. R. Fitzsimmons, "Maximizing signal-to-noise ratio in the presence of coil coupling," *J Magn Reson B,* vol. 111, pp. 230-5, Jun 1996.

[23] B. Keil, J. N. Blau, S. Biber, P. Hoecht, V. Tountcheva, K. Setsompop*, et al.*, "A 64-channel 3T array coil for accelerated brain MRI," *Magn Reson Med,* vol. 70, pp. 248-58, Jul 2013.

[24] J. A. Nordmeyer-Massner, N. De Zanche, and K. P. Pruessmann, "Stretchable coil arrays: application to knee imaging under varying flexion angles," *Magn Reson Med,* vol. 67, pp. 872-9, Mar 2012.

[25] G. C. Wiggins, C. Triantafyllou, A. Potthast, A. Reykowski, M. Nittka, and L. L. Wald, "32-channel 3 Tesla receive-only phased-array head coil with soccer-ball element geometry," *Magn Reson Med,* vol. 56, pp. 216-23, Jul 2006.

Chapter 5

5. Coils for MR Guided High Intensity Focused Ultrasound

5.1 Introduction

Magnetic resonance guided high intensity focused ultrasound (MRgHIFU) is a minimally invasive technique that can selectively heat deep-lying tissue [1-3]. This heating process uses acoustic energy to ablate tissue, activate heat sensitive medication, selectively open the blood brain barrier, or stimulate specific nerves [1-6]. The heating is tracked (i.e., guided) by changes in tissue from images taken with an MRI scanner [2]. This technique has been successfully used to treat uterine fibroids [3, 7] and soft tissue tumors[8]. It can also substantially reduce the pain from bone cancer metastasis [9], and shaking from essential tremor [10]. While traditional surgery, radiosurgery, or deep brain stimulation are available to treat these conditions [11], MRgHIFU offers similar or better outcomes without the major complications that can arise from exposing the patient to high doses of radiation or relying on an invasive surgery [3, 7, 9, 10].

In MRgHIFU therapy, water is used to transfer ultrasonic energy from an acoustic transducer to the patient. Figure 5.1 A illustrates how ultrasonic energy is focused through water and tissue to an ellipsoidal point deep inside tissue. The size of the focal point depends on the geometry of the transducer, but a typical spot size is approximately 500 μm in diameter and 2 mm long. This small focal point locally raises the temperature without damaging the surrounding tissue. MR images can accurately estimate the amount of heating that occurs by comparing the phase difference between images before and during heating [2]. From this heat map, doctors are able to accurately plan therapy and move the focal point to the desired treatment area [12].

In order to obtain images with high resolution and accurate temperature estimation, it is necessary for the image to have a high signal to noise ratio (SNR) [2]. As discussed in the previous chapters, high SNR images are acquired using surface coil arrays that are in close contact with the patient [13, 14]. However, to heat a volume larger than the focal point, the transducer is moved around the patient while changing the focus of the transducer, which would pass acoustic energy directly through different parts of a tightly fitting surface coil [15]. Figure 5.1 B shows how ultrasonic energy easily scatters and attenuates in the thick fiberglass reinforced boards, copper conductors, solder, and porcelain capacitors commonly used in surface coil fabrication. The loss from the surface coil components is significant due to their thickness and the large difference in acoustic impedance compared to water [16]. As a result, large volume coils or non-fitting surface coils that are positioned out of the way of the beam are used to image during therapy. These non-fitting coils offer low SNR and are usually unable to take advantage of image acceleration techniques such as parallel imaging that would decrease the time it takes to acquire an image [17]. This significantly degrades the temporal and spatial resolution of the temperature estimation and leads to low quality temperature maps to plan and monitor treatment. Additionally, the anatomy images used to plan surgery lack the resolution needed to see critical features such as nerves. The coils with low SNR also prevent the acquisition of diffusion-weighted images for in-situ monitoring of tissue changes that

could be used to track tissue necrosis [18, 19]. To illustrate this point, examples of a low SNR image taken with a body coil and a high SNR image from a surface coil array are shown in Figure 5.1 C. As Fig. 5.1 C shows, the noise is higher (i.e., the image has more grain) in the image taken with the body coil compared to that acquired with the surface array.

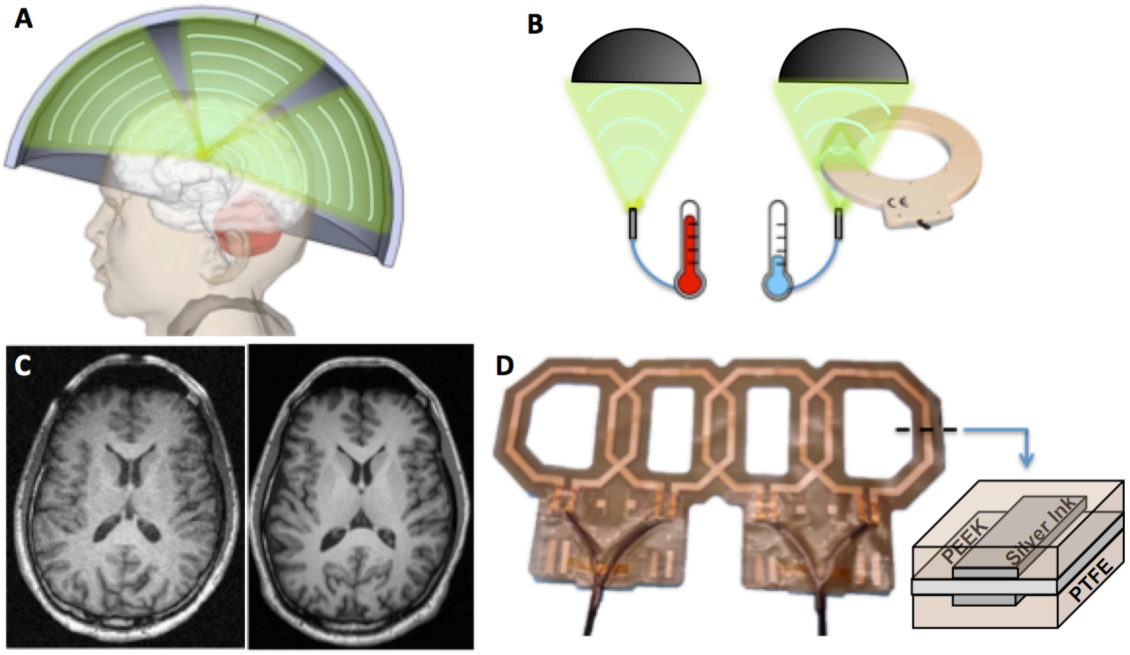

Figure 5.1: **A.** Illustration of patient positioned inside a brain transducer. Ultrasonic energy (green) is passed through water to heat tissue. **B.** Illustration of acoustic energy (green) focusing onto thermal probe producing heat with and without a surface coil present. **C.** Axial MRI scan of human brain using high noise body coil (left) and higher SNR surface coil (right). **D.** Photograph of thin surface array fabricated layer-by-layer using screen printing. Inset shows the cross section of the array detailing the materials used for construction.

In previous works, it has been reported that higher SNR in MRgHIFU is achieved by introducing novel receive coils [20-22]. However, these works have focused on the implementation of existing materials, positioning materials out of the way of the transducer elements to avoid acoustic scattering from coil components. Another way to increase SNR is to implementing a thin dipole antenna that does not significantly impact acoustic attenuation [23]. However, these practical approaches add considerable constrains to the design and implementation of the coil array. Other techniques that do not rely on close proximity of the probe, such as traveling-wave MRI [24], would not be appropriate due to the conductive materials used in the transducer and poor performance in clinical scanners.

To fully take advantage of the high SNR of surface arrays, one that is transparent to acoustic energy is needed. One way to fabricate an acoustically transparent coil is to use very thin materials with acoustic impedances values close to the value of water, such as those found in polymer-based materials and solution processed conductors. We have

shown in previous chapters that it is possible to create such coils with screen-printed conductive inks on thin plastic substrates [25, 26]. Figure 5.1 D shows an example of a surface array made in this way highlighting how the conductive traces sandwich the plastic substrate to form very thin capacitors.

For a coil to be useful in a clinical therapy, it must display high SNR and acoustic transparency. Furthermore, the coil must be able to withstand exposure to water for the length of the procedure. It is common for MRgHIFU treatments to last 3 hours or more [27] therefore to meet this requirement, the coils need to be fabricated with materials that do not suffer property changes over time when submerged. If the materials used in coil construction are affected by water, the coil function can be significantly compromised as the conductor or dielectric degrade.

This chapter covers the physics, design, and fabrication of coils that are acoustically transparent for use in MRgHIFU. First, a brief introduction to acoustic waves and MR thermometry are discussed. Next, material dependent properties such as water absorption, coil quality, and printing compatibility of several potential substrates are evaluated. Then, optimal thickness for acoustic transparency is characterized by passing 650 kHz and 1 MHz acoustic energy though different thicknesses of flexible substrates and solution processed ink in a water bath. Several waterproof coatings are tested in terms of their ability to insulate the coil from the surrounding water and are characterized for their acoustic attenuation. Once an optimized material combination is found, several receive coil arrays are fabricated for use in a 3T scanner fitted with either a table or head MRgHIFU transducer to characterize their image SNR and acoustic attenuation. Abdominal images of a volunteer on a fibroid system are obtained without heating to illustrate the improvement in image quality. Finally to show a system level proof of concept, we tracked the heating of a bovine brain tissue inside an acrylonitrile butadiene styrene (ABS) printed skull with our 4-channel printed array.

5.1.1 Acoustic Wave Theory

As acoustic waves travel through matter, the speed and phase of the wave depend on the acoustic impedance of the material. In materials, the specific acoustic impedance (Z_0) in kg/(m^{2}s) can be calculated from the speed of sound in the material (c) in m/s and density (ρ) in kg/m^3 as shown in equation 5.1.

$$Z_0 = \rho * c \qquad (5.1)$$

The behavior of any wave reflecting at a changing impedance interface will depend on the difference in the acoustic impedance between the two materials. Figure 5.2 shows several examples of incident and reflected wave-packets as they move through different media and interfaces.

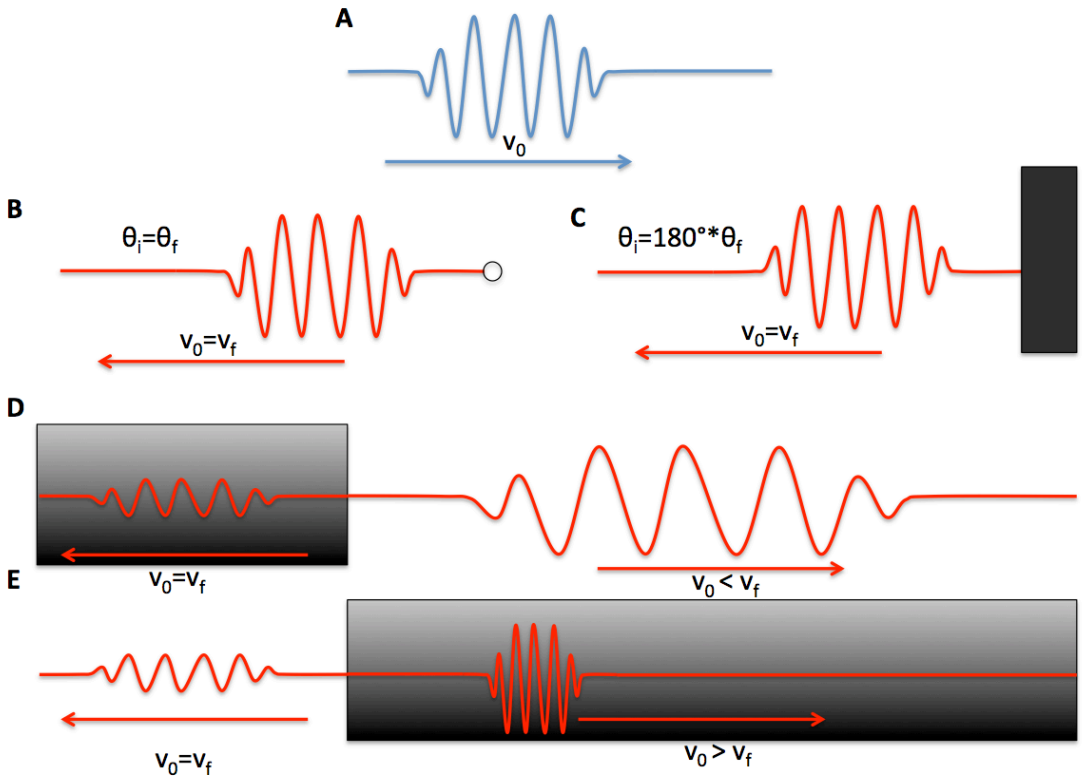

Figure 5.2: **A.** Incident wave traveling in uniform medium. **B.** Wave after it has reflected off an open-ended termination. Velocity (v) and phase (θ) are unchanged. **C.** Wave after it has reflected completely a hard boundary. Velocity is the same, but it is 180° out of phase from the initial wave. **D.** Wave reflections as it travels from high impedance to low impedance medium. Velocity of transmitted (v_f) wave is greater, but wavelength is longer. **E.** Wave reflection as it travels from low to high impedance medium. Velocity of transmitted wave is lower and wavelength is shorter.

For our experiments it is useful to predict the wave behavior of ultrasonic energy as it passed through the printed coils. If the substrate is thin compared to the focal distance of the transducer, then it is possible to model the system as a 1D wave traveling through regions of different acoustic impedance. The vast majority of power is lost due to reflections and wave effects allowing a 1D system described by the transmission line equations to predict the amount of acoustic power seen at the load. An in depth explanation of this relationship is described in Kino, et al[16], but is covered here for clarity. More complex models that take loss from attenuation in the bulk due to heat generation exist. However, the films of interest here are very thin compared to the typical attenuation constant so the 1D model is sufficient.

To calculate the amount of power dissipated in the film and load, an equivalent circuit can be used. As an example, Fig. 5.3 shows the equivalent circuit for a test film in a water bath between a hydrophone and a transducer. In this setup, acoustic energy is generated at the transducer and travels through the water and film before being received at the hydrophone.

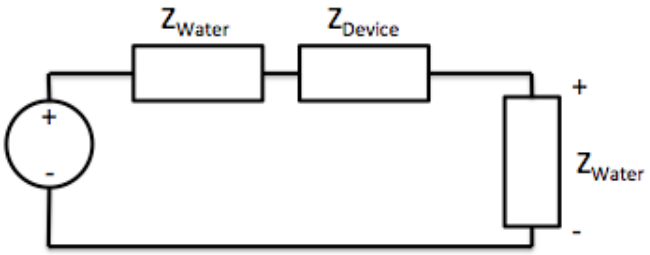

Figure 5.3: Equivalent circuit used to calculate power dissipated in load (hydrophone) from acoustic source (transducer) through test device (plastic substrates). In this model, it is assumed that both the transducer and hydrophone are perfectly matched to water.

The current through the circuit can be calculated using ohms law (equation 5.2, where the amplitude of the acoustic pressure is V) since all the impedances are known. The impedance measured across the load (Z_{in}) can be calculated using equation 5.3 where L is the thickness of the film and ω is the angular frequency.

$$I = \frac{V}{Z_{Total}} \qquad (5.2)$$

$$Z_{in}(-L) = Z_0 \frac{Z_L - i\,Z_0 \tan(kL)}{Z_0 - i\,Z_L \tan(kL)} \qquad \text{where: } k = \frac{\omega}{c_{medium}} \qquad (5.3)$$

Once the current in the circuit is known, the power dissipated in the load (P_L) can be found using equation 5.4.

$$P_L = I^2 Z_L \qquad (5.4)$$

5.1.2 MR Thermometry

There are numerous methods to track temperature changes in MRI. Differences in spin-spin relaxation time [2, 28], spin-lattice relaxation time [2], proton density [29] and diffusion coefficient [30] are all temperature dependent and could be used to track heating in an MRI, but the most common form of tracking temperature change is by the proton resonance frequency (PRF) difference.

As discussed in chapter 1, the resonance frequency of an atomic nucleus is dependent on the strength of the magnetic field that it is situated in. In clinical MRI, the source of this field is the large magnet that supplies the main field of the scanner as well as the gradient coils. In addition to the large macroscopic field, individual spins also experience the magnetic fields from nearby atoms. For hydrogen, the nuclear magnetic moments are shielded from the macroscopic magnetic field by any nearby electrons of the molecule it is bonded to. The bonds influence the resonance frequency of the hydrogen nucleus and can serve as the basis for nuclear resonance spectroscopy. The change in the frequency of precession can be modeled by the addition of a shielding coefficient (s) to the Larmor frequency equation shown in equation 5.5.

$$\omega = \gamma B_0(1 - s) \qquad (5.5)$$

As the temperature increases, the bonds a hydrogen nucleus make with other atoms bend, stretch, and break, changing the amount of screening and subsequently the resonance frequency. For the typical temperature in MRgHIFU, this phenomena varies linearly [2] and can be quantified using equation 5.6 which relates the phase images at two different times ($\phi(T)$ and $\phi(T_0)$) to temperature using the gyromagnetic ratio (γ), the PRF change coefficient (α), main field strength (B_0), and TE the echo time of the scan [2].

$$\Delta T = \frac{\phi(T) - \phi(T_0)}{\gamma \alpha B_0 TE} \qquad (5.6)$$

To acquire a temperature map, first a phase image is acquired at a baseline temperature. While the sample is heating or cooling, a second phase image is acquired. To increase the accuracy of temperature estimation, a B_0 map can be acquired to account for any main field inhomogeneity, which could decrease the accuracy of the temperature estimation.

To demonstrate this technique, a cross-sectional image of a cylindrical gel phantom is acquired before and after a warm towel is applied to the right side of the phantom. The phase images before and after are displayed in Fig. 5.4 and are used to calculate the change in temperature map shown in Fig. 5.4 C. As seen in Fig. 4.5 C the increase in temperature on the right side of the phantom matches where the warm towel was placed. The lefts side of the phantom shows a heat decrease, illustrating the heat transfer from the phantom once it was moved into the colder MR suite.

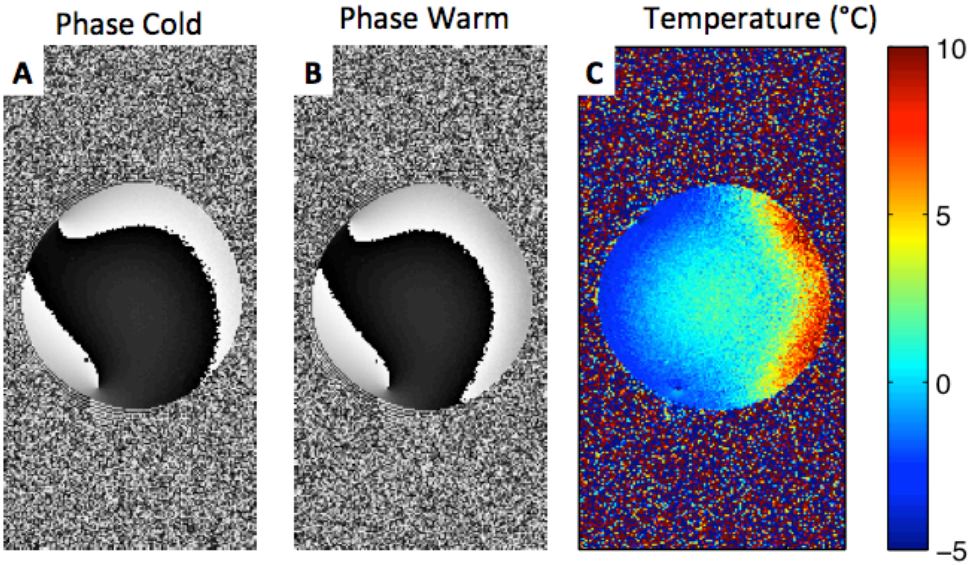

Figure 5.4: **A.** Phase map of a cylindrical gel phantom. **B.** Phase map of the cylindrical phantom after warm tower was applied to right side. **C.** Temperature map showing increase in temperature throughout the entire cross section of the phantom.

This technique can then be used to map the heating and location of a focused ultrasound beam inside tissue. Figure 5.5 illustrates this process as heating is tracked inside a cylindrical gel phantom, pictured in Fig. 5.5 A. An ultrasonic transducer, pictured in 5.5 B, passes acoustic energy through water into a phantom, as shown in 5.5 C. The resulting temperature maps shown in figure 5.5 D and E display the distribution of heat inside the phantom. Note that the heating point remains localized to a small region within the phantom. This point can then be moved around to treat different areas inside a phantom or tissue.

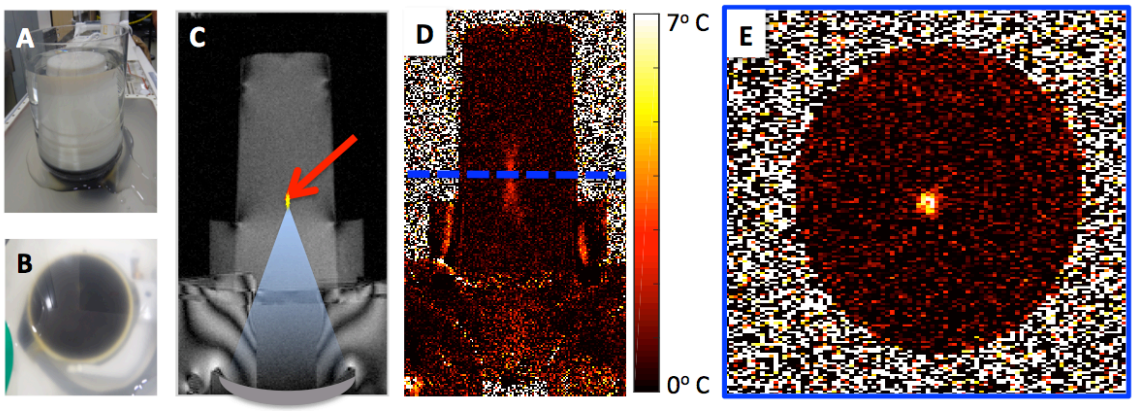

Figure 5.5: **A.** Photograph of gel phantom in water bath. **B.** Top down photograph of ultrasonic transducer. **C.** Cross-sectional magnitude image of phantom sitting on top of transducer with focal path (blue) and focal point (red arrow) highlighted. **D.** Coronal temperature map of cylindrical phantom. Blue dotted line indicates location of maximum temperature map slice shown in **E**.

5.2 Water Stability Characterization

5.2.1 Substrate Water Stability

To get high SNR during a MRgHIFU session, the entire receive coil must be submerged in water. Therefore any substrate used for coil construction must not change properties or degrade when exposed to water for long periods of time. In this study, several common substrates were selected based on their known water absorption properties, mechanical/thermal stability, and availability in thicknesses less than 150 µm. While most plastics have their water absorption properties characterized, it is uncommon to report loss data at frequencies common to MRI. Furthermore, any moisture dependence of dielectric quality is rarely captured in standard testing. To characterize materials for use in MRgHIFU coils, the substrates were placed in a copper/acrylic testing rig to simulate the final coil structure, previously described in Chapter 4 [26]. The area of the copper strips is trimmed so that the coil structure resonates at the Larmor frequency of our 3T scanner (123.3 MHz). To quantify the electrical performance of the material, the quality factor (Q) is measured with the coil at least 50 cm away from any conductive material ($Q_{Unloaded}$), with higher $Q_{Unloaded}$ indicating lower loss. Figure 5.6 shows how the substrates were then removed from the test rig and submerged in 20 °C deionized water for 24 hours. Then, the substrates are taken out of the water bath, wiped

dry, and immediately put in the copper/acrylic test rig again and $Q_{Unloaded}$ and center frequency are recorded. From the relative changes in $Q_{Unloaded}$ and resonant frequency, we are able to compare coil materials to determine a substrate that presents both high $Q_{Unloaded}$ and insensitivity to water.

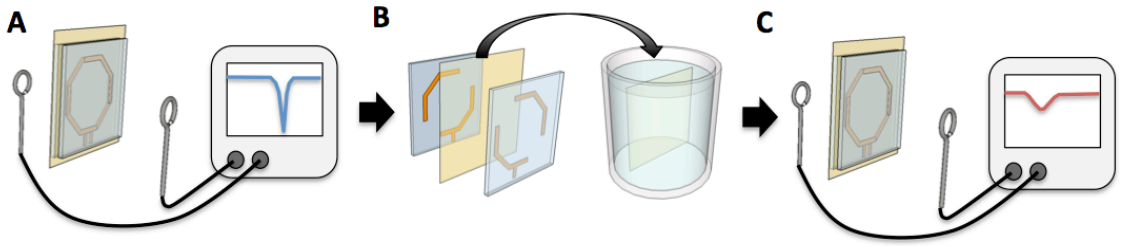

Figure 5.6: **A.** Illustration showing experimental setup during coil $Q_{Unloaded}$ measurements in the test rig. **B.** Illustration showing how substrate is immersed in water for 24 hours. **C.** Illustration showing coil changes in $Q_{Unloaded}$ and resonance frequency after water submersion.

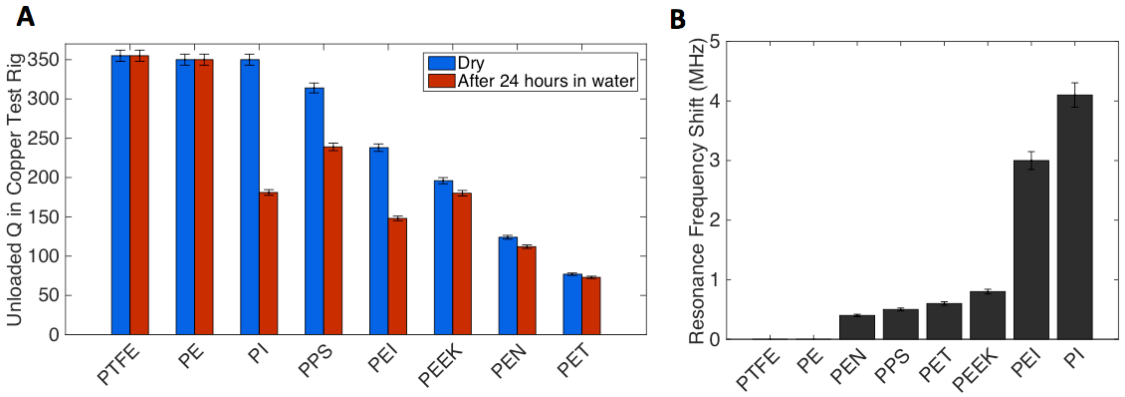

Figure 5.7: **A.** Substrate $Q_{Unloaded}$ before and after water immersion in test rig. **B.** Resonant frequency shift for substrates after 24 hours water immersion.

In this study, polytetrafluoroethylene (PTFE), polyethylene (PE), polyimide (PI), polyphenylene sulfide (PPS), polyetherimide (PEI), polyether ether ketone (PEEK), polyethylene naphthalate (PEN) and polyethylene terephthalate (PET) are evaluated. Figure 5.7 A shows how the $Q_{Unloaded}$ changed for coils made with several plastic substrates before and after submersion in water for 24 hours. Furthermore, Fig. 5.7 B shows the change in resonant frequency after submersion as the substrates absorbed water. The highest $Q_{Unloaded}$ value recorded is 350 for PTFE and the lowest is 58 for PET. While the magnitude of $Q_{Unloaded}$ is relevant, the amount of change in the coil $Q_{Unloaded}$ and the resonant frequency before and after submersion is more important. For example, PI and PEI show higher $Q_{Unloaded}$ than PEEK, but after submersion in water the resonant frequency and $Q_{Unloaded}$ significantly change. The shift in coil tuning is due to the large difference in dielectric constants between plastics ($\varepsilon_r \approx$ 2-4) and water (ε_r = 80 at 20 °C), therefore even a small amount of absorbed water has a large impact on resonant frequency. This makes tuning the coil very difficult, as any absorbed water would change

the coil tuning. Other substrates such as PE and PTFE show excellent $Q_{Unloaded}$ values and low change, but are not suitable for the printing process because our ink easily delaminates from them. Based on this characterization, PEEK is chosen as the most appropriate substrate to fabricate MRgHIFU coils with due to its high $Q_{Unloaded}$, low water absorption, and ease of printability.

It is important to note that while the barrier materials provide some protection against water impinging on the substrate and changing the electrical properties of the substrate, it does not provide complete protection. Even for the PTFE film used to encapsulate the coils (further described in section 5.3.3) water can advance into the substrates along the edges of the substrate and through the adhesive used to bond the encapsulating film to the substrate. Having a water resistant substrate is critical to reliable coil behavior.

5.2.2 Conductor Water Stability

Dupont 5064H silver ink is chosen for the conductive portions of the coil based on its previous use in printed MRI coils described in chapter 4 [26]. To characterize the stability of the conductive traces in water, several samples ranging from 3-28 µm of Dupont 5064H are measured on a 4-point probe to determine bulk resistivity before being submerged in 20 °C deionized water for 24 hours. Then, the traces are wiped dry and re-measured on the 4-point probe to characterize any change in the conductivity. Additionally, the film surface roughness is characterized before and after water submersion on a profilometer to determine if there is any difference in film topography.

After submersion, the samples made of the Dupont 5064H silver ink did not experience a significant change in resistivity; showing resistivity of 16±2 µohm-cm before and after submersion. Furthermore, the surface roughness of the ink did not change, maintaining a root mean squared (RMS) surface roughness of 1.3±0.2 µm both times. From these results, the stability of Dupont 5064H is sufficient for use in an MRgHIFU application.

5.3 Materials Acoustic Characterization

In addition to water stability, the materials must transmit a high percentage of incident acoustic energy without distortion. Local surface burns, damage to the transducer, and low focal heating would arise if the coils reflect or attenuate a significant amount of the acoustic energy.

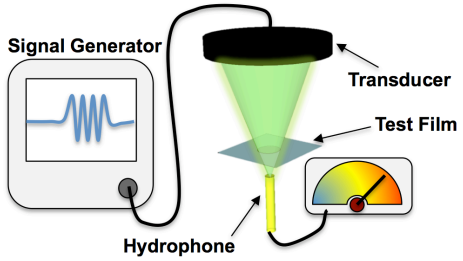

Figure 5.8: Illustration showing the substrate (blue) placement during the sonication testing. Transducer (black) is driven at different frequencies with acoustic pressure measured by a hydrophone (yellow). The transducer, substrate, and hydrophone are submerged in degassed deionized water (not pictured).

To evaluate the materials, test films are placed in a deionized water bath between an ultrasonic transducer (Olympus V303-SU) and a calibrated hydrophone (Onda HGL-0400 capsule hydrophone with AH-2020 20 dB preamplifier) placed 2.54 cm apart. Figure 5.8 illustrates how acoustic power at frequencies commonly used in MRgHIFU – 650 kHz for a head transducer system and 1 MHz for a fibroid transducer system – are transmitted through the substrates and recorded by the hydrophone. The tank is sized to be sufficiently large compared to the wavelength of the acoustic energy (45x30x30 cm) and lined with sound attenuating foam in order to minimize reflections of sound waves off the sidewalls. All values are normalized to the acoustic pressure when no obstruction is present. The acoustic measurements are averaged 2048 times to reduce noise. Each trial is repeated 3 times to further reduce the measurement error. The experimental setup was characterized to have a relative error of 5% by measuring the relative intensity of the focal spot by the hydrophone with no obstruction several times over several different measurement sessions.

5.3.1 Substrate Acoustic Properties

The acoustic absorption of PEEK is characterized since it presents the best combination of high $Q_{Unloaded}$, low sensitivity to water, and adequate printing characteristics. Several PEEK substrates with thicknesses of 50 μm to 254 μm are tested to determine the optimal thickness in the setup previously described. In our analysis, the absolute magnitude of the acoustic pressure is not known, therefore all the measurements, including those predicted in the model, are normalized to the pressure seen by the hydrophone when no film is present. The speed of sound, density, and acoustic impedance values used in our model are shown in table 5.1 [31-34].

Table 5.1: Values used in acoustic impedance analysis

Material	Density (kg/m^3)	Speed of Sound (m/s)	Acoustic Impedance (MRayl)
PEEK [32]	1260	2536	3.16
PTFE [33]	2149	1390	2.99
Water [34]	1000	1482	1.48

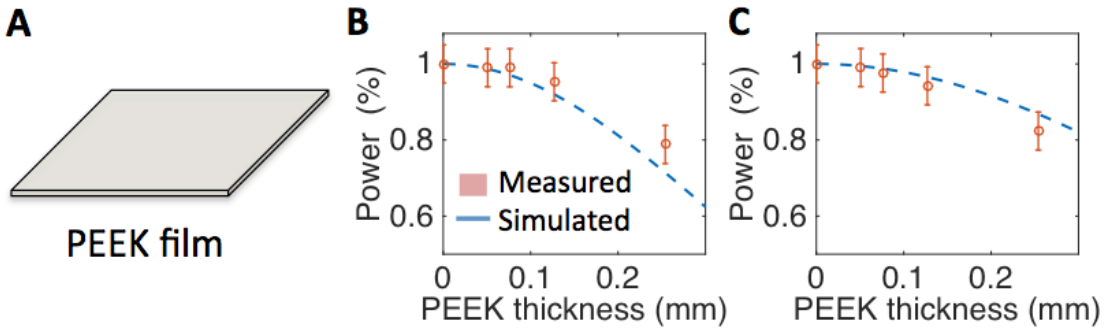

Figure 5.9: **A.** Illustration of the PEEK test film **B.** Relative acoustic power for several thicknesses of the PEEK plastic at 1 MHz and **C.** 650 kHz. Dotted blue line shows attenuation estimated by the acoustic model described in section 5.1.1 [16].

Figure 5.9 shows the relative acoustic power measured from several samples of PEEK at 650 kHz and 1 MHz. The thinnest films of PEEK provide the least amount of attenuation; however, thinner films are more difficult to process. As a result, we chose a PEEK film thickness of 76 µm to maintain acoustic transparency, handling robustness, and ease of processing.

5.3.2 Printed Conductor Acoustic Properties

The acoustic properties for solution-processed materials are not commonly available. Several thickness of silver ink ranging from 3-28 µm thick are screen printed on the previously characterized 76 µm thick PEEK substrates to characterize the acoustic properties of the silver ink. Films thicker than 28 µm are difficult to produce with the screen printer so a blade coater is used to print 17, 24, 38, and 56 µm thick films. Films thicker than 56 µm are extremely non-uniform, showing large deviations in thickness across the film and are not characterized. After deposition, the test films are placed in the water bath between the hydrophone and transducer as previously described to record the transmission of acoustic power at 650 kHz and 1 MHz. The power transmitted through different thicknesses of the ink are then used to make a trust-region-reflective non-linear least squares fit of an acoustic transmission line model described in section 5.1.1 from Kino [16]. The acoustic impedance of the silver ink is estimated from the fit.

Figure 5.10 A shows the substrate film stack tested in the water bath with the transmitted acoustic power at 650 kHz and 1 Mhz. Figures 5.10 B and C show that there is little deviation between the measured and predicted transmitted power, suggesting that the printed silver films are attenuating acoustic energy mainly by transmission and reflection interactions rather than diffuse scattering or bulk attenuation. Low losses from scattering are expected since the surface roughness measurements show a roughness value (1.3±0.2 µm) that is much lower than the wavelength of the acoustic energy (1.48-2.28 mm).

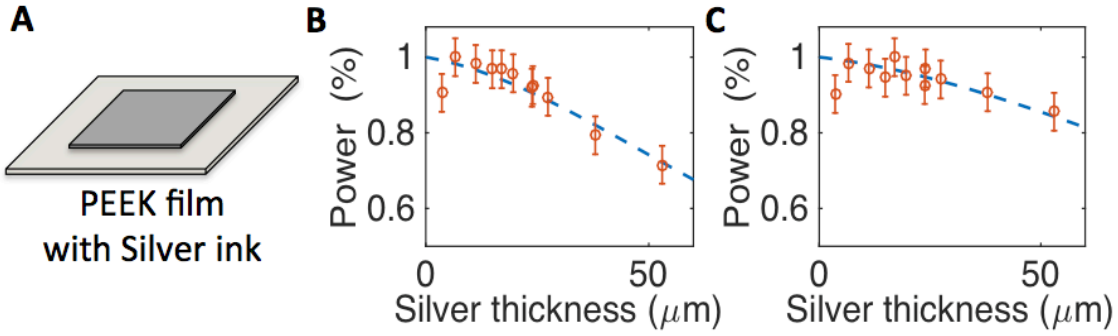

Figure 5.10: **A.** Illustration of the film stack characterized by the acoustic testing. Relative acoustic power for several thicknesses of Dupont 5064H silver ink on 76 µm thick PEEK plastic at **B** 1 MHz and **C** 650 kHz. Dotted blue line shows the attenuation estimated by the acoustic model described in section 5.1.1 [16].

Based on the model fit, we found that the Dupont 5064H silver ink has an acoustic impedance of 15.6±3.8 MRayls. This value is closer to that of water at 1.5 MRayls, when compared to commonly used copper at 44.6 MRayls or bulk silver at 38.0 MRayls. This decreased acoustic impedance can be attributed to the composition of the ink, which is made of a mixture of silver micro-flakes and polymer based binders. The silver microflakes in the ink have an acoustic impedance similar to bulk silver while the polymer binders have a lower acoustic impedance, similar to most plastics. Combining the two gives acoustic properties somewhere between the two constituent materials, like those shown in our measurement. The decreased acoustic impedance allows reduced reflections at any water, tissue, or plastic interface compared to commonly used conductors.

Overall the acoustic properties of the silver ink made it well suited for use in acoustically transparent coils.

5.3.3 Encapsulation Acoustic Properties

While the conductor and substrate materials have shown to be water tolerant, the coils need to be encapsulated in an insulating barrier material to prevent electrical contact with the water and patient. To this end, several different encapsulation layers are also characterized for acoustic transmission. These included commercially available adhesive backed films, spray on coatings, dipped coatings, and epoxy-based resins. These films are applied to one side of a 76 μm thick sheet of PEEK substrate and then characterized for acoustic transmission as previously described.

To protect the patient from any DC bias that might exist on the coil, the electrical isolation of each encapsulation is tested by applying it over a conductive printed trace of Dupont 5064H on 76μm PEEK substrate. Then the samples are then submerged in a 1 molar solution of salt water that is biased to 10,000V. If any current through the film is observed, then the film is not suitable to protect the patient from the DC electrical contact to the coil and is not used.

Table 5.2: Acoustic, breakdown, and adhesion data for various encapsulation methods.

Encapsulation	Thickness	Acoustic Transmission (Pressure)	10,000V breakdown test	Tape test
PTFE film	76 um	97.8 %	Pass	Pass
Epo-Tek Flexible Epoxy	100 um	94.2 %	Fail	Pass
FEP film	90 um	94.0 %	Pass	Pass
Polyimide film	50 um	93.7 %	Fail*	Pass
PMMA Paint	10 um	91.9 %	Fail	Fail
PMMA Sealer	10 um	91.7 %	Fail	Fail
Rubberized coating	50 um	91.6 %	Fail	Pass
PET film	50 um	87.3 %	Pass	Pass
PEEK film	50 um	82.3 %	Pass	Pass
PTFE film	125 um	77.5 %	Pass	Pass

*adhesive failed

To characterize how well the barrier films adhered to the surface of the PEEK, a piece of tape is pressed in contact with the film and then quickly removed. If any of the barrier

material delaminated from the substrate the test film it was not used in coil construction. A summary of the acoustic, electrical breakdown testing, and adhesion testing are shown in Table 5.2.

Based on the initial absorption data shown in table 5.2, we found that a 76 µm film of PTFE with an acrylic adhesive is able to easily stop water transmission and adhere to our coil without delaminating, while passing the highest amount (97.8%) of the initial acoustic pressure. This substrate provided high breakdown strength, easily holding the 10,000V DC bias placed across it. This film provides excellent mechanical and electrical encapsulation that could be further optimized.

To further characterize and optimize the performance of the PTFE film, test films with 75, 127, 391, and 520 µm in thickness of PTFE were measured for transmission across a span of common MRgHIFU frequencies. The same water bath setup shown previously in Fig. 5.8 is used sweeping acoustic power from 600 kHz to 1.4 MHz in steps of 5 kHz.

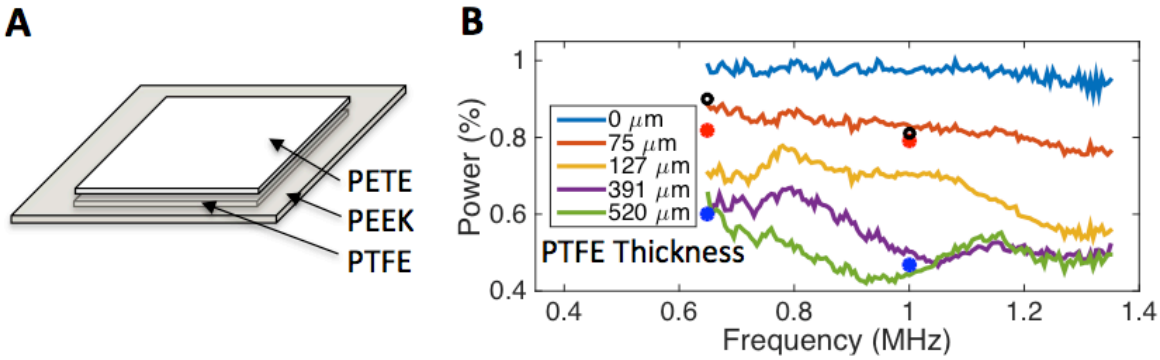

Figure 5.11: **A.** Illustration of the encapsulation stack characterized in the acoustic testing. **B.** Relative acoustic power transmitted through several thicknesses of PTFE encapsulation on both sides of 76 µm thick PEEK plastic. Black dots show relative intensity of capacitor with encapsulation. Red dots indicate transmission of capacitor made from 9 um of copper on 50 um of polyimide. Blue dots indicate transmission of capacitor made from 35 um of copper on 50 um of polyimide.

Figure 5.11 shows the amount of power transmitted through the PTFE/PEEK/PTFE test film over a span of frequencies. The highest transmission across all frequencies is given by 76 µm of PTFE film on both sides of the 76 µm PEEK substrate. As a result, this stack is used for coil construction.

Of particular interest is the higher attenuation indicated by the 391 µm and 520 µm films. These thicknesses were chosen to try to obtain a quarter-wavelength matching layer to increase the transmission at 650 KHz and 1 MHz respectively. While these films seem to pass more energy near their intended frequencies, the attenuation of the bulk is high enough to counteract any gain from this type of matching layer. More optimization and evaluation of materials could be done to make a matching layer like this work, but it is beyond the scope of the work presented here.

5.3.4 Test Device Acoustic Properties

The optimal material stack for electrical isolation and minimal acoustic attenuation is found to be 15 µm of printed silver on both sides of a 76 µm thick PEEK substrate encapsulated in 76 µm of PTFE film. A test capacitor is fabricated with this combination and used to compare the attenuation to traditionally used porcelain capacitors (ATC series B) on 35 µm copper coated 1 mm thick fiberglass board. To create a 2D map of transmitted power to characterize attenuation or scattering, the hydrophone is scanned over a 20x20 mm area. In order to compare it with the traditionally used coil materials, a 3.2 mm thick piece of acrylic sheeting is characterized to show the attenuation that could occur from typical array packaging.

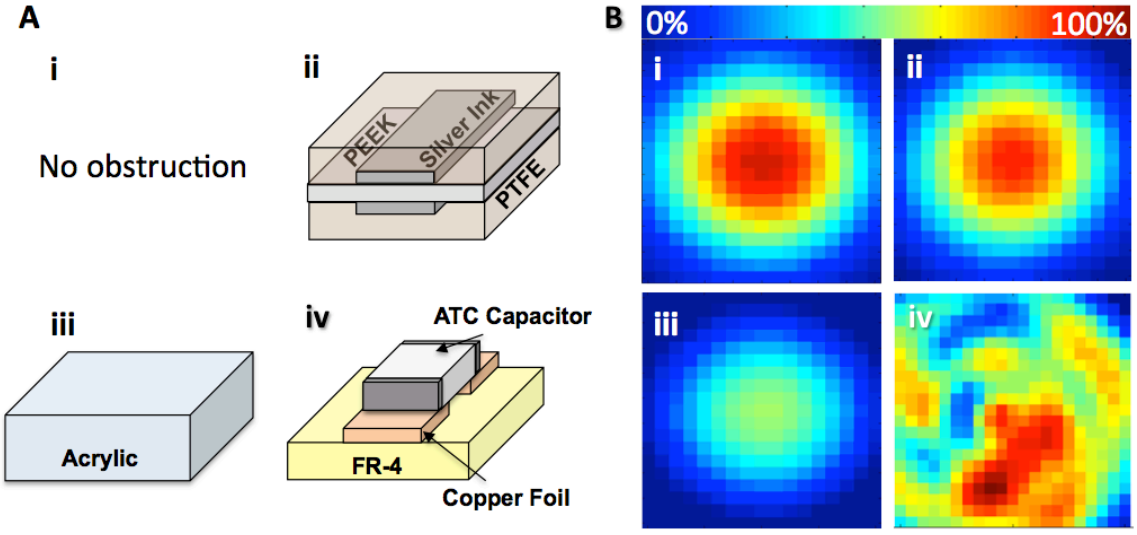

Figure 5.12: **A.** Illustrations of (i) no obstruction, (ii) printed coil capacitor in beam path, (iii) 2 mm acrylic plastic, and (iv) traditionally used porcelain tuning capacitor in beam path tested for attenuation and scattering **B.** 2D acoustic profiles for transducer focal point over 4x4 mm area showing relative intensity with (i) no obstruction, (ii) printed coil capacitor in beam path, (iii) 2 mm acrylic plastic, and (iv) traditionally used porcelain tuning capacitor in beam path.

Figure 5.12 shows the acoustic power transmission profiles for our printed capacitor in addition to traditionally used materials. From these scans, we did not notice any significant distortion or scattering in the focal spot for the printed capacitor. The printed capacitor transmitted 80.5% of the acoustic power at 1 MHz and 89.5% at 650kHz, in agreement with previous testing. These transmissions are much higher compared with the 51.4% and 62.5% obtained with the 2 mm thick acrylic. The beam shape is also preserved for both the acrylic and printed capacitors, but is significantly scattered for the traditionally used porcelain capacitor on copper clad fiberglass reinforced circuit board.

To provide a comparison to a non-printed approach, two commonly available thin copper clad substrates were also evaluated by our hydrophone setup. Commercially available 9 µm copper on top of 50 µm polyimde (Pyralux AP 7156E) and 35 µm copper on top of 50 µm polyimde (Pyralux AP 9121R) were both encapsulated in 76 µm of

PTFE and characterized to compare to our printed coil. The transmitted acoustic power for these the films is shown in Fig. 5.13. This figure shows that while the thinner version of Pyralux with copper comes close to the printed coil, the printed coil still outperforms at both 650 kHz and 1 MHz.

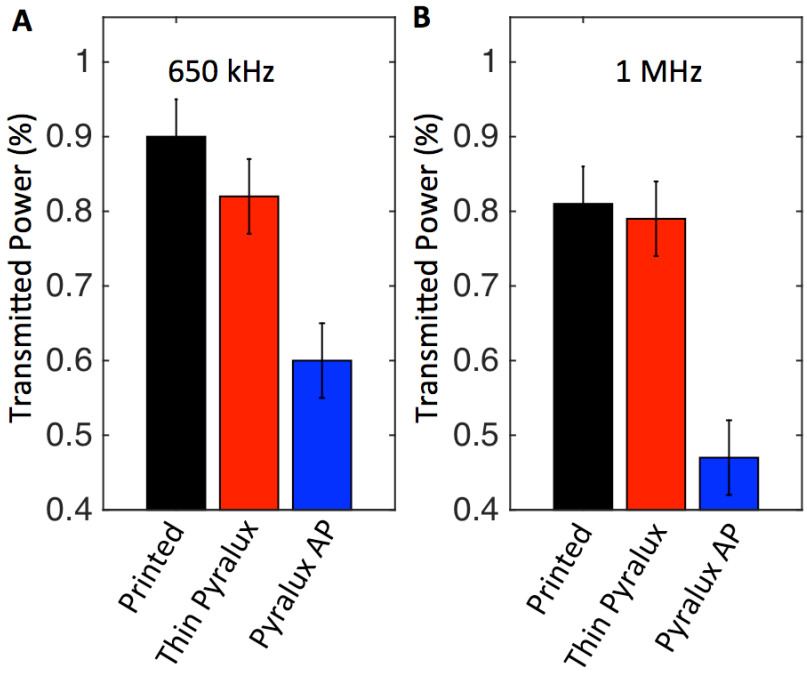

Figure 5.13: Acoustic transmission for printed coil structure (black) Pyralux AP 9121R (red) Pyralux AP 7156E (blue) at **A** 650 kHz and **B** 1 MHz. All materials were encapsulated in 76 μm of PTFE on both sides.

In addition to providing poorer acoustic transmission, the pyralux substrates are made of materials that are sensitive to water. The copper conductors easily corrode and break down if left in water for extended periods of time. Additionally, the substrate used in pyralux is similar to the polyimide (PI) materials that we tested in section 5.2.1, and readily absorb water changing the electrical tuning of any coil made of it. As it is shown in previous sections, the printed materials do not suffer from such problems and are uniquely suited for MRgHIFU coils.

5.4 Coil Array SNR Characterization

5.4.1 Phantom Imaging

A water resistant 4-channel array is fabricated using 76 μm of PEEK (polyether ether ketone) film encapsulated in 76 μm PTFE (polytetrafluoroethylene) film with 20 μm Dupont 5064H conductive ink using the method described in chapter 4 [26]. The SNR of our array is compared to the SNR of the traditionally used body coil of a 3T scanner (General Electric 3T Discovery MR750) on a gel phantom inside the head transducer

(Insightec Exablate 4000). An ultra fast gradient echo scan with flip angle of 30°, echo time of 12.7 ms, repitition time of 25.6 ms and 1 average sequence is chosen since it is representative of a scan that is used in a temperature map for the SNR comparison. Figure 5.14 A illustrates the positioning of the printed array wrapped around the gel phantom and submerged inside the head transducer to characterize the SNR.

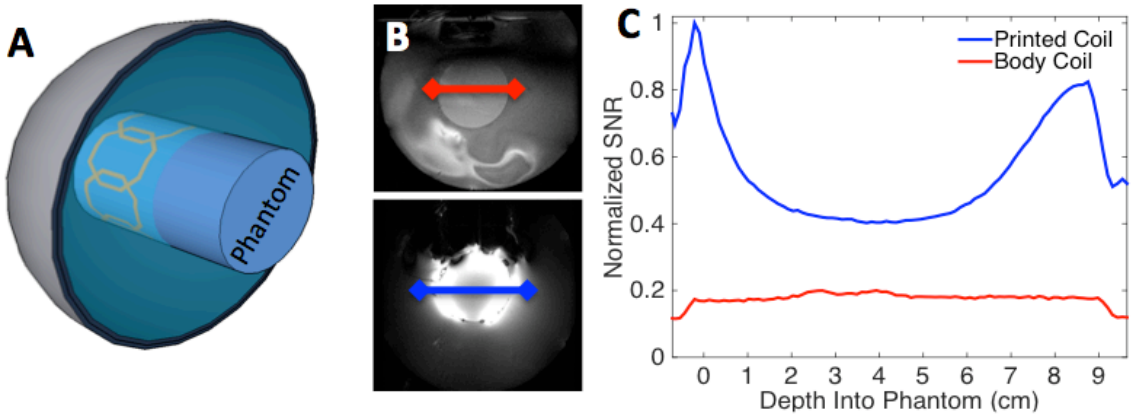

Figure 5.14: **A.** Illustration of the experimental setup. A gel phantom is placed inside the head transducer with a coil array wrapped around it. The entire transducer is filled with water. **B.** Coronal slices of phantom in head array show sensitivity profile for (top) system body coil and (bottom) 4-channel printed array. The red and blue lines highlight the location of the SNR profile. **C.** SNR for printed 4-channel surface array compared to a 3 T system body coil. Magnitude is normalized to the maximum intensity seen with the printed coil.

The SNR across the center of the phantom - highlighted in figure 5.14 B and C - shows that the array presents as 5 times the SNR at the surface of the phantom when compared to the currently used body coil. The asymmetry seen in the coil sensitivity pattern is due to the coil size and placement on the phantom. The array displayed twice the SNR than when compared to the body coil at the center of the phantom where MRgHIFU surgery is most likely to occur. The SNR in the center could be further improved by better-optimized element size and placement, but it is beyond the scope of the work presented here.

5.4.2 Volunteer Imaging

To show the clinical SNR gains that a printed coil array can provide, breath-hold abdominal images of a volunteer are acquired. Figure 5.15 A illustrates the positioning of the volunteer face down inside the scanner with an 8-channel coil array wrapped around their abdomen. A gradient echo sequence with flip angle of 20°, encode time of 4 ms, readout time of 8.6 ms, 1 average is used to acquire images with both the body coil and the printed array. Images are acquired on the same system as describe previously, but with the transducer disconnected for safety. The coil array is offset from the volunteer by 4 mm to reduce capacitive coupling. All volunteer imaging is performed with internal review board (IRB) consent.

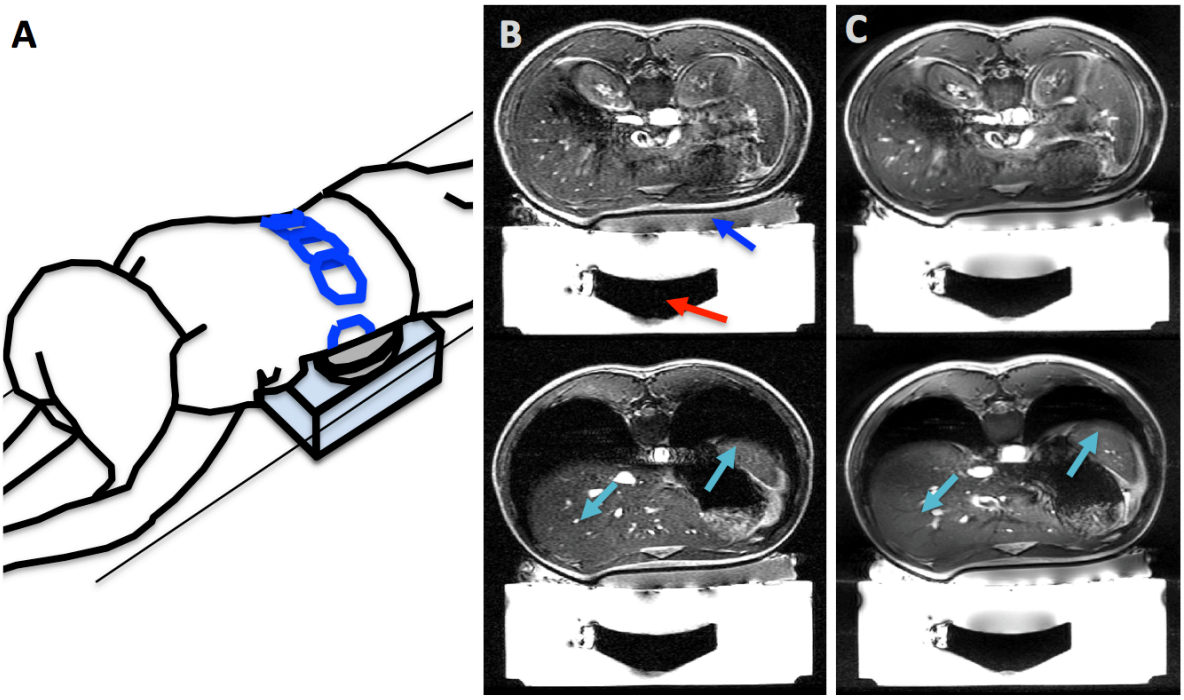

Figure 5.15: **A.** Illustration of coil array (blue) positioned on volunteer lying face down. **B.** Abdominal images of volunteer from low SNR body coil and **C.** high SNR 8-channel ultrasound transparent array. Top images are during a full exhale and bottom images are taken during a complete inhale. Blue arrow highlights acoustic matching gel pad. Red arrow highlights location of transducer in water bath. Teal arrows highlight increased resolution at inside liver and at edge of lungs. Image intensity is normalized using the body coil images for images produced with the array.

The comparison between the abdominal images from the body coil and the transparent arrays in Fig. 15B and C shows that it is possible to obtain images with more detailed liver and stomach regions when using the printed array. While there are some regions in the center of the patient with decreased SNR for the 8-channel array, these regions still contain more SNR than the body coil. This would provide more crucial detail that is extremely valuable during treatments. In addition to the observed SNR benefit, the multichannel array is also able to perform parallel imaging acceleration from the additional channels which enable faster image acquisition [17].

5.4.3 Acoustic Heat Tracking

The array and body coil are used to track the heating inside the center of a gel phantom using 60 W of acoustic power for 10 seconds at 650 KHz. This test is performed inside the head transducer system while tracking with a 3T MR scanner to demonstrate the improved heat maps produced by the array. The printed array is wrapped around the outside of the cylinder during these experiments as illustrated in figure 5.16 A.

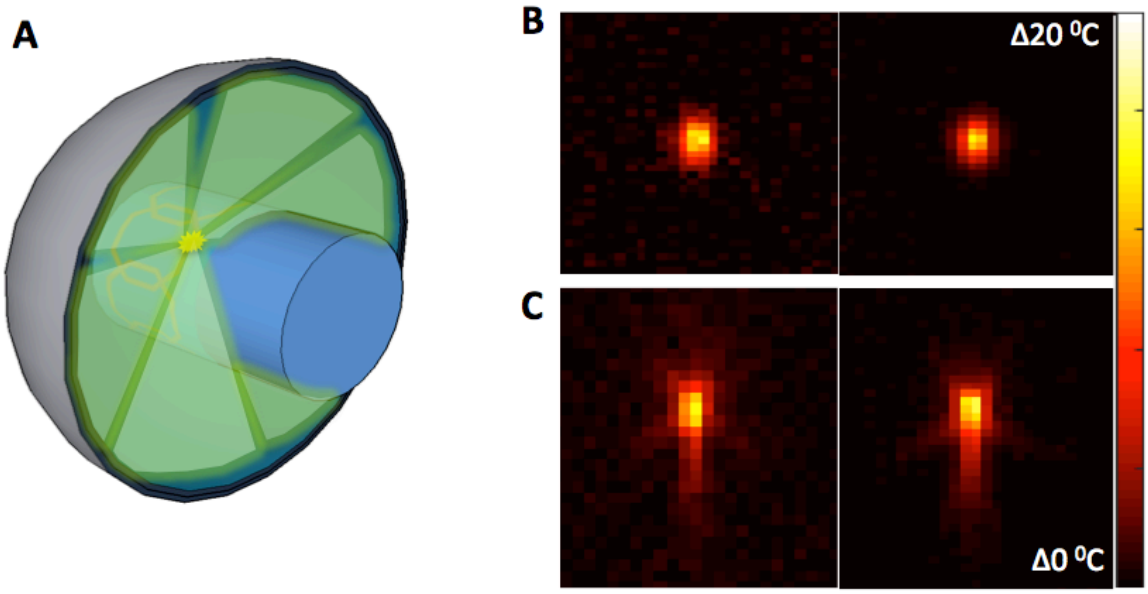

Figure 5.16: **A.** Illustration of phantom in scanner with the array wrapped around a gel phantom. Acoustic energy (green) is passed through the test array submerged in water (blue) inside acoustic transducer (grey) **B.** Heat maps tracking the sonication inside the phantom using axial scans of focal point using (right) body coil and (left) printed array. **C.** Coronal scans of focal point from (right) body coil and (left) printed coil array. Higher SNR from printed array leads to less noise in heat map.

Figure 5.16 B and C show axial and coronal slices of the maximum heating point for each of these experiments. The heating occurred in the center of the phantom where the 4-channel printed array had slightly more than double the SNR of the body coil. As a result, in both the coronal and axial slices of the heating profile, the coil array provides clearer heating profiles. This is more evident in the coronal profile where the printed array easily shows the side lobes of the heating from the focal point, while the body coil only provides a faint outline of the total profile. The increased SNR from this coil array would allow more precise estimation of temperature increase, particularly near the focal point.

5.5 In Scanner Heating Experiments

5.5.1 Phantom heating

To characterize the acoustic attenuation measured by the scanner, an area inside a homogeneous gel phantom is heated with an in-table transducer (Insightec ExAblate 2100) with 54W of acoustic energy at 1 MHz for 10 seconds for an approximate temperature rise of 20 °C. For clarity, Fig. 5.16 A shows how the coil is placed in-between the transducer and the phantom during these experiments. The temperature increase is tracked with the body coil of a 3T MR scanner with and without the array to maintain measurement consistency. An axial slice of the beam is prescribed to map the temperature every 3.4 seconds. To prevent the focal spot of the transducer from only being partially captured by the single slice, the temperature increase is measured 10

times, each point evenly spaced along 10 mm of the focal point of the transducer. After scanning, the complex image data is reconstructed to show the temperature increase by measuring the phase difference as described in section 5.1.2 [2]. The maximum temperature recorded is used as the benchmark for comparison. The acoustic power is applied at the same time to ensure accurate capture of the maximum heating point.

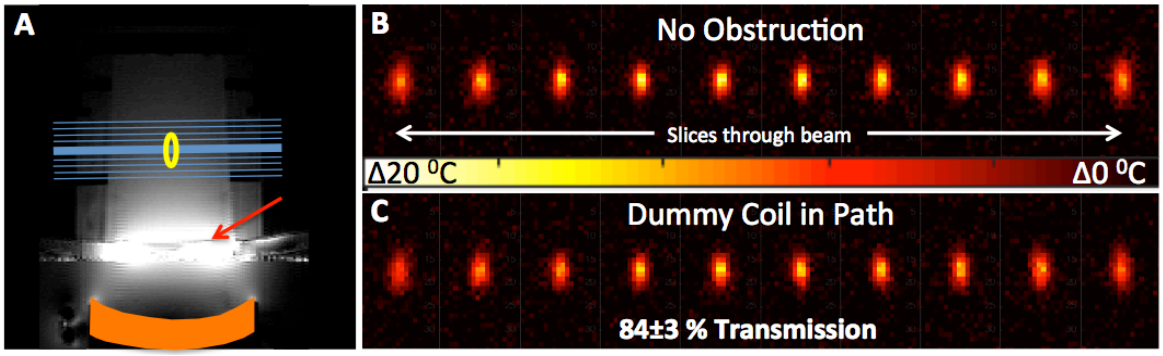

Figure 5.17: **A.** Scan of the phantom on a fibroid transducer using printed array. Red arrow shows location of the array, orange shape highlights location of the transducer, blue lines show the locations of slices used to track heating, and yellow oval shows approximate location of heating. **B.** Heating point inside of phantom without a coil and **C** with the array present. Heating is tracked with body coil in both cases for maintain the same conditions for comparison.

Figure 5.17 B and C show examples of the focal point temperature maps taken with the body coil without and with the 4-channel array present, respectively. When the 4-channel array is placed between the transducer and the phantom, 83±3% of the temperature rise is measured without any significant beam distortion. This value matches those seen in the water bath testing along with the acoustic modeling. This 17% attenuation is considerably smaller than the attenuation due to the skull, which is approximately 70% [35]. This attenuation would be much smaller on the 650 kHz head system as suggested by the water bath testing, however the low image SNR from the body coil did not allow precise temperature measurement for comparison.

5.5.2 Ex-vivo Tissue Heating

To demonstrate the proof-of-concept of all system elements working together, a 4-channel array is used to track the heating of brain tissue inside the head transducer. A 3D printed ABS plastic skull mimics bone containing an ex vivo bovine brain suspended in a gel of 2% agar, 1.2 % silica, and 25 % evaporated milk as described in Menkiou et al. [36]. A thin latex membrane is stretched around the entire phantom to prevent animal tissue from contacting the clinical system. The phantom is mounted to the patient table of the head transducer and scanned with an ultra fast gradient echo that had a flip angle of 30^{o}, TE of 12.8 ms, TR of 25.7 ms, 1 average. An imaging slice 34x34 cm and 3 mm thick with 256 frequency encodes and 128 phase encodes is taken every 3.4 seconds to track heating. The head transducer (InSightec Exablate 4000) applied 200 W of acoustic power to the targeted area for 10 seconds. The heating map is overlaid onto an anatomy

scan obtained using a fast relaxation fast spin echo with TE of 100.7 ms, TR of 4565 ms, FA of 111°, and 2.5 averages. Each slice is 34x34 cm and 2 mm thick.

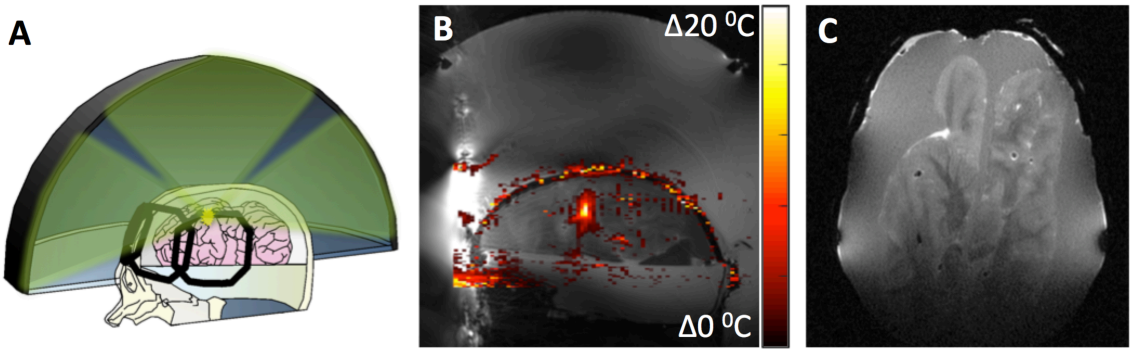

Figure 5.18: **A.** Illustration showing printed array wrapped around skull and brain phantom containing bovine brain submerged in water inside the head transducer. **B.** Sagittal of brain phantom with overlaid heating map tracked with 4-channel array. **C.** Axial scan of skull and brain phantom showing anatomical image quality from the 4-channel array.

The experimental setup, shown in Figure 5.18 A, positions the 4-channel array on a skull phantom while it is heated inside a head transducer. The temperature map obtained is overlaid on the anatomy scan of the bovine brain in Figure 5.18 B. The temperature map in Fig 5.18 B is similar to the heating profile shown in Fig 5.16 B, indicating there is not significant distortion or attenuation due to the array. Similar to the phantom scans, SNR in the heating region is twice as high as that given by the body coil.

In addition to the heating, a high-resolution scan of the phantom is taken inside the transducer, shown in Figure 5.18 C. From the image in Fig 5.18 C, it is shown that there is a reduction in SNR towards the back of the head due to incomplete coverage of the head from the limited width of the array. This can easily be corrected by using additional arrays, but it is beyond the capability of our experimental setup. Overall the array performed well, tracking the heating point inside the skull without significantly attenuating or visibly distorting the acoustic power.

5.6 Conclusions

Our printed coils show high SNR in phantoms, ex-vivo tissue, and volunteers while not significantly interfering with the operation of the MRgHIFU system. With the advances presented in this work, coils designed for MRgHIFU can now take advantage of the current state of the art array designs without the restriction imposed by the position of the ultrasonic transducer. The high SNR offered by these designs provides better resolution, allows for more intricate sequences to be run, and enables faster acquisition of heat maps to monitor treatment. This work can bring MRgHIFU the powerful imaging tools that physicians are accustomed to have in diagnostic imaging, enabling new methods of treatment for this highly versatile technique.

5.7 References

[1] H. E. Cline, J. F. Schenck, K. Hynynen, R. D. Watkins, S. P. Souza, and F. A. Jolesz, "MR-guided focused ultrasound surgery," *J Comput Assist Tomogr,* vol. 16, pp. 956-65, Nov-Dec 1992.

[2] V. Rieke and K. Butts Pauly, "MR thermometry," *J Magn Reson Imaging,* vol. 27, pp. 376-90, Feb 2008.

[3] H. Ruhnke, T. Eckey, M. K. Bohlmann, M. P. Beldoch, A. Neumann, A. Agic*, et al.*, "MR-guided HIFU treatment of symptomatic uterine fibroids using novel feedback-regulated volumetric ablation: effectiveness and clinical practice," *Rofo,* vol. 185, pp. 983-91, Oct 2013.

[4] M. de Smet, E. Heijman, S. Langereis, N. M. Hijnen, and H. Grull, "Magnetic resonance imaging of high intensity focused ultrasound mediated drug delivery from temperature-sensitive liposomes: an in vivo proof-of-concept study," *J Control Release,* vol. 150, pp. 102-10, Feb 28 2011.

[5] E. E. Konofagou, Y. S. Tung, J. Choi, T. Deffieux, B. Baseri, and F. Vlachos, "Ultrasound-Induced Blood-Brain Barrier Opening," *Current Pharmaceutical Biotechnology,* vol. 13, pp. 1332-1345, Jun 2012.

[6] F. A. Jolesz, "MRI-guided focused ultrasound surgery," *Annu Rev Med,* vol. 60, pp. 417-30, 2009.

[7] E. A. Stewart, W. M. Gedroyc, C. M. Tempany, B. J. Quade, Y. Inbar, T. Ehrenstein*, et al.*, "Focused ultrasound treatment of uterine fibroid tumors: safety and feasibility of a noninvasive thermoablative technique," *Am J Obstet Gynecol,* vol. 189, pp. 48-54, Jul 2003.

[8] P. Ghanouni, A. Dobrotwir, A. Bazzocchi, M. Bucknor, R. Bitton, J. Rosenberg*, et al.*, "Magnetic resonance-guided focused ultrasound treatment of extra-abdominal desmoid tumors: a retrospective multicenter study," *Eur Radiol,* May 5 2016.

[9] C. X. Li, W. D. Zhang, W. J. Fan, J. H. Huang, F. J. Zhang, and P. H. Wu, "Noninvasive Treatment of Malignant Bone Tumors Using High-Intensity Focused Ultrasound," *Cancer,* vol. 116, pp. 3934-3942, Aug 15 2010.

[10] W. J. Elias, D. Huss, T. Voss, J. Loomba, M. Khaled, E. Zadicario*, et al.*, "A pilot study of focused ultrasound thalamotomy for essential tremor," *N Engl J Med,* vol. 369, pp. 640-8, Aug 15 2013.

[11] A. L. Elaimy, J. J. Demakas, B. J. Arthurs, B. S. Cooke, R. K. Fairbanks, W. T. Lamoreaux*, et al.*, "Gamma knife radiosurgery for essential tremor: a case report and review of the literature," *World J Surg Oncol,* vol. 8, p. 20, 2010.

[12] J. Hindley, W. M. Gedroyc, L. Regan, E. Stewart, C. Tempany, K. Hynyen*, et al.*, "MRI guidance of focused ultrasound therapy of uterine fibroids: early results," *AJR Am J Roentgenol,* vol. 183, pp. 1713-9, Dec 2004.

[13] P. B. Roemer, W. A. Edelstein, C. E. Hayes, S. P. Souza, and O. M. Mueller, "The NMR phased array," *Magn Reson Med,* vol. 16, pp. 192-225, Nov 1990.

[14] J. T. Vaughan and J. R. Griffiths, *RF coils for MRI*. Chichester, West Sussex: John Wiley and Sons Ltd., 2012.

[15] Y. F. Zhou, "High intensity focused ultrasound in clinical tumor ablation," *World J Clin Oncol,* vol. 2, pp. 8-27, Jan 10 2011.
[16] G. S. Kino, *Acoustic waves : devices, imaging, and analog signal processing*. Englewood Cliffs, N.J.: Prentice-Hall, 1987.
[17] K. P. Pruessmann, M. Weiger, M. B. Scheidegger, and P. Boesiger, "SENSE: sensitivity encoding for fast MRI," *Magn Reson Med,* vol. 42, pp. 952-62, 1999.
[18] M. A. Jacobs, E. H. Herskovits, and H. S. Kim, "Uterine fibroids: diffusion-weighted MR imaging for monitoring therapy with focused ultrasound surgery--preliminary study," *Radiology,* vol. 236, pp. 196-203, Jul 2005.
[19] E. O. Stejskal and J. E. Tanner, "Spin Diffusion Measurements: Spin Echoes in the Presence of a Time-Dependent Field Gradient," *Journal of Chemical Physics,* vol. 42, pp. 288-+, 1965.
[20] R. D. B. Watkins, Rachelle; Pauly, Kim Butts, "Integration of an Inductive Driven Axially Split Quadrature Volume Coil with MRgFUS System for Treatment of Human Brain," in *ISMRM*, Milan, Italy, 2014.
[21] E. M. Minalga, R;Todd, N; Payne, A; Parker,D;Hadley,JR, "A 6-Channel Brain Coil for MR Guided High Intensity Ultrasound," in *ISMRM*, Melbourne Australia, 2012.
[22] A. Payne, R. Merrill, E. Minalga, U. Vyas, J. de Bever, N. Todd*, et al.*, "Design and characterization of a laterally mounted phased-array transducer breast-specific MRgHIFU device with integrated 11-channel receiver array," *Med Phys,* vol. 39, pp. 1552-60, Mar 2012.
[23] M. O. T. Kohler, M.; Syrja, A.; Nakari, R.; Ylihautala, M., "Ultrasound-transparent RF coil design for improved MR thermometry of HIFU therapy.," in *19th Annual Meeting of ISMRM*, Montreal, Canada, 2011, p. 1728.
[24] D. O. Brunner, N. De Zanche, J. Frohlich, J. Paska, and K. P. Pruessmann, "Travelling-wave nuclear magnetic resonance," *Nature,* vol. 457, pp. 994-8, Feb 19 2009.
[25] J. R. Corea, A. M. Flynn, B. Lechene, G. Scott, G. D. Reed, P. J. Shin*, et al.*, "Screen-printed flexible MRI receive coils," *Nat Commun,* vol. 7, p. 10839, 2016.
[26] J. R. Corea, P. B. Lechene, M. Lustig, and A. C. Arias, "Materials and Methods for Higher Performance Screen-Printed Flexible MRI Receive Coils," *Magn Reson Med,* Sep 9 2016.
[27] G. Pron, "Magnetic Resonance-Guided High-Intensity Focused Ultrasound (MRgHIFU) Treatment of Symptomatic Uterine Fibroids: An Evidence-Based Analysis," *Ont Health Technol Assess Ser,* vol. 15, pp. 1-86, 2015.
[28] M. Peller, H. M. Reinl, A. Weigel, M. Meininger, R. D. Issels, and M. Reiser, "T1 relaxation time at 0.2 Tesla for monitoring regional hyperthermia: feasibility study in muscle and adipose tissue," *Magn Reson Med,* vol. 47, pp. 1194-201, Jun 2002.
[29] J. Chen, B. L. Daniel, and K. B. Pauly, "Investigation of proton density for measuring tissue temperature," *J Magn Reson Imaging,* vol. 23, pp. 430-4, Mar 2006.

[30] A. R. Bleier, F. A. Jolesz, M. S. Cohen, R. M. Weisskoff, J. J. Dalcanton, N. Higuchi*, et al.*, "Real-time magnetic resonance imaging of laser heat deposition in tissue," *Magn Reson Med,* vol. 21, pp. 132-7, Sep 1991.

[31] A. R. Selfridge, "Approximate Material Properties in Isotropic Materials," *Ieee Transactions on Sonics and Ultrasonics,* vol. 32, pp. 381-394, 1985.

[32] J. E. Carlson, J. van Deventer, A. Scolan, and C. Carlander, "Frequency and temperature dependence of acoustic properties of polymers used in pulse-echo systems," *2003 Ieee Ultrasonics Symposium Proceedings, Vols 1 and 2,* pp. 885-888, 2003.

[33] Onda Corporation. (2003, Nov. 11, 2016). *Acoustic Properties of Materials*. Available: http://www.ondacorp.com/images/Solids.pdf

[34] Onda Corporation. (2003, Nov. 11, 2016). *Acoustic Properties of Liquids*. Available: http://www.ondacorp.com/images/Liquids.pdf

[35] G. Pinton, J. F. Aubry, E. Bossy, M. Muller, M. Pernot, and M. Tanter, "Attenuation, scattering, and absorption of ultrasound in the skull bone," *Med Phys,* vol. 39, pp. 299-307, Jan 2012.

[36] G. Menikou, T. Dadakova, M. Pavlina, M. Bock, and C. Damianou, "MRI compatible head phantom for ultrasound surgery," *Ultrasonics,* vol. 57, pp. 144-52, Mar 2015.

Chapter 6

6. Conclusions and Future Work

6.1 Conclusions

The work described in this thesis provides a new approach to the well-established field of coil design and represents a significant advance for printed medical devices. Screen printing coils allows them to be thin, lightweight, and flexible. These attributes allow coils to uniquely address challenges in pediatric imaging as well as MRgHIFU procedures. Additionally, the advances described here give the array designer powerful new tools and techniques to design the next generation array, focusing more on patient comfort and reproducibility rather than ultimate SNR.

Several screen printed coils produced images on par with commercially available coils and arrays. While the current SNR of a printed coil is 3-7% lower than the high quality copper coils, the flexibility offered by the printed coils allow them to surpass poorly fitting traditional coils if they are more than 18 mm away from the patient.

The characterization techniques described in detail allow for rapid study of new materials providing tools for future research. Existing and emerging materials can be quickly compared to quantify any SNR gain that a new material may bring.

This thesis evaluates coil materials starting from individual components and methodically built up to full system demonstrations. Characterization of individual component performance properties is supported by quality factor measurements of the coils made with those components. The quality factor measurements are verified with the SNR measured from phantom images from 1.5 and 3 T scanners. Phantom measurements in turn served as an accurate prediction of the SNR seen in our volunteer studies. With this step-by-step approach for characterizing and validating coils, the arrays for both pediatric and interventional MRgHIFU surgery are developed.

The coil array created for pediatric patients provides 6 times the SNR at the surface of the volunteer compared to a commercially available head coil and half of the SNR in the center of the volunteer. The coverage could be further optimized to provide higher SNR throughout the entire sample. Furthermore, the printed array was able to provide high SNR while only weighing 125 g, significantly lighter than the commercial coil array. This greatly reduced weight would be more tolerable for most pediatric patients compared to current coil arrays intended for adults.

The MRgHIFU surgery coils were able to provide an SNR increase of up to 5 times the SNR of the low-resolution body coil used. The coils provided this improvement without significantly impacting the acoustic energy used for heating, passing 83% of the incident energy at 1 MHZ and up to 90% at 650 kHz. In the system level proof-of-concept, the acoustically transparent printed array was able to track the heating in an ex-vivo brain. The coil arrays produced heat maps with high SNR, easily tracking the focal point. The array showed considerably lower attenuation then the skull, having very little impact on the focal spot intensity and shape.

In summary, thin, flexible and conformable receive coils with high SNR have been demonstrated on 1.5 T and 3 T clinical scanners. The characterization techniques

discussed here allow for rapid characterization of printed materials speeding up coil development. Furthermore, the benefits of lightweight and thin printed coils have been shown in pediatric and MRgHIFU applications.

6.2 Suggestions for Future Work

Throughout this thesis, several suggestions have been made to further improve printed MRI coils, however a more in depth discussion is needed. Here several topics are covered which may improve printed MRI coils and represent interesting avenues of future research. Additionally, some topics that were not previously covered are included as well.

While extremely flexible coils create tightly fitting arrays with high SNR they also introduce new challenges. In particular, if the coils move during imaging, the closely fitting coils amplify image artifacts created circulatory and respiratory motion [1, 2]. While there has been a tremendous development in image processing to compensate for motion [3, 4], having received coils move and change their sensitivity pattern during a scan would add a new degree of difficulty to remove these artifacts. An ideal coil is one that is flexible and conformable to the patient during positioning, then locked into place during imaging. One way to create this array would be to adopt some of the techniques used in the ridged formers employed by current coils, like the adjustable wrist array discussed in Nordmeyer-Massner et al. [5]. Unlike the ridged coils, the printed elements could be mounted in the patient padding, giving a custom fit while restricting motion. This type of former could be employed by traditional fabrication techniques or novel ones such as 3D printing [6] to make a new generation of custom fitting hardware.

The work in this thesis has mostly been limited to the coil portion of the receive chain, however other portions could benefit from optimization. All the printed coils proposed in this thesis used traditional connection means, such as coaxial cables with large connectors. As a result, the most unwieldy and bulky part of our array was the cabling and connectors. There have been several techniques introduced in other works to reduce the amount of cabling by relying on time multiplexing of the signal [7], but more can be done to improve the implementation. Printing the transmission lines that connect coil to scanner, along with the cable traps may be one avenue of research that could provide significant packaging gains.

One of the limitations of the screen printed coil design is the conductivity of the silver conductor. While the screen printed films are near the thickness of the skin depth at 1.5 and 3 T there is still some enhancement to be made as previously shown in chapter 4. Other deposition techniques such as 3D printing, blade coating, or spray coating could create even thicker films that are more resilient to bending than the screen printed films examined here. A more conductive film would only provide 3-7 % improvement over the screen printed coils for clinical use, but could produce gains of up to 50% for printed coils used in system that are coil-noise dominated [8].

The linear array topology examined in this thesis was chosen based on ease of processioning and implementation. However, it did not fully take advantage of the limitless design possibilities that solution processing has to offer. Folded or origami style topologies [9] could be implemented to provide better coverage for patients or create

coils internal to the body that could be deployed once inside, similar to current endo-recital coils [10]. Furthermore, if coils are flexible, or even stretchable, certain topographies that maintain a constant area while stretching could be used. One geometric shape called a trellis is able to do this and has already been implemented for other more traditional coil designs [11].

The SNR gain for interventional HIFU arrays is shown in chapter 5, however much needs to be done to make the array ready for the clinic. More system integration on the hardware and software is needed before it is ready to help doctors to treat patients. In particular, the coils need to be able to transmit as well as receive to fully address excitation problems with MRgHIFU of the brain [12]. This raises many new questions about a printed material's ability to handle the higher currents needed during excitation as well as any SAR hotspots created by the semi-flexible coils. The heat dissipation of this device topology has not been well characterized. More research is needed to determine if the surrounding water and ink could remove heat fast enough to prevent significant heating.

Thin printed coils could also be used for lowering the coil attenuation in PET-MRI scanners. Several coils have been designed to reduce the attenuation from X-rays as well as PET emissions [13, 14], but printing may provide additional gains. Currently, the silver used for the printed conductor is not a great candidate for PET transparency due to the high atomic number of silver. However the process could be used to deposit other printed conductors that are better suited to decrease shielding from coils.

Very little is done in this thesis to optimize the final packaging the printed coils were placed into. In traditional arrays, the final enclosure has often been the largest source of inflexibility and weight taking away from any flexibility the coils may have offered. Using the developments and technology from the textile industry, printed coils can easily be integrated with novel fabrics or other materials to create a truly flexible and robust device. Fasteners such as zippers, buttons, and thread could be used to build form fitting coils, much the same way they are used in creating clothing.

The substrates for printed coils do not need to be limited to inert plastic films or fabrics. The versatility of printing allows it to be applied to many different surfaces, including directly to the skin [15]. While there is very limited application for this in clinical imaging, permanent coils on research animals have been used previously [16]. The soft printed design could deliver the usefulness of a permanent implant while being flexible enough not to significantly impact a research animal's quality of life.

While this thesis has focused on some specific applications for printed MRI coils, many opportunities still exist. The biggest strength of these coils is their ability to be easily packaged in new and interesting ways making dramatically different receive coils. With the techniques outlined in this thesis, printed coils can continue to improve MRI in ways not previously possible. Using these methods, along with the countless other advances in MR, MRI is inching forward, hopefully one day becoming as simple and fast as a CT or X-ray while providing an order of magnitude more information.

6.3 References

[1] D. Nishimura, *Principles of Magnetic Resonance Imaging*: Stanford University, 2010.

[2] L. D. Landau and E. M. Lifshitz, *The classical theory of fields*, 3d rev. English ed. Oxford, New York,: Pergamon Press, 1971.
[3] M. Uecker, S. Zhang, D. Voit, A. Karaus, K. D. Merboldt, and J. Frahm, "Real-time MRI at a resolution of 20 ms," *NMR in Biomedicine,* vol. 23, pp. 986-994, Oct 2010.
[4] J. Y. Cheng, T. Zhang, N. Ruangwattanapaisarn, M. T. Alley, M. Uecker, J. M. Pauly*, et al.*, "Free-breathing pediatric MRI with nonrigid motion correction and acceleration," *J Magn Reson Imaging,* vol. 42, pp. 407-20, Aug 2015.
[5] J. A. Nordmeyer-Massner, N. De Zanche, and K. P. Pruessmann, "Mechanically adjustable coil array for wrist MRI," *Magn Reson Med,* vol. 61, pp. 429-38, Feb 2009.
[6] R. A. G. Horch, J.C., "3D-Printed RF Coils for solution-state NMR: Towards low-cost, high-throughput arrays," in *ISMRM 2015*, Toronto Canada, 2015.
[7] D. Lu, "Flexible RF coils for MRI system," US 5548218 A, 1996.
[8] L. Darrasse and J. C. Ginefri, "Perspectives with cryogenic RF probes in biomedical MRI," *Biochimie,* vol. 85, pp. 915-37, 2003.
[9] Z. Yan, F. Zhang, J. Wang, F. Liu, X. Guo, K. Nan*, et al.*, "Controlled mechanical buckling for origami-inspired construction of 3D microstructures in advanced materials," *Adv Funct Mater,* vol. 26, pp. 2629-2639, Apr 25 2016.
[10] S. M. Noworolski, J. C. Crane, D. B. Vigneron, and J. Kurhanewicz, "A clinical comparison of rigid and inflatable endorectal-coil probes for MRI and 3D MR spectroscopic imaging (MRSI) of the prostate," *J Magn Reson Imaging,* vol. 27, pp. 1077-82, May 2008.
[11] G. F. Wiggins, A, "The Trellis Coil: A Morphing, Size Adaptable Array Coil," in *ISMRM*, Signapore, 2016.
[12] R. D. B. Watkins, Rachelle; Pauly, Kim Butts, "Integration of an Inductive Driven Axially Split Quadrature Volume Coil with MRgFUS System for Treatment of Human Brain," in *ISMRM*, Milan, Italy, 2014.
[13] C. Y. Sander, B. Keil, D. B. Chonde, B. R. Rosen, C. Catana, and L. L. Wald, "A 31-channel MR brain array coil compatible with positron emission tomography," *Magn Reson Med,* vol. 73, pp. 2363-75, Jun 2015.
[14] V. Rieke, A. Ganguly, B. L. Daniel, G. Scott, J. M. Pauly, R. Fahrig*, et al.*, "X-ray compatible radiofrequency coil for magnetic resonance imaging," *Magn Reson Med,* vol. 53, pp. 1409-14, Jun 2005.
[15] D.-H. Kim, N. Lu, R. Ma, Y.-S. Kim, R.-H. Kim, S. Wang*, et al.*, "Epidermal Electronics," *Science,* vol. 333, pp. 838-843, 2011.
[16] T. Janssens, B. Keil, R. Farivar, J. A. McNab, J. R. Polimeni, A. Gerits*, et al.*, "An implanted 8-channel array coil for high-resolution macaque MRI at 3T," *Neuroimage,* vol. 62, pp. 1529-36, Sep 2012.